UNIVERSITY OF CALIFORNIA, SAN DIEGO

Observations and Modeling of Crustal Deformation due to Recent Large Earthquakes around the Tibetan Plateau

A dissertation submitted in partial satisfaction of the
requirements for the degree
Doctor of Philosophy

in

Earth Sciences

by

Kang Wang

Committee in charge:

Professor Yuri Fialko, Chair
Professor Kevin Brown
Professor Xanthippi Markenscoff
Professor David Sandwell
Professor Dave Stegman

2017

The dissertation of Kang Wang is approved, and it is acceptable in quality and form for publication on microfilm and electronically:

_____

_____

_____

_____

_____

Chair

University of California, San Diego

2017

DEDICATION

To my lovely wife Mrs Chu Yu.

EPIGRAPH

All models are wrong, but some are useful.

—George E.P. Box

TABLE OF CONTENTS

LIST OF FIGURES

ACKNOWLEDGEMENTS

Time of being a student for more than two decades finally comes to an end. I am fortunate to have the last few years at Scripps. During the years, I received help from many people here at Scripps and other places. First of all, I would like to thank my advisor Prof. Yuri Fialko. Virtually none of the work presented in this thesis would have been possible, without his encouragement, guidance, support, as well as patience over the years. He is always available for discussion and guidance. He is an excellent mentor not only in my research, but also my life. I am deeply impressed by his rigorous attitude on science and good temper in life. I am glad to have the opportunity to work with him. My thank next goes to the other members on my committee: Kevin Brown, Xanthippi Markenscoff, David Sandwell and David Stegman. I thank them for providing suggestions and comments during my study.

My PhD research would not have been possible either, without the fantastic classes taught by many faculty here at IGPP, including Duncan Agnew, David Sandwell, David Stegman, Guy Masters, Peter Shearer, Cathy Constables, etc. I also thank Dr. Peng Fang for his guidance and help on the GPS data processing.

I thank the students and postdocs who have made my study at Scripps so much fun. I am grateful to the diversely talented cohort of which I was part: Nick, Maggie, Shi, Peter, Wenyuan, Qian, Kyle and Lauren. So much memories of working together with you in Keller for the departmental exam. I also thank

my officemates Nick and Erica. It has been a great time being officemates with you. I also thank the Chinese students group here at Scripps: Xiaopeng, Zhitu, Xiaowei, Xiaohua, Zhao, Yuxiang, Qian, Wenyuan, Wei, Yongfei, Shiying and many others. It is your presence at Scripps that makes my life in U.S. more interesting. Particularly, thank you for your help and care when I was sick in hospital. I also benefited from discussions with Zhongwen, Junle and others in the daily lunch group. I would also like to particularly express my gratitude to Xiaopeng and Xiaohua for developing and maintaining the GMTSAR software, to Katia for organizing the great weekly InSAR meeting. I am also grateful to the chatting and discussions with many other current and previous students at IGPP, including Eric Lindsey, Syvain Barbot, Andy Barbour, Daniel Trugman, etc.

Last, and certainly not the least, my sincere thank goes to my wife Chu Yu for her love and support. We often discuss each other's discipline. Thank you for understanding my ignorance on economics and social sciences. And of course, I thank you for correcting my bad pronunciation in English, as well in Chinese, although for now, I still have a hard time to differentiate the pronunciations of 'n' and 'l' in both English and Chinese. Life with you has been quite enjoyable!

Thank you all for your help on my study and living at Scripps !

Chapter 2, in full, is a reprint of the the published paper appearing as: Wang, K., and Y. Fialko (2014), "Space geodetic observations and models of post-seismic deformation due to the 2005 M7.6 Kashmir (Pakistan) earthquake", *Journal of Geophysical Research–Solid Earth* 119, 7306-7318, doi:10.1002/2014JB011122.

The author of this dissertation is the primary investigator of work presented in this chapter.

Chapter 3, in full, is a reprint of the published paper appearing as: Wang, K., and Y. Fialko (2015), "Slip model of the 2015 Mw 7.8 Gorkha (Nepal) earthquake from inver- sions of ALOS-2 and GPS data", *Geophysical Research Letters*, 42, 7452-7458, doi:10.1002/2015GL065201. The author of this dissertation is the primary investigator of work presented in this chapter.

Chapter 4, in full, is a preprint of the material being submitted to *JGR*, which may appear as: Wang, K., and Y. Fialko, "Observations and modeling of co- and post-seismic deformation due to the 2015 Mw 7.8 Gorkha (Nepal) earthquake", *Journal of Geophysical Research: Solid Earth*. The author of this dissertation is the primary investigator of work presented in this chapter.

Chapter 5, in full, is a preprint of the material being prepared for the submission to *JGR*, which may appear as: Wang, K., and Y. Fialko, " Postseismic deformation due to the 2013 Balochistan earthquake observed with Sentinel-1 interferometry",*Journal of Geophysical Research: Solid Earth*. The author of this dissertation is the primary investigator of work presented in this chapter.

Chapter 6, in full, is a preprint of the material submitted to the *IEEE Geoscience and Remote Sensing Letters* as: Wang, K., X. Xu and Y. Fialko, "Improving Burst Alignment in TOPS Interferometry with Bivariate Enhanced Spectral Diversity (BESD)". The author of this dissertation is the primary investigator of work presented in this chapter.

VITA

2004	B. S. in Geophysics, School of Geodesy and Geomatics, Wuhan University, China
2008-2001	M. S. in Geophysics, School of Earth and Space Sciences, Peking University, China
2017	Ph. D. in Earth Sciences, Scripps Institution of Oceanography, University of California, San Diego

PUBLICATIONS

Wang, K. and Y. Fialko (2017). Observations and modeling of co- and post-seismic deformation due to the 2015 Mw 7.8 Gorkha (Nepal) earthquake, *Journal of Geophysical Research: Solid Earth*, in revision.

Wang, K. and Y. Fialko (2015). Slip model of the 2015 Mw 7.8 Gorkha (Nepal) earthquake from inversions of ALOS-2 and GPS data, *Geophysical Research Letters*, 42(18), 7452-7458.

Wang, K. and Y. Fialko (2014). Space geodetic observations and models of postseismic deformation due to the 2015 M7.6 Kashmir (Pakistan) earthquake, *Journal of Geophysical Research:Solid Earth*, 119(9), 7306-7318.

Wang Y., M. Wang, Z. Shen, W, Ge, **K. Wang**, F. Wang and J. Sun (2013). Inter-seismic deformation field of the Ganzi-Yushu fault before the 2010 Mw 6.9 Yushu earthquake, *Tectonophysics*, 584,138-143.

Wang, K. and Z. Shen (2011). Location and focal mechanism of the 1933 Diexi earthquake and its associated regional tectonics, *Acta Seismological Sinnia*, 33(5), 557-567.

ABSTRACT OF THE DISSERTATION

Observations and Modeling of Crustal Deformation due to Recent Large Earthquakes around the Tibetan Plateau

by

Kang Wang

Doctor of Philosophy in Earth Sciences

University of California, San Diego, 2017

Professor Yuri Fialko, Chair

In this dissertation, I use Interferometric Synthetic Aperture Radar (InSAR) and Global Positioning System (GPS) to study the crustal deformation due to several recent large earthquakes around the Tibetan Plateau. The studied events include the 2005 Mw 7.6 Kashmir (Pakistan) earthquake that occurred in the northwest Himalaya, the 2015 Mw 7.8 Gorkha (Nepal) earthquake that occurred along central Himalaya, and the 2013 Mw 7.7 Balochistan earthquake that occurred in the Makran accretionary wedge in southwestern Pakistan. In partic-

ular, I focus on the observations and modeling of postseismic deformation due to these events. Despite of the challenging surface conditions for InSAR and GPS observations in the mountainous regions, I obtain robust measurements of postseismic deformation following the respective earthquake. Among all the three events studied in this dissertation, the observed postseismic displacements several years after the mainshock are all best explained by afterslip that primarily occurs at the downdip extension of the coseismic rupture. Viscoelastic relaxation and poroelastic relaxation seem to have played only a limited role in the postseismic relaxation of the respective earthquake during the corresponding observation period. Postseismic deformation following the 2005 Kashmir earthquake and the 2015 Gorkha earthquake seems to be inconsistent with models of a low viscosity channel beneath the Tibetan Plateau that are often advocated to explain the uplift and topography variations at the plateau margins. Results of this dissertation have implications for the mechanisms of the long-term growth of Tibetan Plateau and accommodation of plate convergence across the Himalayan Arc.

Chapter 1

Introduction

1.1 Earthquake cycle deformation

The sudden release of energy from a major earthquake is one of the most destructive forces in the earth. While by far it is still difficult to forecast earthquake, our knowledge about the earthquake phenomenon has been tremendously enriched since the introduction of the elastic rebound theory by Harry Fielding Reid in 1910, shortly after the devastating 1906 San Francisco. Reid's elastic rebound theory can be summarized as short as that earthquakes are the results of the elastic rebound of the previous elastic strain stored in the rocks on either side of the geological faults. In the time period between major earthquakes (interseismic period), rocks around the fault deform as a result of relative plate motion due to tectonic forces in the far field, while the fault is locked. During the earthquake (coseismic period), the portions of the rock around the fault that were locked move

'spring' back to catch up the motion that the plates moved over the interseismic period. In this model, the material is elastic and the long-term plate motion is accommodated by the summation of interseismic and coseismic displacements across the fault during multiple earthquake cycles.

Recent advances in satellite geodesy, particularly the Interferometric Synthetic Aperture Radar (InSAR) and Global Position System (GPS), have led to a dramatic increase in the quantity and quality of surface deformation measurements. These measurements have significantly improved our understanding about the crustal deformation during earthquake cycles. It is now recognized that, besides the coseismic and interseismic deformation as described above, large earthquakes are often followed by periods of transient surface deformation whose velocities are higher than that of the interseismic deformation. Such transients are often termed as the postseismic deformation. The complete earthquake cycle earthquake thus consists of three phases: interseismic, coseismic and postseismic (Figure 1.1).

Among the three phases of crustal deformation during an earthquake cycle, the origin and mechanisms of the time-dependent postseismic transients are least understood. There are a variety of mechanical processes that could give rise to postseismic deformation, including viscoelastic relaxation of ambient rocks below the seismogenic zone (e.g. *Freed and Bürgmann*, 2004; *Pollitz et al.*, 2001); transient aseismic slip either within the rupture zone or at its downdip extension (e.g. *Savage and Church*, 1974; *Savage and Svarc*, 1997), and flow of pore fluids induced by the earthquake, the so-called poroelastic rebound (e.g. *Fialko*, 2004; *Jonsson*

et al., 2003; *Peltzer et al.*, 1998). If surface deformation from these postseismic relaxation processes can be differentiated, the former may provide valuable constraints on the mechanical properties of the ambient rocks and the fault hosting the earthquake. For instance, the observed postseismic deformation may be used to infer the rheology (i.e. the effective viscosity) of the substrate in case of viscoelastic relaxation, the porosity of the host rocks in case of poroelastic rebound and frictional properties of the fault in case of afterslip.

1.2 Deformation models of the Tibetan Plateau

As a result of the continuous convergence between the Indian and Eurasian plates since $\sim$ 55 Ma ago, the Tibetan Plateau is the largest plateau on the earth (Figure 1.2). It stretches approximately 1,000 kilometres north to south and 2,500 kilometers east to west, with an average elevation exceeding 4,500 meters. Over the past decades, several end-member models have been proposed to describe the long-term evolution and uplift of the Tibetan Plateau. One of the currently vigorous debates is on whether the Tibetan Plateau behaves more as a weak viscous fluid or a series of rigid blocks bounded by major faults. One school of thought suggests that the collision zone is composed of a collage of rigid blocks bounded by several deeply rooted large-scale faults of fast slip rates, and the crustal deformation takes places mainly along those major faults, with little or no deformation inside the blocks (e.g. *Avouac and Tapponnier*, 1993; *Tapponnier et al.*, 1982). By contrast,

another school of thought appeals to the existence of a highly fluid layer in the lower crust, that effectively decouples the deformation of the upper crust from underlying mantle (e.g. *Clark and Royden*, 2000; *England and McKenzie*, 1982; *Royden et al.*, 1997). At the margins of the plateau, particularly at the eastern margin along the Longmenshan range front, the question becomes whether the mountains are formed by crustal faulting and shortening (e.g. *Tapponnier et al.*, 2001), or they are maintained by dynamic pressure from lower-crustal flow (e.g. *Royden et al.*, 1997; *Bird*, 1991) (Figure 1.3). A key difference between these models lies in the rheology (i.e. effective viscosity) of the lower crust and upper mantle in and surrounding the Tibetan Plateau.

The past 15 years have witnessed a number of large earthquakes around the Tibetan Plateau, including the 2005 Mw 7.6 Kashmir (Pakistan) earthquake in northwest Himalaya, the 2008 Mw 7.9 Wenchuan (China) earthquake along the eastern margin of the Tibetan Plateau, the 2013 Mw 7.7 Saravan (Iran) earthquake within the plate boundary between the Arabian and the Eurasian plates, 2013 Mw 7.7 Balochistan (Pakistan) earthquake in the Makran accretionary wedge, and the 2015 Mw 7.8 Gorkha (Nepal) earthquake in central Himalaya (Figure 1.2). Relaxation of the stress change caused the mainshock may induce observable postseismic deformation transients in the respective epicentral area, which can be used to infer the mechanical properties, particularly the rheology, of the Tibetan Plateau's lower crust and upper mantle. This thesis thus focuses on the observations and modeling of postseismic deformation due to three of these events, including the

2005 Kashmir earthquake, the 2013 Balochistan earthquake, and the 2015 Gorkha earthquake. For each earthquake, we compare observed surface deformation to predictions of models assuming different relaxation processes (i.e. afterslip, viscoelastic relaxation, and poroelastic redound) to evaluate what mechanism(s) may have dominated the early-phase (e.g. several years after the mainshock) postseismic relaxation of the respective event. We try to place constraints on the effective viscosity of lithosphere in the collision zone between the Indian and Eurasian plates.

1.3 Thesis overview

This thesis consists of 6 chapters. Chapters 2, 3, 4, 5, 6 were original written to be self-contained articles for individual publications. Although they were initially written to be read in isolation, the main chapters are closely related to one another in theme.

In Chapter 2, we study the postseismic deformation due to the 2005 Mw 7.6 Kashmir (Pakistan) earthquake that occurred in the northwestern Himalaya. In this study, we find that InSAR and GPS observations spanning the time period from 2005 to 2010 are best explained by afterslip on the downdip extension of the coseismic rupture. The effective viscosity of the ductile substrate in the Kashmir region is estimated to be greater than 10^{19} Pas.

In Chapter 3, we model the coseismic surface deformation due to the 2015 Gorkha (Nepal) earthquake in central Himalaya. We find that the rupture of the

2015 Gorkha earthquake is along the fault of a very small dip angle $4-7^{\circ}$. Coseismic slip of the 2015 Mw 7.8 Nepal earthquake is concentrated in a fairly narrow zone (between $\sim$ 50 and $\sim$ 100 km) from the Main Frontal Thrust (MFT) at the deep end of the seismogenic zone. The coseismic slip model derived in this study has been widely adopted by the research community for other relevant studies of this earthquake.

In Chapter 4, we refine the coseismic slip model derived in Chapter 3 with more realistic material structure and study the postseismic deformation due to the 2015 Gorkha (Nepal) earthquake. We find that the coseismic slip model accounting for the lateral variation of surface topography and elastic rigidity across the Himalaya has $\sim$10% slip at the depths of coseismic asperties. We also study the postseismic deformation due to the Gorkha earthquake using InSAR and GPS data. Despite of the challenging surface condition along the Himalayan range, we are able to derive the time series of the InSAR line-of-sight (LOS) displacements due to the postseismic relaxation of the 2015 Gorkha earthquake. Similar to the Kashmir earthquake, postseismic deformation $\sim$2 years after the Gorkha earthquake are best explained the afterslip models with most of the slip occurring at the downdip of the coseismic rupture. Viscoelastic relaxation and poroelastic rebound seem to have contributed little to the postseismic relaxation following the 2015 Gorkha earthquake during the observation period of this study.

In Chapter 5, we study the postseismic deformation due to the 2013 Mw 7.7 Balochistan earthquake that occurred within the Makran accretionary wedge in

southwestern Pakistan. Interferometric Synthetic Aperture Radar (InSAR) data from three tracks of the Sentinel-1 satellite reveal robust post-seismic deformation after the 2013 Balochistan earthquake. Similar to the thrust earthquakes (i.e. the 2005 Kashmir earthquake and the 2015 Gorkha earthquake) that occurred along the Himalaya, postseismic deformation several years after the 2013 Balochistan earthquake is also found to be dominated by afterslip which primarily occurs at the downdip of the coseismic rupture. We also observe a segment of surface creep on the North-East continuation of the 2013 rupture, along the Chaman fault. The creep rate across the InSAR LOS velocities maps has increased by more than an order of magnitude after the 2013 Balochistan earthquake.

In Chapter 6, we propose a method to improve the burst alignment in TOPS (Terrain Observation by Progressive Scans) SAR system. It is a chapter dealing with some technical issues in TOPS SAR system. In this chapter, we show that the Enhanced Spectral Diversity (ESD) method may sometimes be insufficient to compensate the burst misalignment in Sentinel-1 TOPS interferometry. In these cases, the azimuth shift derived from the double differenced interferograms exhibits strong variations along both and azimuth directions. We propose a modification of the ESD method, named Bivariate Enhanced Spectral Diversity (BESD) that relaxes the assumption of a constant azimuth shift and estimates a point-by-point azimuth shift map that varies in both range and azimuth. We demonstrate that the BESD method is able to produce TOPS interferograms without artificial phase discontinuities.

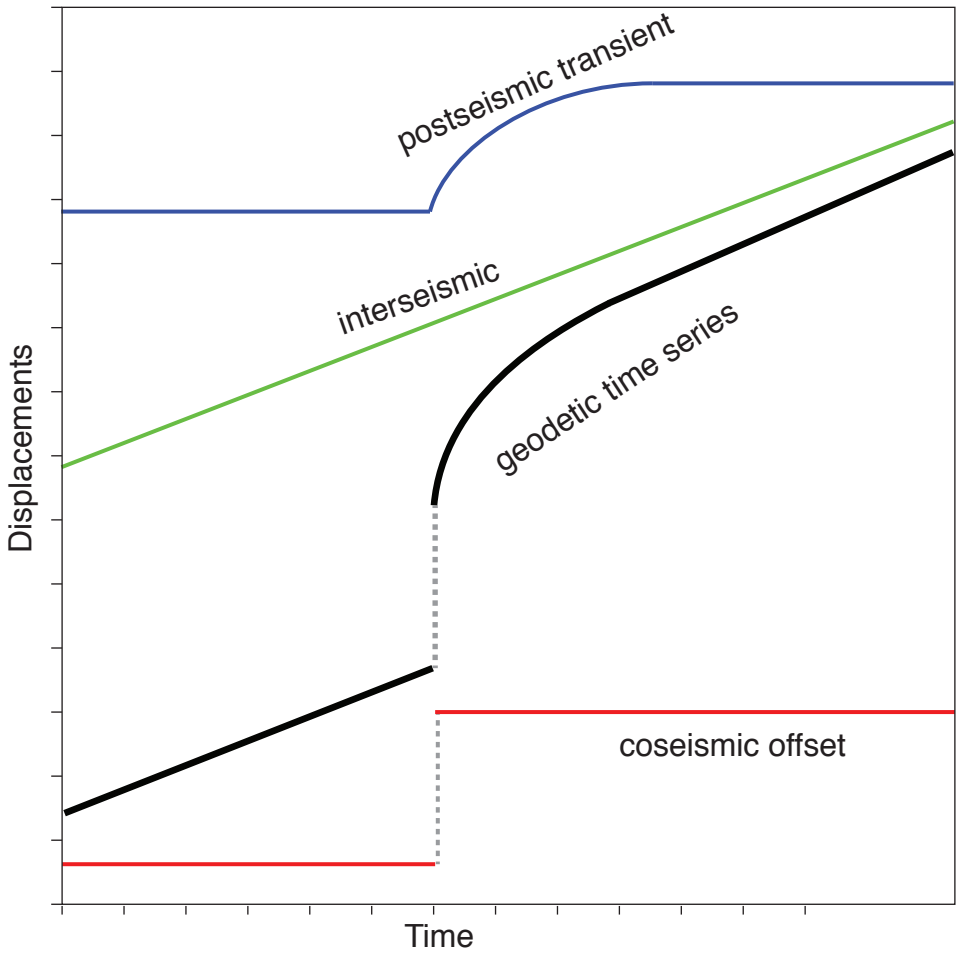

Figure 1.1: Diagram of surface deformation during an earthquake cycle. Black line represents the time series of position for a given point close to the fault during an earthquake cycle. Green line represents position change due to the interseismic loading. Dashed line in between the red lines represents the coseismic offset produced by the earthquake. Blue curve represents the postseismic deformation transients.

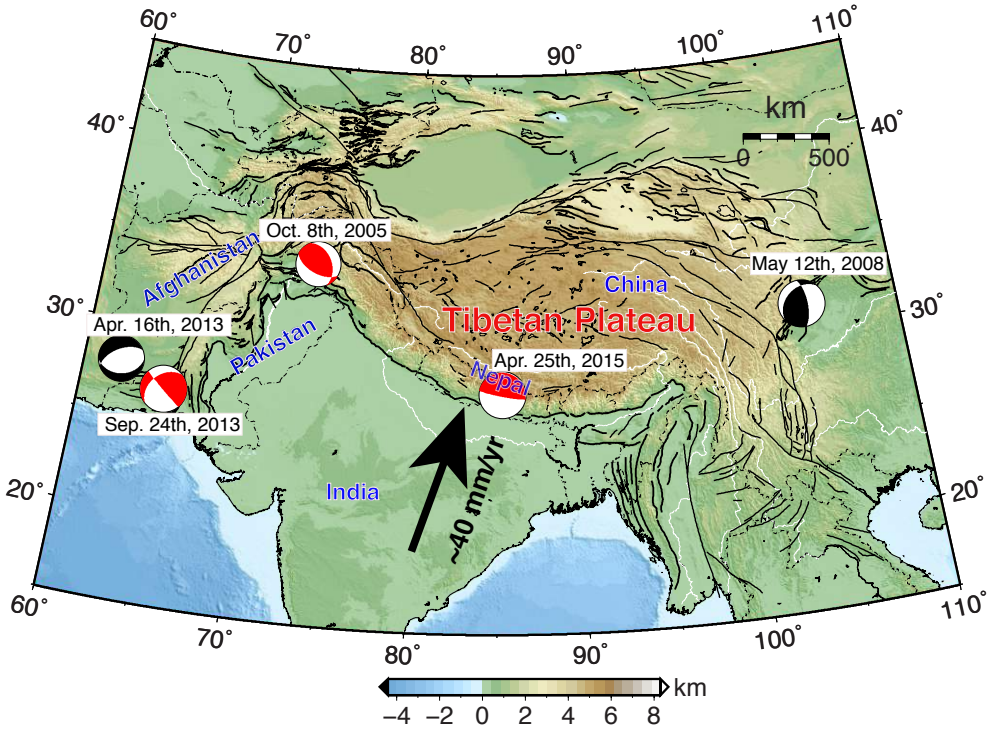

Figure 1.2: Tectonic setting of the Tibetan Plateau and its vicinity regions. The blacks lines represent the active Quaternary faults (*Mohadjer et al.*, 2016). The beach balls denote the location (central moment tensor) and focal mechanisms of the earthquakes of $M > 7.5$ in the past 15 years. Three events studied in this thesis are shown in red.

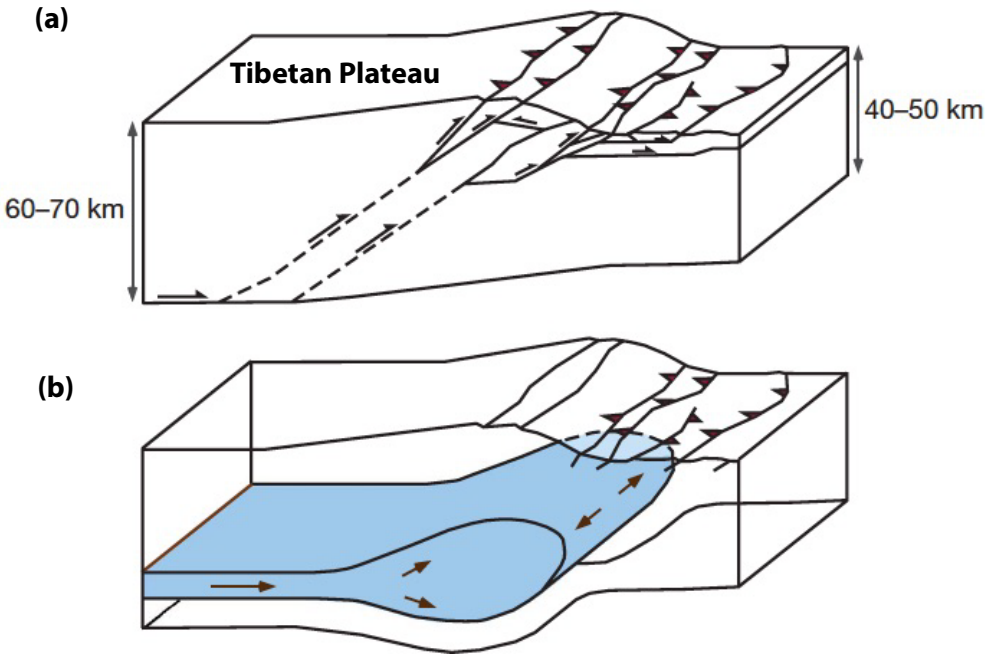

Figure 1.3: Alternative conceptual models for the uplift of the Tibetan Plateau (modified from (*Hubbard and Shaw*, 2009)). (a) uplift is accommodated by thrust faulting and crustal shortening. (b) uplift is accommodated by inflation of the ductile lower crust. The effective viscosity in lower crust of model (b) is suggested to be remarkably low (e.g.$10^{16} - 10^{17}$ Pas)

Bibliography

Avouac, J.-P., and P. Tapponnier (1993), Kinematic model of active deformation in central Asia, *Geophysical Research Letters*, *20*(10), 895–898.

Bird, P. (1991), Lateral extrusion of lower crust from under high topography in the isostatic limit, *Journal of Geophysical Research: Solid Earth*, *96*(B6), 10,275–10,286.

Clark, M. K., and L. H. Royden (2000), Topographic ooze: Building the eastern margin of Tibet by lower crustal flow, *Geology*, *28*(8), 703–706.

England, P., and D. McKenzie (1982), A thin viscous sheet model for continental deformation, *Geophysical Journal International*, *70*(2), 295–321.

Fialko, Y. (2004), Evidence of fluid-filled upper crust from observations of post-seismic deformation due to the 1992 Mw 7.3 Landers earthquake, *Journal of Geophysical Research: Solid Earth (1978–2012)*, *109*(B8), B08,401.

Freed, A. M., and R. Bürgmann (2004), Evidence of power-law flow in the Mojave desert mantle, *Nature*, *430*(6999), 548–551.

Hubbard, J., and J. H. Shaw (2009), Uplift of the Longmen Shan and Tibetan plateau, and the 2008 Wenchuan (M = 7.9) earthquake, *Nature*, *458*(7235), 194–197.

Jonsson, S., P. Segall, R. Pedersen, and G. Bjornsson (2003), Post-earthquake ground movements correlated to pore-pressure transients, *Nature*, *424*(6945), 179.

Mohadjer, Solmaz, Ehlers, Todd Alan, Bendick, Rebecca, Stübner, Konstanze, and Strube, Timo (2016), A Quaternary fault database for central Asia, *Natural Hazards and Earth System Sciences*, *16*(2), 529–542.

Peltzer, G., P. Rosen, F. Rogez, and K. Hudnut (1998), Poroelastic rebound along the Landers 1992 earthquake surface rupture, *Journal of Geophysical Research: Solid Earth*, *103*(B12), 30,131–30,145.

Pollitz, F. F., C. Wicks, and W. Thatcher (2001), Mantle flow beneath a continental strike-slip fault: Postseismic deformation after the 1999 Hector Mine earthquake, *Science*, *293*(5536), 1814–1818.

Royden, L. H., B. C. Burchfiel, R. W. King, E. Wang, Z. Chen, F. Shen, and Y. Liu (1997), Surface deformation and lower crustal flow in eastern Tibet, *Science*, *276*(5313), 788–790.

Savage, J., and J. Church (1974), Evidence for postearthquake slip in the fairview peak, dixie valley, and rainbow mountain fault areas of Nevada, *Bulletin of the Seismological Society of America*, *64*(3-1), 687–698.

Savage, J., and J. Svarc (1997), Postseismic deformation associated with the 1992 Mw=7.3 Landers earthquake, southern california, *Journal of Geophysical Research: Solid Earth*, *102*(B4), 7565–7577.

Tapponnier, P., G. Peltzer, A. Le Dain, R. Armijo, and P. Cobbold (1982), Propagating extrusion tectonics in Asia: New insights from simple experiments with plasticine, *Geology*, *10*(12), 611–616.

Tapponnier, P., X. Zhiqin, F. Roger, B. Meyer, N. Arnaud, G. Wittlinger, and Y. Jingsui (2001), Oblique stepwise rise and growth of the Tibet Plateau, *science*, *294*(5547), 1671–1677.

Chapter 2

Space geodetic observations and models of postseismic deformation due to the 2005 M7.6 Kashmir (Pakistan) earthquake

Abstract

We use the L-band Advanced Land Observing Satellite (ALOS) and C-band Envisat interferometric synthetic aperture data and campaign GPS observations to study the postseismic deformation due to the 2005 magnitude 7.6 Kashmir (Pakistan) earthquake that occurred in the northwestern Himalaya. Envisat data are available from both the descending and ascending orbits and span a time period of

$\sim$4.5 years immediately following the earthquake (2005-2010), with nearly monthly acquisitions. However, the Envisat data are highly decorrelated due to high topography and snow cover. ALOS data are available from the ascending orbit and span a time period of $\sim$ 2.5 years between 2007 and 2009, over which they remain reasonably well correlated. We derive the mean line-of-sight (LOS) postseismic velocity maps in the epicentral area of the Kashmir earthquake using persistent scatterer method for Envisat data and selective stacking for ALOS data. LOS velocities from all data sets indicate an uplift (decrease in radar range), primarily in the hanging wall of the earthquake rupture over the entire period of synthetic aperture radar observations (2005-2010). Models of poroelastic relaxation predict uplift of both the footwall and the hanging wall, while models of viscoelastic relaxation below the brittle-ductile transition predict subsidence (increase in radar range) in both the footwall and the hanging wall. Therefore, the observed pattern of surface velocities indicates that the early several years of postseismic deformation were dominated by afterslip on the fault plane, possibly with a minor contribution from poroelastic rebound. Kinematic inversions of interferometric synthetic aperture radar and GPS data confirm that the observed deformation is consistent with afterslip, primarily downdip of the seismic asperity. To place constraints on the effective viscosity of the ductile substrate in the study area, we subtract the surface deformation predicted by stress-driven afterslip model from the mean LOS velocities and compare the residuals to models of viscoelastic relaxation for a range of assumed viscosities. We show that in order to prevent surface subsidence, the

effective viscosity has to be greater than 10^{19} Pas.

2.1 Introduction

The Mw 7.6 Kashmir earthquake occurred on 8 October 2005 in the northwestern Himalaya (Figure 2.1). This area represents a tectonic boundary resulted from the India-Eurasia collision and is characterized by significant seismicity (e.g. *Bilham et al.*, 2001). The 2005 Kashmir earthquake is the latest and largest seismic event to date that occurred along the Himalaya arc since the advent of modern space geodesy. The coseismic deformation due to this earthquake has been studied extensively using both geodetic (*Avouac et al.*, 2006; *Pathier et al.*, 2006; *Yan et al.*, 2013) and seismic (*Avouac et al.*, 2006; *Parsons et al.*, 2006). Although there are some variations among the proposed rupture models in terms of rupture geometry and slip distribution, all models suggest that the 2005 Kashmir earthquake ruptured a ∼70 km long NE dipping fault with primarily thrust mechanism, with minor component of right-lateral slip, consistent with seismic moment tensor solution determined from modeling of long-period surface waves.

In this study, we investigate surface deformation over several years following the earthquake. Spatiotemporal patterns of postseismic deformation may provide valuable information about mechanical properties of the lithosphere (e.g. *Pollitz et al.*, 2000; *Fialko*, 2004a; *Bürgmann and Dresen*, 2008). Several mechanisms are often invoked to explain the observed transients following large earthquakes,

including afterslip, viscoelastic relaxation, and poroelastic rebound (e.g. *Bürgmann et al.*, 2002; *Fialko*, 2004a; *Barbot et al.*, 2008, 2009). It is often difficult to separate contributions from different mechanisms due to similar patterns of surface motion, especially in case of strike-slip earthquake (e.g. *Savage*, 1990; *Barbot et al.*, 2009). Dip-slip earthquakes, on the other hand, may give rise to distinct pattern of surface displacements that can be readily identified in the geodetic data (e.g. *Nishimura and Thatcher*, 2003; *Yu et al.*, 2003).

Unfortunately, only limited ground-based observations of postseismic deformation due to the 2005 Kashmir earthquake are available because of the difficult access and mountainous terrain in the epicentral area. Based on data from a campaign-mode GPS survey of 18 sites, *Jouanne et al.* (2011) estimated the temporal-spatial evolution of postseismic deformation. They argued that the GPS data are consistent with afterslip along a flat decollement beneath the main rupture. Most of the GPS measurements with high signal-to-noise ratio were made within ∼50 km from the rupture during the first 2 years (2005–2007) after the earthquake. In this study, we complement the available GPS data with C-band Envisat and L-band Advanced Land Observing Satellite (ALOS) synthetic aperture radar (SAR) observations spanning 2005–2010 and 2007–2009, respectively, to characterize the surface deformation over a longer time period and at higher spatial resolution. We compare the observed surface deformation to predictions of models assuming afterslip, viscoelastic relaxation, and poroelastic redound to place constraints on the effective mechanical properties of lithosphere in the collision zone

between the Indian and Eurasian plates.

2.2 Data

2.2.1 Envisat

The C-band Envisat data used in this study are from the ascending track T499 (average incidence angle of 4°) and descending track T463 (average incident angle of 23°). Because of the rugged topography and precipitation in the epicentral area, interferograms suffer from severe decorrelation. To mitigate the problem of geometric and temporal decorrelation, we analyzed the Envisat data using persistent scatter (PS) interferometric synthetic aperture radar (InSAR) technique (e.g. *Ferretti et al.*, 2000; *Hooper et al.*, 2004, 2007). There are 30 scenes available for the ascending track T499, with the first acquisition on 24 October 2005 (about 2 weeks after the earthquake) and last acquisition on 31 May 2010. The descending track T463 has 17 scenes, with first acquisition on 22 October 2005 and last acquisition on 13 June 2009. Figure 2.2 shows the baseline plots for the respective tracks. We processed the data using StaMPS v3.2 (*Hooper et al.*, 2010). Default parameters (e.g., 800 m cutoff wavelength for low-pass filtering in the space domain and 2 years time window for phase smoothing in the time domain) were used unless noted otherwise. The resulting average line-of-sight (LOS) velocities for the respective tracks T499 and T463 are shown in Figures 2.3a and 2.3b, with positive LOS displacements corresponding to surface movement toward the satellite. Data from

both tracks yield comparable rate (∼cm/yr) of LOS surface movement toward the satellite, primarily on the hanging wall side of the fault. We note that depending on the choice of processing parameters, for example, selection of the master scene, noise threshold, averaging window in the spatial domain, etc., the magnitude of the average LOS velocity can vary by a factor of 2 to 3. For instance, changing the value of a parameter for smoothing the spatially correlated noise in temporal domain, from a default value of 2 years to 0.5 year, increases the LOS velocity in the hanging wall to ∼25 mm/yr (cf. Figure 2.3b). Using a shorter time window for smoothing might be desirable to better characterize the time dependence of postseismic relaxation; however, the resulting LOS velocity is much noisier in the space domain. Also, we found that the deformation accumulated during the first 2 years after the earthquake (2005–2007) is smaller than that accumulated during a later period (2007–2010). This may be due to the residual atmospheric artifacts or some other noise. We thus chose to use a default time window (2 years) for the temporal noise filtering to better characterize the average LOS velocity and the spatial pattern of surface deformation. Figure 2.4 shows resulting time series of the LOS displacements for the track T499. LOS displacements of this track are characterized by a monotonic decrease in radar range throughout of the observation period primarily on the hanging wall side of the fault. The radar phase from all unwrapped interferograms was then added and divided by the cumulative time span of the respective interferograms to yield the average LOS velocity during the period of Envisat observations (2005-2010 for ascending track T499 and 2005–2009

for descending track T463).

2.2.2 ALOS

The L-band ALOS data used in this study are from three frames (F660, F670, and F680) of the ascending track T530 (average incidence angle of $\sim 39^{\circ}$), covering the entire rupture (Figure 2.1). There are 18 acquisitions over a time period from 2007 to 2011 (see Figure 2.2 for the baseline plot). We processed the raw SAR data using GMTSAR software (*Sandwell et al.*, 2011). All interferometric pairs satisfy the following criteria: (1) perpendicular baselines less than 700 m, (2) time intervals greater than 1 year, and (3) low root-mean-square (RMS) of interferograms after subtracting the mean radar phase. These criteria are met for a subset of five interferograms with the earliest scene acquired on 17 February 2007 and last scene acquired on 25 August 2009. Because the ALOS data used in our study were in both ALOS User Interface Gateway (AUIG) and Earth Remote Sensing Data Analysis Center (ERSDAC) formats, we processed the interferograms frame by frame and concatenated the unwrapped radar phase ensuring that there are no discontinuities in the overlapping areas. A linear trend was then removed from each interferogram to reduce possible orbital or ionospheric errors. Similar to processing of Envisat data, the radar phase from all five interferograms was added and divided by the cumulative time span of the respective interferograms to produce the average LOS velocity during the period of ALOS observations (2007–2009).

Figure 2.3c shows the resulting average LOS velocity derived from ALOS data. The pattern of the LOS velocity is similar to that derived from Envisat data, with mainly decreases in radar range on the hanging wall side of the fault. The maximum LOS velocity is up to ∼2 cm/yr. Compared to the results of Envisat data from persistent scatter (PS) analysis of Envisat data, the LOS velocities of ALOS are noisier, as expected given a smaller set of independent interferograms, but provide a continuous LOS velocity field. We have verified that the inferred uplift pattern is not due to a residual atmospheric noise by inspecting correlation between topography and LOS velocity over the rest of the image. Away from the rupture area, the dependence of the LOS velocity on elevation, if anything, is an increase in the radar range with elevation; thus, positive LOS velocities in the hanging wall would be enhanced if one removes a linear trend inferred from the regression analysis of the LOS velocity and topography in the far field. A linear north-south trending feature that extends ∼50 km to the south from the middle of the 2005 Kashmir rupture is correlated with the Jhelum fault described by (*Tapponnier et al.*, 2006), although it is not clear whether this might represent triggered fault slip or elevation-dependent atmospheric artifacts.

Figure 2.5 shows the LOS velocities from different satellite tracks along a profile perpendicular to the earthquake rupture. Data from both ALOS track T530 and Envisat ascending track T499 suggest a relatively sharp discontinuity in surface displacements across the fault. The across-fault variations in the LOS velocity are less apparent in the profile from the Envisat descending track T463, possibly due

to a destructive interference of the vertical and horizontal displacements along the radar line of sight (Figure 2.3a). Also, we note that the LOS velocities from the descending Envisat track 463 may be subject to greater uncertainties due to a fewer acquisitions compared to the ascending track 499 (Figure 2.3b). The standard deviation of the mean LOS velocity is ∼3 mm/yr for the Envisat data. For the ALOS data, the uncertainty is more difficult to quantify due to a relatively small number of interferograms used for stacking, but it should be comparable to that of the Envisat data based on the scatter of individual data points from the mean (Figure 2.5).

As the same general pattern of LOS velocity is seen in all satellite tracks with different look geometries and time periods, the signals shown in Figure 2.3 are indicative of surface displacements. Interseismic crustal shortening across the Balakot-Bagh thrust (the main rupture of the 2005 Mw 7.6 Kashmir earthquake) is estimated to be slow, at a rate of 1.1-4.1 mm/yr (*Kaneda et al.*, 2008), and has a negligible contribution to the LOS velocities shown in Figure 2.3. The latter therefore most likely represents postseismic deformation due to the 2005 Kashmir earthquake. In the next section, we will quantitatively analyze the surface displacement fields due to various mechanisms (viscoelastic relaxation, poroelastic rebound, and afterslip) and compare them to the observations to explore what mechanism (or a combination of mechanisms) may have contributed to postseismic deformation following the 2005 Kashmir earthquake.

2.3 Modeling of Postseismic Deformation

2.3.1 Viscoelastic Relaxation

We estimate viscoelastic response due to the Kashmir earthquake using a finite element model. As little is known about the lithospheric structure in the Kashmir region, we assume a simple structure consisting of a 20 km thick elastic layer and viscoelastic substrate with linear Maxwell rheology. More complicated models accounting for nonlinear depth-dependent (e.g. *Freed et al.*, 2010; *Takeuchi and Fialko*, 2013) and spatially heterogeneous (e.g. *Rousset et al.*, 2012) rheologies are not warranted given the limited data resolution. The simulations were performed using the finite element code ABAQUS (`www.simulia.com/products/abaqus_fea.html`). The dimension of the model is 800 km $\times$ 600 km $\times$ 150 km in strike-parallel, strike-perpendicular, and vertical directions, respectively. Zero-displacement boundary conditions are applied at all sides of the model except the top side which is assumed to be stress free. To better resolve the displacement and stress fields close to the fault, the size of the elements gradually increases away from the earthquake rupture. The model contains 1,226,468 tetrahedron elements with near-fault elements as small as $\sim$0.5 km.

Several coseismic slip models are available for the 2005 Kashmir earthquake from inversions of geodetic and seismic data. We use two published finite fault models: *Avouac et al.* (2006) hereafter referred to as 'model' A and *Yan et al.* (2013), hereafter referred to as 'model' Y. Slip distribution is imposed using a split

node technique similar to that used by (*Masterlark*, 2003). To directly compare the model predictions to the InSAR-observed surface velocities (Figure 2.3), we compute the predicted average surface velocity by summing up the differences in surface displacements between the time intervals corresponding to the SAR acquisition dates and divide by the sum of the respective time intervals. The resulting surface velocity is then projected onto the line of sight (LOS) of the satellite to yield the predicted average LOS velocity. Figure 2.6 (Figures 2.6a–2.6c are based on model A, and Figures 2.6d–2.6f are based on model Y) shows the predicted average LOS velocities due to viscoelastic relaxation assuming the effective viscosity of the substrate of 10^{19} Pa s. For both Envisat and ALOS tracks, the viscoelastic relaxation models predict increases in radar range that vary continuously across the fault, in contrast to the observed range changes (Figure 2.3). For the effective viscosity of 10^{19} Pa s, the model predicts increase in radar range at a rate of $\sim$4 cm/yr during the Envisat observation period (2005–2010); the rate decreases to 3 cm/yr during the ALOS observation period (2007–2009). The surface velocity fields predicted for the coseismic model Y appear to be more symmetric with respect to the fault and more uniformly distributed along the fault strike from north to the south, compared to the velocities corresponding to model A. These differences are primarily due to the steeper dip angle and more broadly distributed slip in model Y. Changing the viscosity of the substrate affects the average velocity but does not change the overall pattern of surface motion. To examine the sensitivity of LOS velocity to the thickness of viscoelastic layer, we performed a simulation

assuming a 20 km thick elastic crust, a 40 km thick lower crust with viscosity of 10^{19} Pas, and elastic mantle. The LOS velocity in this case is slightly lower and of shorter wavelength, compared to the model shown in Figure 2.6. We note that the surface subsidence predicted by both models monotonically increases (and decelerates) with time, indicating that the surface deformation field due to viscoelastic relaxation should exhibit a similar pattern during the whole postseismic phase. The significant differences in surface deformation patterns between observations (Figure 2.3) and models (Figure 2.6) thus suggest that viscoelastic relaxation was not the dominant mechanism responsible for transient deformation following the 2005 Kashmir earthquake.

2.3.2 Poroelastic Rebound

We evaluate surface displacements due to poroelastic rebound by differencing the coseismic displacements under undrained and drained conditions. The predicted surface displacements due to poroelastic rebound in the 20 km thick upper crust projected on the line of sight of Envisat and ALOS are shown in Figure 2.7 (Figures 2.7a–2.7c correspond to model A, while 2.7d–2.7f ccorrespond to model Y). We use a Poisson's ratio reduction of 0.03 (from undrained value of 0.28 to drained value of 0.25). The poroelastic rebound model based on both coseismic models (models A and Y) shows decreases in the radar range up to $\sim$5 cm for both Envisat and ALOS tracks, in a qualitative agreement with the data (Figure 2.3). However, the poroelastic model predicts a relatively symmetric uplift (decrease in

radar range) on both sides of the fault, while the InSAR data suggest that the uplift is primarily concentrated in the hanging wall, although a small amount of uplift may also occur in the footwall (Figures 2.3 and 2.5). We note that variations in the reduction of Poisson's ratio and depth extent of fluid-saturated layer do not alter the surface deformation pattern significantly and only affect the magnitude of surface deformation.

By comparing the InSAR observations (Figure 2.3) and modeling results (Figures 2.6 and 2.7), one can conclude that the viscoelastic and poroelastic responses are not able to explain the InSAR data and alternative mechanisms must be involved.

2.3.3 Afterslip

The general pattern of postseismic deformation imaged by InSAR data (uplift in the hanging wall and a relatively sharp discontinuity in LOS velocities across the fault; see Figures 2.3 and 2.5) is suggestive of a continued slip on the earthquake rupture. To get an insight into the spatial distribution of afterslip on the rupture plane, we performed an inversion using the LOS velocities derived from ALOS and GPS measurements from (*Jouanne et al.*, 2011). The fault geometry is based on the coseismic slip model of *Avouac et al.* (2006). We extended the fault segments both in strike and dip directions. We assumed that the fault has a dip angle of 29° down to depth of 15 km and transitions to a décollement with a dip angle of 10° below 15 km (*Jouanne et al.*, 2011). The total downdip width

of the fault is 60 km. The kinked fault planes were then divided into patches whose sizes gradually increase with depth to ensure a uniform model resolution (*Fialko*, 2004b). Each individual patch is allowed to have thrust and right-lateral slip components. Laplacian smoothing is applied between adjacent fault patches to avoid abrupt variations in slip. The inversion problem is further regularized by requiring no slip at the fault edges, except the top edge, which is allowed to slip. This leads to a classical minimization problem for the misfit function:

$$F(m, \lambda) = \| Gm - d \| + \lambda \| \Delta^2 m \| \tag{2.1}$$

where m is the vector of unknown (slip) components, d is the data vector, G is the matrix of Green's functions, Δ^2 is the finite difference approximation of the Laplacian operator used to smooth the model, and λ is a smoothing factor. We use the Green's function for a dislocation in a homogeneous elastic half-space. To reduce the computational burden, the average LOS velocity map is subsampled using a gradient-based resampling scheme. Each resulting data point is then assigned with a weigh based on the number of points in the subsampled area. To minimize possible contributions from the postevent seismic activity in the Indus Kohistan Seismic Zone to the northwest of the Kashmir rupture, data west of 73.3°E longitude were excluded from the inversion.

The optimal value of λ controlling the smoothness of the model was determined using the trade-off relation between the model misfit (residual of model prediction and observation) and the roughness ($1/\lambda$) of the corresponding model

(Figure 2.8). We found that the value of $\lambda = 1.0 \times 10^{-4}$ yields a reasonably smooth slip model with relatively low misfit. The corresponding afterslip model is shown in Figure 2.10a, along with the contours of the coseismic slip models of *Avouac et al.* (2006) and *Yan et al.* (2013). The inferred afterslip mainly occurs downdip fo maximum coseismic slip. The average slip rate during the ALOS observation period (2007–2009) is up to ∼80 mm/yr, a factor of ∼ 4 lower than the rate estimated from the early (2005–2006) GPS measurements by *Jouanne et al.* (2011).

We next examine whether the GPS measurements of *Jouanne et al.* (2011) are consistent with a model derived from InSAR data. Because most of their campaign-mode GPS measurements were conducted during 2005–2007, it is not straightforward to include them in a joint inversion with the LOS velocity derived from ALOS data in this study that correspond to a later time period (2007–2009). By comparing the time evolution of the postseismic displacements and aftershocks, *Jouanne et al.* (2011) suggested that the postseismic displacements of the 2005 Kashmir earthquake can be approximated by the function with log-exponential time dependence (*Fialko*, 2004a; *Perfettini and Avouac*, 2004).

$$U(t) = A \log(1 + d(\exp(t/t_r) - 1)) \tag{2.2}$$

where constants $d = 3200$ and $t_r = 8.8$ yr were determined from the analysis of temporal evolution of aftershocks. We performed a grid search to find the best fitting value of A in equation (2.2) for each GPS sites based upon the relative displacements between different occupations available for that site. The displacements

for each site were then extrapolated over the time period of ALOS observations and stacked in the same fashion as ALOS interferograms to yield the average velocity of each GPS site during the ALOS observation period (∼2007–2009). The resulding GPS velocities have azimuths that are similar to the observed ones at the early postseismic epoch but much reduced amplitudes.

We then combined the average LOS velocities from ALOS data with the extrapolated average GPS velocities for the time period of 2007–2009 in a joint inversion for the afterslip distribution. The use of different data sets in the joint inversion requires some choices for relative weighting of the data (*Simons et al.*, 2002; *Fialko*, 2004b). The optimal values of the relative weights of these two data sets are determined by examining the trade-off relation between misfit of each data set (ALOS and GPS) and their relative contribution to the inversion. We set the relative weight of ALOS data to be 1 and vary the relative weight of GPS data, α, over a certain range. Figure 2.9 shows the trade-off between model misfits for each data set (ALOS and GPS) as a function of α. We look for the optimal value of α such that misfits for each data set are within 30% of the respective minimum values. The value of $\alpha = 0.3$ (see the shaded area in Figure 2.9) was thus chosen as the optimal value for GPS weighting in the joint inversion.

Using the respective optimal values of model smoothness λ and relative weighting α, we infer the afterslip distribution from the joint inversion of ALOS and GPS data (Figure 2.10b). Similar to the inversion using ALOS data only, the afterslip is mainly concentrated on the periphery of high coseismic slip areas. The

maximum slip rate from the joint inversion of ALOS and GPS data is slightly lower than that from inversion of ALOS data only, possibly because the GPS data better constrains the slip rake (the InSAR data from the ascending orbit are only weakly sensitive to strike-slip displacements as the latter are almost orthogonal to the LOS vector). Compared to the afterslip model derived from ALOS data only, the joint inversion has a smaller component of strike slip and a deeper moment centroid of afterslip. Another noticeable difference is the greater amount of afterslip in the northern half of the fault in the joint inversion of ALOS and GPS data. This is consistent with the results of *Jouanne et al.* (2011), who found that afterslip on the Balakot flat (the northern segment) is more pronounced than that on the Bagh flat (the southern segment).

The preferred afterslip model fits both ALOS and GPS data reasonably well. Figure 2.11 shows the comparison of observed surface deformation and predictions of the afterslip model derived from the ALOS and GPS data(Figure 2.10b). Overall, the observed uplift on the hanging wall side of the fault has been recovered by the model. Figure 2.13 shows the comparison of horizontal displacements at the GPS sites of *Jouanne et al.* (2011) (extrapolated and averaged velocities corresponding to the ALOS observation period) and predictions of afterslip, viscoelastic relaxation, and poroelastic rebound models. The overall good agreement between the data and predictions of the afterslip model suggests that deformation during the first several years following the 2005 Kashmir earthquake was dominated by afterslip on the earthquake rupture. The spatial pattern of afterslip appears to

have persisted over the period of observations (2005–2010).

We also compared predictions of afterslip model derived from joint inversion of ALOS and GPS data to Envisat observations spanning ∼4.5 years immediately after the earthquake. The surface deformation patterns revealed by the Envisat observation are used as an independent check on model predictions. Because of different time periods covered by the data, and substantial (up to a factor of 2 to 3) dependence of the mean LOS velocities on parameters used in the persistent scatter InSAR analysis, we adjust the amplitude of the mean LOS velocity derived from Envisat data to render the best agreement with the afterslip model corresponding to the time period of 2007–2009. Figure 2.12 shows the comparisons between the adjusted Envisat LOS velocities from the ascending track T499 (Figures 2.12a–2.12c) and the descending track T463 (Figures 2.12d–2.12f) to the afterslip model predictions. There is a general agreement in the pattern of surface velocities between the Envisat data and the model, suggesting that the early deformation following the 2005 Kashmir earthquake was also dominated by fault afterslip. At some locations close to the rupture trace, the afterslip model seems to underestimate the surface deformation rate (Figures 2.12c and 2.13). While this might be in part due to residual errors in the interferograms (e.g., from atmospheric phase delays), another possibility is that these residuals may signify rapidly decaying shallow creep on the earthquake rupture in the first months and years following the earthquake. Similar behavior was documented by continuous GPS measurements elsewhere (e.g. *Bürgmann et al.*, 2002; *Barbot et al.*, 2009).

2.4 Discussion

Rheological properties of the lower crust and upper mantle are of considerable interest, in particular in actively deforming continental settings such as Tibet. Over the past several decades, several end-member models have been proposed to describe the long-term evolution and uplift of the Tibetan Plateau. Some of the proposed models appeal to a highly fluid layer in the lower crust, with viscosity as low as 10^{16} Pas, that effectively decouples the upper crust from the underlying mantle (e.g. *Royden et al.*, 1997; *Clark and Royden*, 2000). Such low viscosities are ruled out by studies of postseismic deformation due to large earthquakes in Tibet and adjacent areas, which suggest much higher viscosities of $10^{18} - 10^{19}$ Pas (e.g. *Ryder et al.*, 2007, 2011). In most cases, the published estimates of the effective viscosities are, in fact, lower bounds because of a limited observation period and potential trade-offs between different relaxation mechanisms (i.e., epistemic uncertainties).

Our study reveals no obvious contribution of viscoelastic relaxation in the deformation transient following the 2005 Kashmir earthquake. Nevertheless, as the LOS velocities due to viscoelastic relaxation and afterslip have opposite signs on the hanging wall side of the fault, it is possible that the rapid afterslip could overshadow the effects of viscoelastic relaxation (if any). To evaluate how efficiently the signature of viscoelastic relaxation could be canceled by afterslip, we performed an additional set of simulations of stress-driven afterslip assuming that afterslip is

governed by the rate-and-state friction (e.g. *Dieterich*, 1979; *Ruina*, 1983; *Barbot et al.*, 2009). Simulations were performed using numerical code RELAX (*Barbot and Fialko*, 2010). We used the coseismic slip model A (*Avouac et al.*, 2006) to drive afterslip. Afterslip was only allowed in areas that experienced an increase in Coulomb stress (see *Barbot et al.* (2009) for details). Since little information is available about in situ frictional properties of faults in Kashmir region, we used a velocity-strengthening constitutive law with the effective relaxation time of 10 years. Note that the total amount of afterslip and the respective surface deformation in the limit of full relaxation depend only on the coseismic stress change and the assumed fault geometry and not on the details of the constitutive friction law. The resulting total surface displacement is divided by 10 years and then subtracted from the surface velocity field derived from ALOS data to yield the residual LOS velocities 2.14. We compare the residual LOS surface velocities to predictions of viscoelastic relaxation model to test the sensitivity of data to viscosity of the substrate. Figure 2.15 shows the RMS of difference between the viscoelastic model prediction and the residual LOS velocity as a function of effective viscosity. The misfit is largest for viscosities smaller than 10^{19} Pas, indicting that it is unlikely that afterslip could be masking a significant contribution from viscoelastic relaxation. For viscosities above $10^{19}Pas$, because the characteristic relaxation time is greater than the period of observations, the predicted surface deformation is negligible. For the viscosity of 10^{19} Pas, the predicted rate of surface subsidence (increase in radar range) is $\sim$ 3 cm/yr during the period of ALOS observations.

Therefore, 10^{19} Pas is a conservative lower bound on the effective viscosity of the lower crust of the Western Himalaya region. Future observations may further refine this bound. In particular, a transition from uplift to subsidence may signal an onset of viscoelastic relaxation in the ductile substrate.

Previous studies have suggested that fault slip may induce poroelastic deformation in the host rocks (e.g. *Peltzer et al.*, 1998; *Jonsson et al.*, 2003; *Fialko*, 2004a; *LaBonte et al.*, 2009). The inferred timescales of poroelastic rebound are on the order of months to years, depending on the hydraulic diffusivity of the host rocks, as well as on the earthquake rupture size (e.g. *Fialko*, 2004a; *Barbot et al.*, 2008; *Barbot and Fialko*, 2010). For the 2005 Kashmir earthquake, the poroelastic rebound model predicts a uniform uplift (decrease in radar range) on both sides of the fault (Figure 2.7). The LOS velocities from all three InSAR tracks indicated a significant uplift in the hanging wall and only minor (if any) uplift in the footwall (Figures 2.3 and 2.5). The latter could be partly due to the low-pass filtering applied in the data processing. Alternatively, it may be indicative of poroelastic rebound following the Kashmir earthquake. A strong asymmetry in the LOS velocities across the fault (Figures 2.3 and 2.5), as well as a poor fit between the poroelastic model and GPS observations (Figure 2.13), suggests that the contribution of poroelastic rebound to the observed surface deformation following the 2005 Kashmir earthquake is minor, compared to that of afterslip. It remains to be seen whether poroelastic rebound is a common process in the Earth's crust hosting seismogenic faults (e.g. *Jonsson et al.*, 2003; *Fialko*, 2004a; *Barbot et al.*,

2008; *Gonzalez-Ortega et al.*, 2014).

The pattern of surface deformation following the 2005 Kashmir earthquake revealed by the Envisat (2005–2010) and ALOS (2007–2009) data is most consistent with afterslip on the earthquake rupture, in agreement with previous studies of early postseismic response due to large dip-slip earthquakes (e.g. *Hsu et al.*, 2002; *Yu et al.*, 2003; *Fialko*, 2009; *Reddy et al.*, 2013; *Copley et al.*, 2012; *Bie et al.*, 2013). At the same time, vertical motion of the Earth's surface in the epicentral area of several large dip-slip earthquakes might be indicative of viscoelastic relaxation several tens of years after the earthquakes (e.g. *Nishimura and Thatcher*, 2003; *Gourmelen and Amelung*, 2005). Robust constraints on the effective rheology of the lower crust and upper mantle may require long-term observations that include both the early and late phases of postseismic deformation over a broad range of epicentral distances (e.g. *Takeuchi and Fialko*, 2013). Space geodetic observations of the early postseismic deformation due to the 2005 Kashmir earthquake indicate that afterslip mainly occurred downdip of the seismogenic asperity. Spatiotemporal distribution of afterslip inferred from kinematic inversions of data spanning different epochs indicates more robust afterslip on the northern section of the fault compared to the southern section, and faster decay of afterslip on the shallow part of the fault, implying heterogeneities in the rate and state frictional properties on the earthquake rupture.

2.5 Conclusions

We analyzed the C-band Envisat and L-band ALOS interferometric synthetic aperture radar data from the epicentral area of the 2005 Mw 7.6 Kashmir (Pakistan) earthquake that occurred on the northwestern edge of Himalaya. Envisat data are available from both the descending and ascending orbits and span a time period of ∼4.5 years immediately following the earthquake (2005?2010), with nearly monthly acquisitions. Envisat data are highly decorrelated due to rugged topography and precipitation. ALOS data are available from the ascending orbit and span a time period of ∼2.5 years between 2007 and 2009, over which they remain reasonably well correlated. The mean line-of-sight postseismic velocity maps in the epicentral area of the Kashmir earthquake are derived using persistent scatterer method for Envisat data and selective stacking for ALOS data. LOS velocities from all data sets indicate an uplift (decrease in radar range), primarily in the hanging wall, of the earthquake rupture (with little uplift in the footwall) over the entire period of SAR observations (2005–2010). Modeling of viscoelastic relaxation in the lower crust and upper mantle predicts subsidence (increase in radar range) in the epicentral area and provides a lower bound on the effective viscosity of the substrate of $\sim 10^{19}$ Pas. Poroelastic rebound model predicts uplift on both sides of the fault. The available data are best explained by afterslip, possibly with minor contribution from poroelastic rebound. Inversions of InSAR and GPS data suggest that maximum afterslip occurred primarily downdip of the area

of maximum coseismic slip and that afterslip on the northern half of the fault was more pronounced compared to that on the southern half of the fault.

Acknowledgement

This work was funded by the National Science Foundation (grant EAR-1321932). We thank two anonymous reviewers and the Associate Editor for comments that improved the manuscript. Original ALOS and Envisat data are copyright by Japanese Aerospace Exploration Agency (JAXA) and European Space Agency (ESA), respectively. The data and computer codes used in this paper are available from the corresponding author.

This chapter, in full, is a reprint of the the published paper appearing as: Wang, K., and Y. Fialko (2014), "Space geodetic observations and models of post-seismic deformation due to the 2005 M7.6 Kashmir (Pakistan) earthquake", *Journal of Geophysical Research–Solid Earth* 119, 7306-7318, doi:10.1002/2014JB011122. The author of this dissertation is the primary investigator of work presented in this chapter.

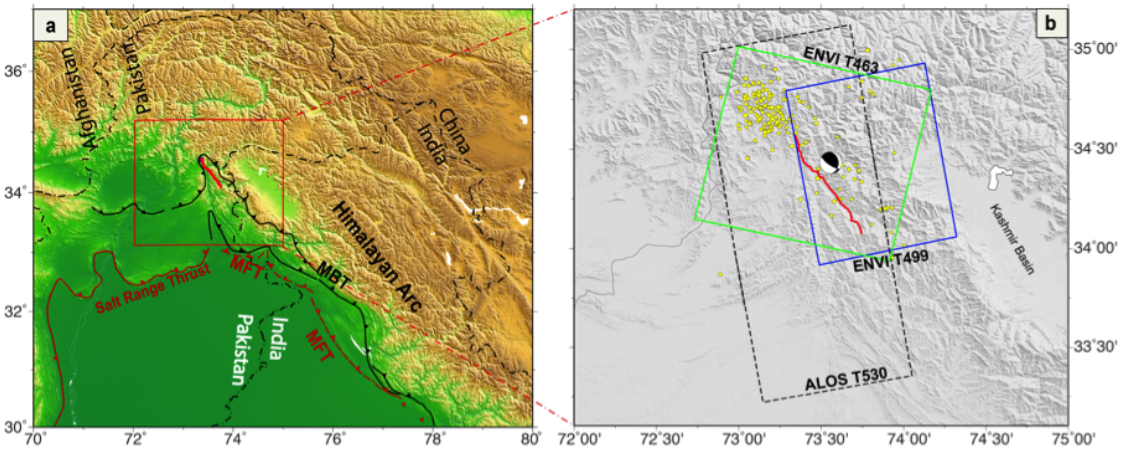

Figure 2.1: Location of the 8 October 2005 Mw 7.6 Kashmir earthquake (a) Tectonic settings of the western Himalaya. Major active faults in red are from (*Avouac et al.*, 2006). MFT = main frontal thrust; MBT = main boundary thrust (most inactive at present). (b) Location of the main shock (beach ball) and $M >$ 4.5 aftershocks. Red line denotes the surface trace of coseismic rupture derived from pixel tracking of optical images (*Avouac et al.*, 2006). Solid and dashed line boxes show the scene coverage of Envisat (blue for ascending track A499 and green for descending track D463) and ALOS (ascending track A530), respectively.

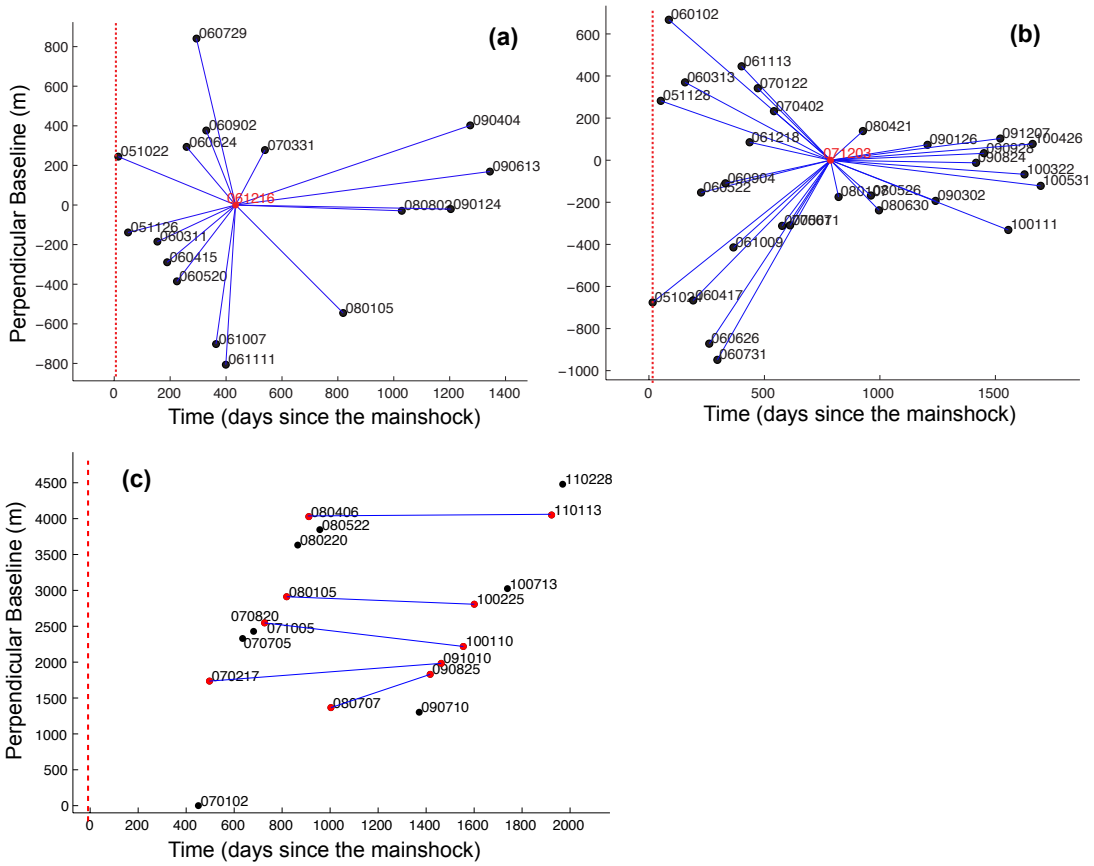

Figure 2.2: Perpendicular baseline vs. time of InSAR observations. The red dashed line in each subplot represents the time of 2005 Mw 7.6 Kashmir earthquake. The 6-digit number by each dot denotes the date of the SAR acquisition (year, month, day). For the ENVISAT tracks (a for ascending track A499; b for descending track D463), red dots denote the master scene used in the Permanent Scatterer analysis. For the ALOS track A530 (c), red dots connected by blues lines denote the interferograms used to compute the average LOS velocity.

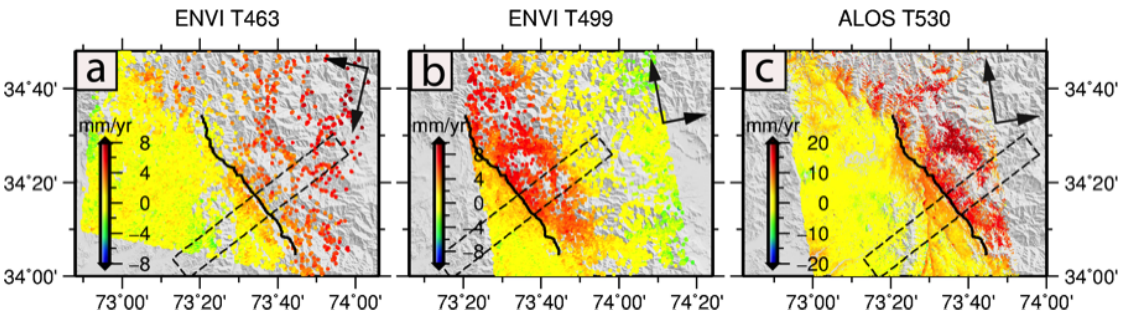

Figure 2.3: Mean line-of-sight (LOS) velocity maps of InSAR analysis of Envisat data (a and b) and selective stacking of ALOS interferograms. Positive LOS change corresponds to the surface movement toward the satellite (uplift if all deformation is vertical). Black arrows represent the satellite heading and radar look directions. Dashed black box denotes a profile shown in Figure 2.5. Note that the magnitude of LOS velocity inferred from PS InSAR analysis of Envisat data is somewhat uncertain, depending on the selection of processing parameters (see the main text for details).

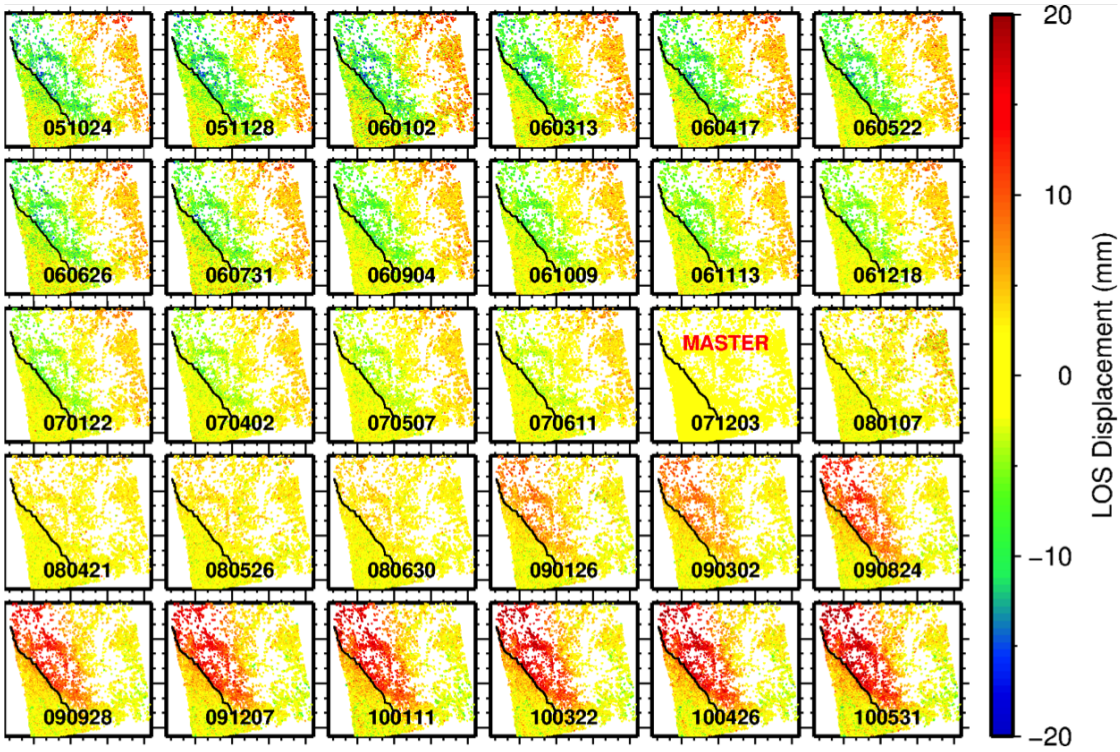

Figure 2.4: Time series of the LOS displacements derived from the PS analysis of the Envisat data for track A499. The six digits in each panel represent the date of corresponding SAR acquisition (yymmdd). Black line denotes the surface rupture trace of the 2005 Kashmir earthquake (*Avouac et al.*, 2006). The LOS displacements at each SAR acquisition epoc are relative to the time of master image (2007/12/03) used in the PS analysis.

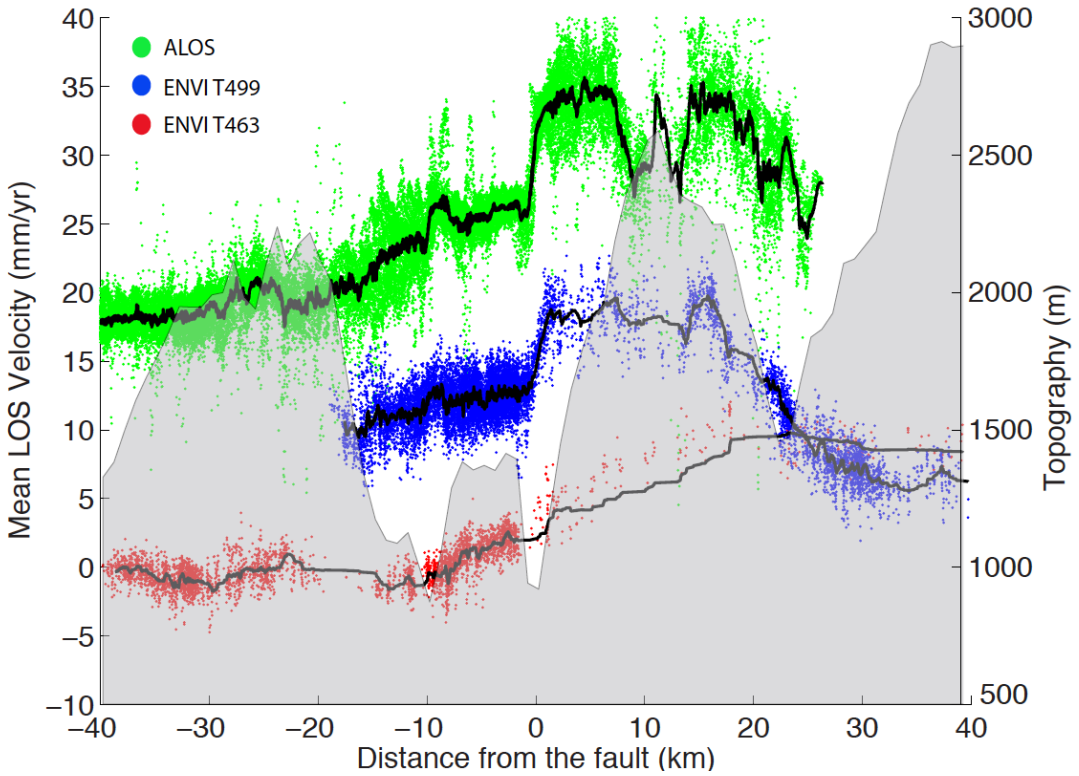

Figure 2.5: LOS velocities from different satellite tracks (colored circles) and topography (gray shading) along the profile shown by the dashed black line in Figure 2.3. The LOS velocity profiles have been shifted vertically for better visualization.

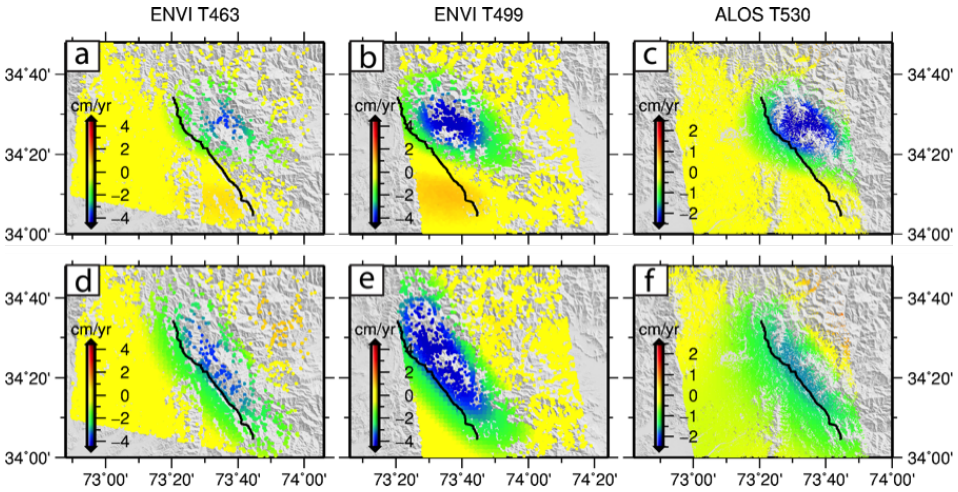

Figure 2.6: The predicted LOS velocity map is obtained by stacking the differential displacements using the intervals corresponding to the SAR interferograms. The sign convention for LOS velocities (positive for decreases in radar range and negative for increases in radar range) is the same as in Figure 2.3. Results in the top row (a–c) are based upon the coseismic slip model of *Avouac et al.* (2006), and results in bottom row (d–f) are based upon the coseismic slip model of *Yan et al.* (2013).

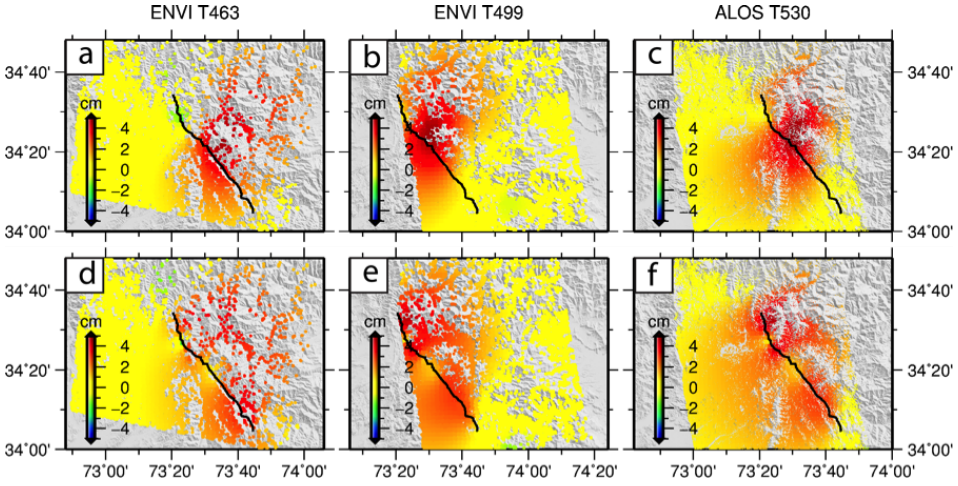

Figure 2.7: Predicted surface deformation due to the poroelastic rebound in the top 20 km of Earth's crust, calculated by differencing the coseismic deformation under undrained and drained conditons. The top three panels (a–c) are based on the coseismic slip model of *Avouac et al.* (2006), and the bottom three panels (d–f) are based upon the coseismic slip model of *Yan et al.* (2013).

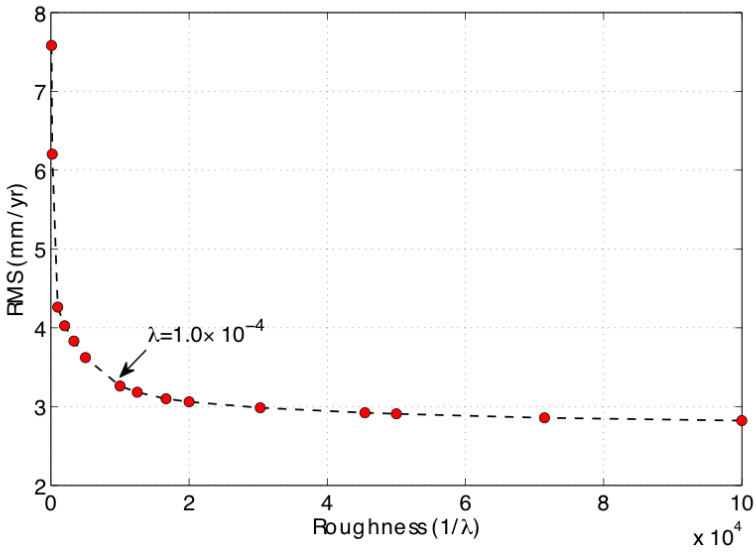

Figure 2.8: Trade-off curve of the root-mean-square (RMS) of the model misfit with ALOS data versus the roughness of the model.

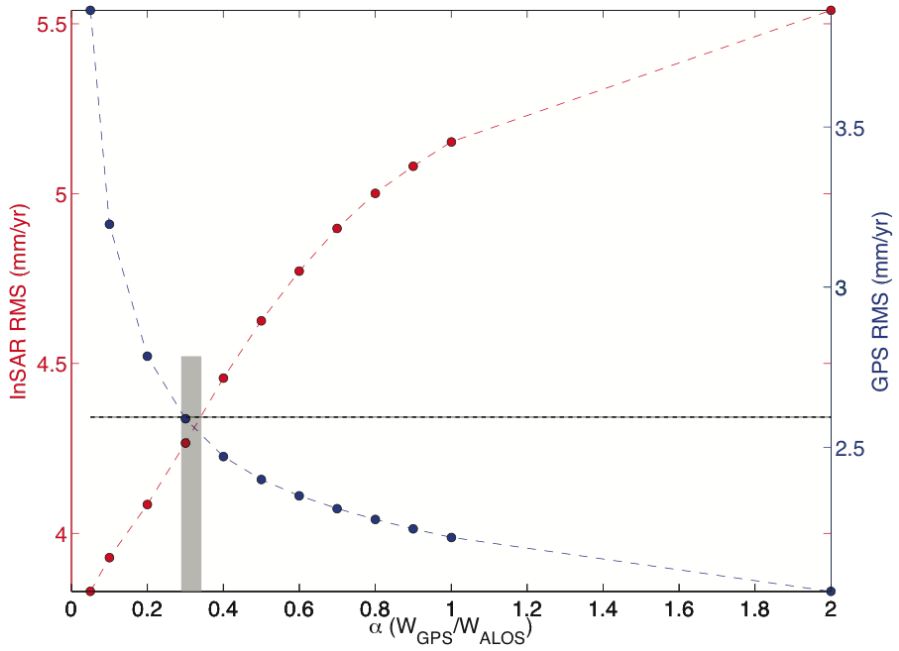

Figure 2.9: Root-mean-square (RMS) of the afterslip model for ALOS and GPS data as a function of their relative weighting in the inversion. The relative weight of ALOS data is set to be 1, and α is the relative weight of GPS data in the joint inversion. Black dashed line represents 30% increase of the RMS with respect to the minimal value. Shaded area denotes the optimal range of α in which the increase of RMS of both ALOS and GPS data are less than 30%.

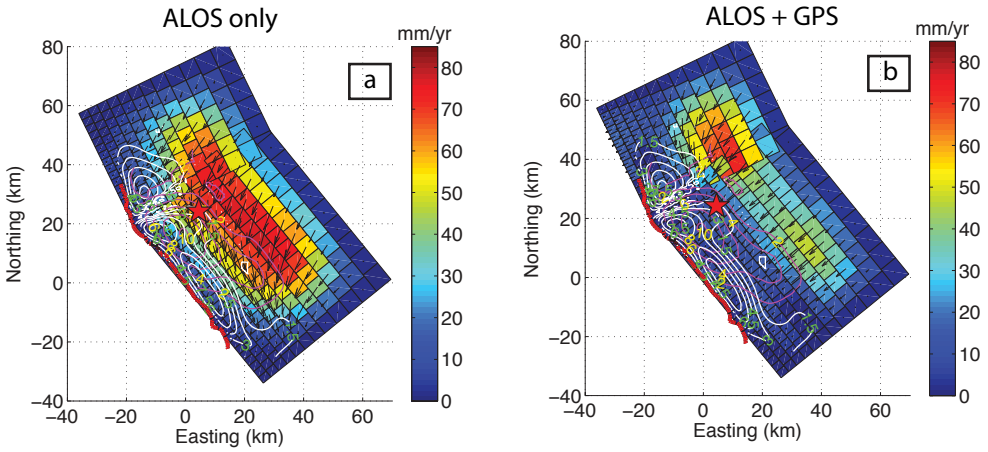

Figure 2.10: Preferred afterslip models from inversion of (a) ALOS data only and (b) joint inversion of ALOS and GPS data. Magenta lines and white lines represent the contours of coseismic slip distribution from *Avouac et al.* (2006) and *Yan et al.* (2013), respectively. Numbers inside the contours represent slip amplitude in meters. Red star denotes the epicenter of the 2005 Kashmir earthquake. Red line denotes the surface rupture trace derived from pixel-tracking analysis of optical ASTER images*Avouac et al.* (2006).

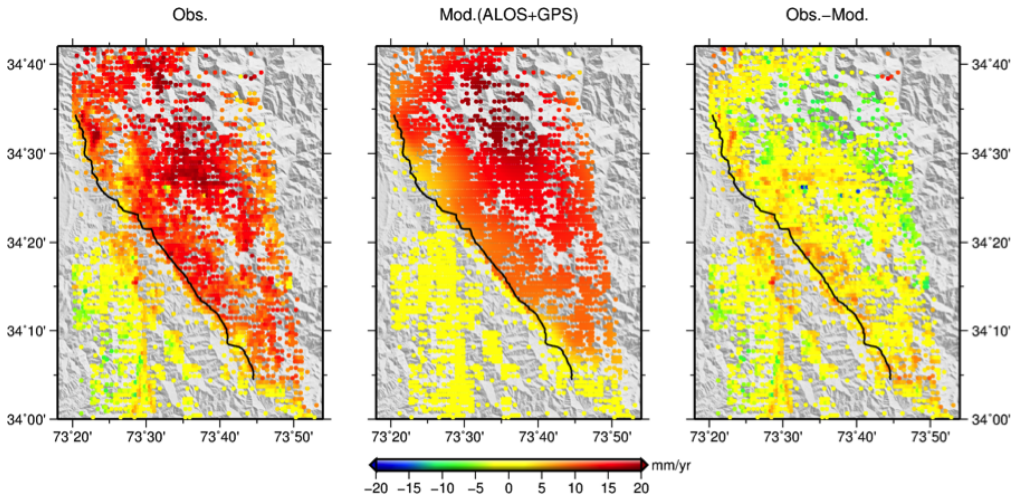

Figure 2.11: Subsampled mean LOS velocity from ALOS data and prediction of preferred afterslip model from joint inversion (Figure 2.10b) of ALOS and GPS data.

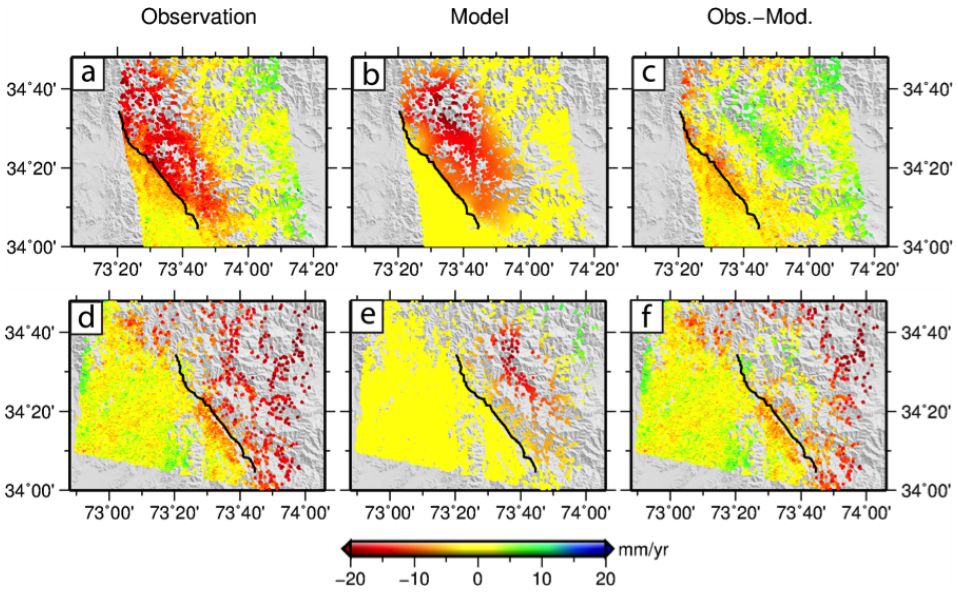

Figure 2.12: Comparison of surface deformation between Envisat observations and afterslip model predictions. The tops panels (a–c) are for the ascending track A499. The bottom panels (d–f) are for the descending track D463.

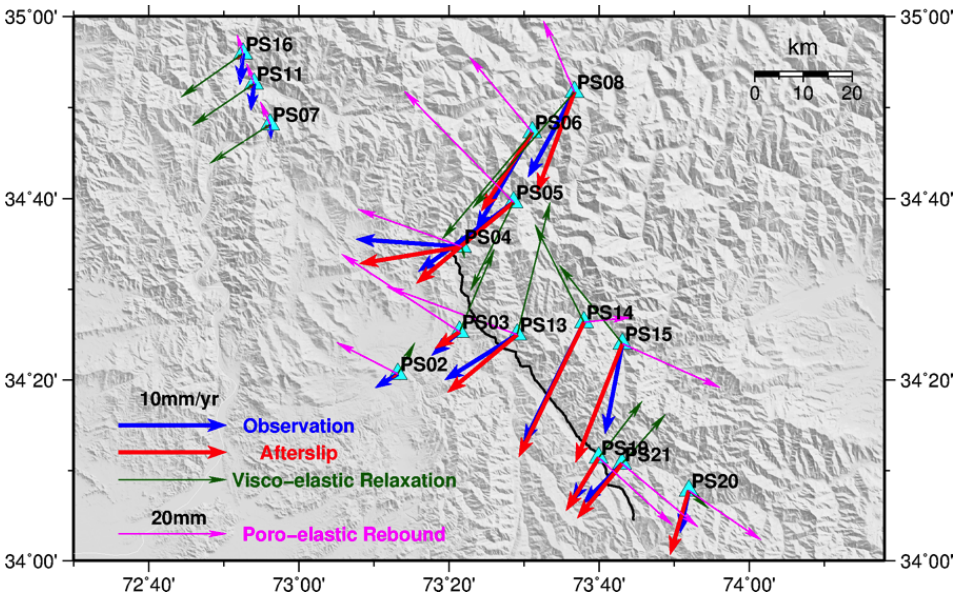

Figure 2.13: Comparison between the GPS velocities extrapolated over the time of ALOS observation period (2007–2009) and model predictions for various relaxation mechanisms. Surface velocities due to viscoelastic relaxation and displacements due to poroelastic rebound are computed using the coseismic slip model A (*Avouac et al.*, 2006). Surface velocities due to afterslip are derived from the afterslip model shown in Figure2.10b. All GPS velocities are relative to the station PS01 (not shown in this figure, see (*Jouanne et al.*, 2011)).

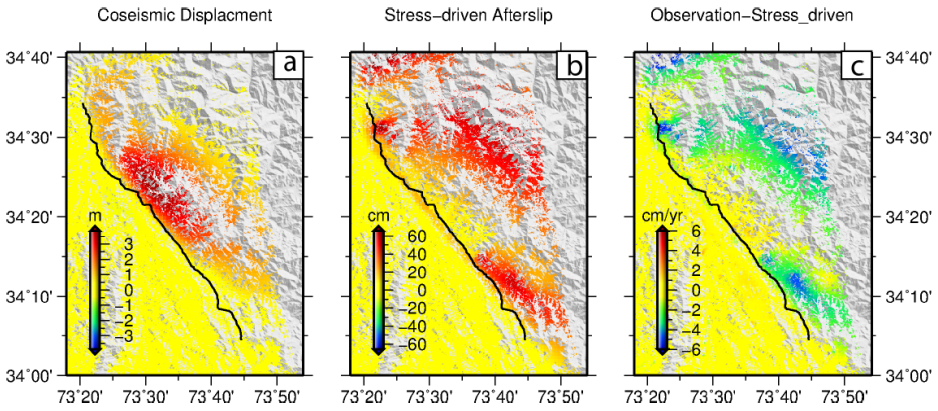

Figure 2.14: Predicted LOS displacements for the ALOS track due to (a) coseismic slip, (b) stress-driven afterslip, (c) difference between the observed postseismic deformation and prediction of the stress-driven afterslip model that might be attributed to viscoelastic relaxation. Positive LOS velocity corresponds to surface movement toward to the satellite. The coseismic displacement is based on model A (*Avouac et al.*, 2006). Surface deformation due to stress-driven afterslip is calculated using RELAX code (*Barbot et al.*, 2009).

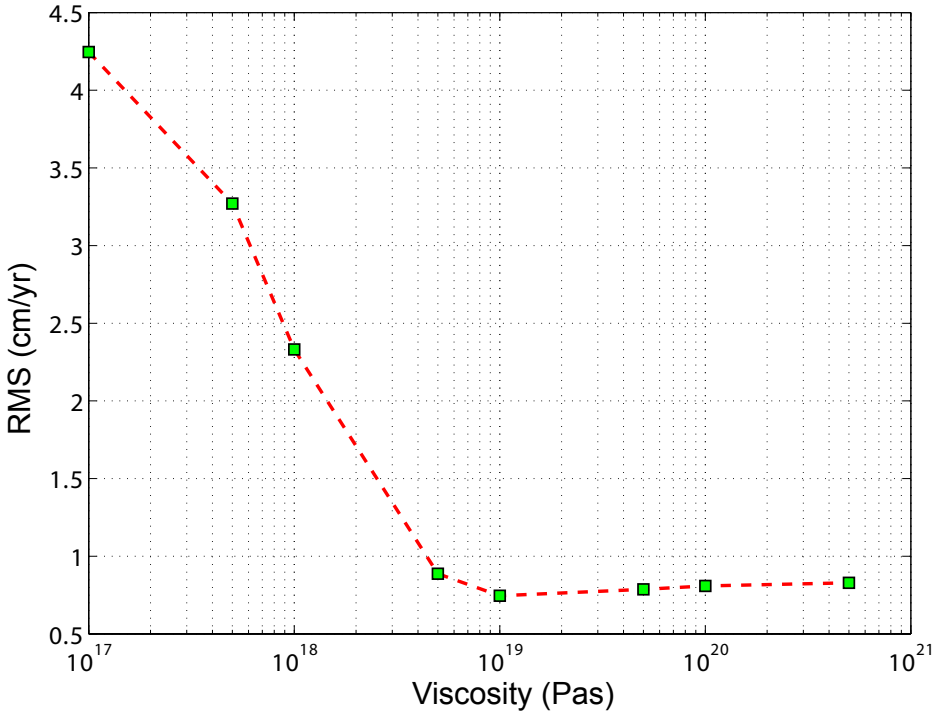

Figure 2.15: Root-mean-square (RMS) of difference between the viscoelastic model and residual LOS velocity of ALOS data (see the text) as a function of the effective viscosities in the substrate of the Kashmir region..

Bibliography

Avouac, J.-P., F. Ayoub, S. Leprince, O. Konca, and D. V. Helmberger (2006), The 2005, Mw 7.6 Kashmir earthquake: sub-pixel correlation of aster images and seismic waveforms analysis, *Earth and Planetary Science Letters*, *249*(3), 514–528.

Barbot, S., and Y. Fialko (2010), A unified continuum representation of post-seismic relaxation mechanisms: semi-analytic models of afterslip, poroelastic rebound and viscoelastic flow, *Geophysical Journal International*, *182*(3), 1124–1140.

Barbot, S., Y. Hamiel, and Y. Fialko (2008), Space geodetic investigation of the coseismic and postseismic deformation due to the 2003 Mw7. 2 Altai earthquake: Implications for the local lithospheric rheology, *Journal of Geophysical Research: Solid Earth*, *113*(B3).

Barbot, S., Y. Fialko, and Y. Bock (2009), Postseismic deformation due to the Mw 6.0 2004 Parkfield earthquake: Stress-driven creep on a fault with spatially variable rate-and-state friction parameters, *Journal of Geophysical Research: Solid Earth*, *114*(B7).

Bie, L., I. Ryder, S. E. Nippress, and R. Bürgmann (2013), Coseismic and post-seismic activity associated with the 2008 Mw 6.3 Damxung earthquake, Tibet, constrained by InSAR, *Geophysical Journal International*, *196*(2), 788–803.

Bilham, R., V. K. Gaur, and P. Molnar (2001), Himalayan seismic hazard, *Science*, *293*(5534), 1442–1444.

Bürgmann, R., and G. Dresen (2008), Rheology of the lower crust and upper mantle: Evidence from rock mechanics, geodesy, and field observations, *Annual Review of Earth and Planetary Sciences*, *36*, 531–567.

Bürgmann, R., S. Ergintav, P. Segall, E. H. Hearn, S. McClusky, R. E. Reilinger, H. Woith, and J. Zschau (2002), Time-dependent distributed afterslip on and

deep below the Izmit earthquake rupture, *Bulletin of the Seismological Society of America*, *92*(1), 126–137.

Clark, M. K., and L. H. Royden (2000), Topographic ooze: Building the eastern margin of tibet by lower crustal flow, *Geology*, *28*(8), 703–706.

Copley, A., J. Hollingsworth, and E. Bergman (2012), Constraints on fault and lithosphere rheology from the coseismic slip and postseismic afterslip of the 2006 Mw 7.0 Mozambique earthquake, *Journal of Geophysical Research: Solid Earth*, *117*(B3).

Dieterich, J. H. (1979), Modeling of rock friction: 1. experimental results and constitutive equations, *Journal of Geophysical Research: Solid Earth*, *84*(B5), 2161–2168.

Ferretti, A., C. Prati, and F. Rocca (2000), Nonlinear subsidence rate estimation using permanent scatterers in differential sar interferometry, *IEEE Transactions on geoscience and remote sensing*, *38*(5), 2202–2212.

Fialko, Y. (2004a), Evidence of fluid-filled upper crust from observations of postseismic deformation due to the 1992 Mw 7.3 Landers earthquake, *Journal of Geophysical Research: Solid Earth*, *109*(B8).

Fialko, Y. (2004b), Probing the mechanical properties of seismically active crust with space geodesy: Study of the coseismic deformation due to the 1992 Mw 7.3 Landers (southern California) earthquake, *Journal of Geophysical Research: Solid Earth (1978–2012)*, *109*(B3).

Fialko, Y. (2009), Study of postseismic deformation due to the 2006 Mw 7.0 Mozambique (east Africa) earthquake using ALOS-PALSAR data, in *3rd ALOS PI Symposium, Kona, Hawaii*, pp. 9–13.

Freed, A. M., T. Herring, and R. Bürgmann (2010), Steady-state laboratory flow laws alone fail to explain postseismic observations, *Earth and Planetary Science Letters*, *300*(1), 1–10.

Gonzalez-Ortega, A., Y. Fialko, D. Sandwell, F. Alejandro Nava-Pichardo, J. Fletcher, J. Gonzalez-Garcia, B. Lipovsky, M. Floyd, and G. Funning (2014), El Mayor-Cucapah (Mw 7.2) earthquake: Early near-field postseismic deformation from InSAR and GPS observations, *Journal of Geophysical Research: Solid Earth*, *119*(2), 1482–1497.

Gourmelen, N., and F. Amelung (2005), Postseismic mantle relaxation in the central Nevada seismic belt, *Science*, *310*(5753), 1473–1476.

Hearn, E. H., R. Bürgmann, and R. E. Reilinger (2002), Dynamics of Izmit earthquake postseismic deformation and loading of the Düzce earthquake hypocenter, *Bulletin of the Seismological Society of America*, *92*(1), 172–193.

Hooper, A., H. Zebker, P. Segall, and B. Kampes (2004), A new method for measuring deformation on volcanoes and other natural terrains using InSAR persistent scatterers, *Geophysical research letters*, *31*(23).

Hooper, A., P. Segall, and H. Zebker (2007), Persistent scatterer interferometric synthetic aperture radar for crustal deformation analysis, with application to volcán alcedo, galápagos, *Journal of Geophysical Research: Solid Earth*, *112*(B7).

Hooper, A., K. Spaans, D. Bekaert, M. C. Cuenca, M. Arıkan, and A. Oyen (2010), StaMPSs/MTI manual, *Delft Institute of Earth Observation and Space Systems Delft University of Technology, Kluyverweg*.

Hsu, Y.-J., N. Bechor, P. Segall, S.-B. Yu, L.-C. Kuo, and K.-F. Ma (2002), Rapid afterslip following the 1999 Chi-Chi, Taiwan earthquake, *Geophysical Research Letters*, *29*(16).

Jónsson, S., H. Zebker, P. Segall, and F. Amelung (2002), Fault slip distribution of the 1999 Mw 7.1 Hector mine, california, earthquake, estimated from satellite radar and GPS measurements, *Bulletin of the Seismological Society of America*, *92*(4), 1377–1389.

Jonsson, S., P. Segall, R. Pedersen, and G. Bjornsson (2003), Post-earthquake ground movements correlated to pore-pressure transients, *Nature*, *424*(6945), 179.

Jouanne, F., A. Awan, A. Madji, A. Pêcher, M. Latif, A. Kausar, J.-L. Mugnier, I. Khan, and N. Khan (2011), Postseismic deformation in Pakistan after the 8 October 2005 earthquake: evidence of afterslip along a flat north of the Balakot-Bagh thrust, *Journal of Geophysical Research: Solid Earth*, *116*(B7).

Kaneda, H., T. Nakata, H. Tsutsumi, H. Kondo, N. Sugito, Y. Awata, S. S. Akhtar, A. Majid, W. Khattak, A. A. Awan, et al. (2008), Surface rupture of the 2005 Kashmir, Pakistan, earthquake and its active tectonic implications, *Bulletin of the Seismological Society of America*, *98*(2), 521–557.

Khwaja, A. A., M. Q. Jan, R. S. Yeats, A. Hussain, and S. A. Khan (2009), New data on the Indus Kohistan seismic zone and its extension into the Hazara–Kashmir syntaxis, NW Himalayas of Pakistan, *Journal of Seismology*, *13*(3), 339–361.

LaBonte, A. L., K. M. Brown, and Y. Fialko (2009), Hydrologic detection and finite element modeling of a slow slip event in the costa rica prism toe, *Journal of Geophysical Research: Solid Earth*, *114*(B4).

Masterlark, T. (2003), Finite element model predictions of static deformation from dislocation sources in a subduction zone: sensitivities to homogeneous, isotropic, poisson-solid, and half-space assumptions, *Journal of Geophysical Research: Solid Earth*, *108*(B11).

Nishimura, T., and W. Thatcher (2003), Rheology of the lithosphere inferred from postseismic uplift following the 1959 Hebgen lake earthquake, *Journal of Geophysical Research: Solid Earth*, *108*(B8).

Okada, Y. (1985), Surface deformation due to shear and tensile faults in a half-space, *Bulletin of the Seismological Society of America*, *75*(4), 1135–1154.

Parsons, T., R. S. Yeats, Y. Yagi, and A. Hussain (2006), Static stress change from the 8 October, 2005 m=7.6 Kashmir earthquake, *Geophysical Research Letters*, *33*(6).

Pathier, E., E. Fielding, T. Wright, R. Walker, B. Parsons, and S. Hensley (2006), Displacement field and slip distribution of the 2005 Kashmir earthquake from SAR imagery, *Geophysical Research Letters*, *33*(20).

Peltzer, G., P. Rosen, F. Rogez, and K. Hudnut (1998), Poroelastic rebound along the Landers 1992 earthquake surface rupture, *Journal of Geophysical Research: Solid Earth*, *103*(B12), 30,131–30,145.

Perfettini, H., and J.-P. Avouac (2004), Postseismic relaxation driven by brittle creep: A possible mechanism to reconcile geodetic measurements and the decay rate of aftershocks, application to the Chi-Chi earthquake, Taiwan, *Journal of Geophysical Research: Solid Earth*, *109*(B2).

Pollitz, F. F., G. Peltzer, and R. Bürgmann (2000), Mobility of continental mantle: Evidence from postseismic geodetic observations following the 1992 Landers earthquake, *Journal of Geophysical Research: Solid Earth*, *105*(B4), 8035–8054.

Reddy, C., P. Sunil, R. Bürgmann, D. Chandrasekhar, and T. Kato (2013), Postseismic relaxation due to Bhuj earthquake on January 26, 2001: possible mechanisms and processes, *Natural Hazards*, *65*(2), 1119–1134.

Rousset, B., S. Barbot, J.-P. Avouac, and Y.-J. Hsu (2012), Postseismic deformation following the 1999 Chi-Chi earthquake, taiwan: Implication for lower-crust rheology, *Journal of Geophysical Research: Solid Earth*, *117*(B12).

Royden, L. H., B. C. Burchfiel, R. W. King, E. Wang, Z. Chen, F. Shen, and Y. Liu (1997), Surface deformation and lower crustal flow in eastern Tibet, *Science*, *276*(5313), 788–790.

Ruina, A. (1983), Slip instability and state variable friction laws, *Journal of Geophysical Research: Solid Earth*, *88*(B12), 10,359–10,370.

Ryder, I., B. Parsons, T. J. Wright, and G. J. Funning (2007), Post-seismic motion following the 1997 Manyi Tibet earthquake: InSAR observations and modelling, *Geophysical Journal International*, *169*(3), 1009–1027.

Ryder, I., R. Bürgmann, and F. Pollitz (2011), Lower crustal relaxation beneath the Tibetan Plateau u and Qaidam basin following the 2001 Kokoxili earthquake, *Geophysical Journal International*, *187*(2), 613–630.

Sandwell, D., R. Mellors, X. Tong, M. Wei, and P. Wessel (2011), GMTSAR: An InSAR processing system based on generic mapping tools, *Scripps Institution of Oceanography*.

Savage, J. (1990), Equivalent strike-slip earthquake cycles in half-space and lithosphere-asthenosphere earth models, *Journal of Geophysical Research: Solid Earth*, *95*(B4), 4873–4879.

Simons, M., Y. Fialko, and L. Rivera (2002), Coseismic deformation from the 1999 Mw 7.1 Hector Mine, California, earthquake as inferred from InSAR and GPS observations, *Bulletin of the Seismological Society of America*, *92*(4), 1390–1402.

Takeuchi, C. S., and Y. Fialko (2013), On the effects of thermally weakened ductile shear zones on postseismic deformation, *Journal of Geophysical Research: Solid Earth*, *118*(12), 6295–6310.

Tapponnier, P., G. King, and L. Bollinger (2006), Active faulting and seismic hazard in the western Himalayan syntaxis, Pakistan, in *International Conference on Earthquake in Pakistan: Extended Abstracts, Geological Survey of Pakistan, Quetta*, pp. 2–3.

Yan, Y., V. Pinel, E. Trouvé, E. Pathier, J. Perrin, P. Bascou, and F. Jouanne (2013), Coseismic displacement field and slip distribution of the 2005 Kashmir earthquake from SAR amplitude image correlation and differential interferometry, *Geophysical Journal International*, *193*(1), 29–46.

Yu, S.-B., Y.-J. Hsu, L.-C. Kuo, H.-Y. Chen, and C.-C. Liu (2003), GPS measurement of postseismic deformation following the 1999 Chi-Chi, Taiwan, earthquake, *Journal of Geophysical Research: Solid Earth*, *108*(B11).

Chapter 3

Slip model of the 2015 Mw 7.8 Gorkha (Nepal) earthquake from inversions of ALOS-2 and GPS data

Abstract

We use surface deformation measurements including Interferometric Synthetic Aperture Radar (InSAR) data acquired by the ALOS-2 mission of the Japanese Aerospace Exploration Agency (JAXA) and Global Positioning System (GPS) data to invert for the fault geometry and coseismic slip distribution of the 2015 M_w 7.8 Gorkha earthquake in Nepal. Assuming that the ruptured fault

connects to the surface trace of the of Main Frontal Thrust fault (MFT) between 84.34°E and 86.19°E, the best-fitting model suggests a dip angle of 7°. The moment calculated from the slip model is 6.08×10^{20} Nm, corresponding to the moment magnitude of 7.79. The rupture of the 2015 Gorkha earthquake was dominated by thrust motion that was primarily concentrated in a 150-km long zone 50 to 100 km northward from the surface trace of the Main Frontal Thrust (MFT), with maximum slip of $\sim$ 5.8 m at a depth of $\sim$8 km. Data thus indicate that the 2015 Gorkha earthquake ruptured a deep part of the seismogenic zone, in contrast to the 1934 Bihar-Nepal earthquake, which had ruptured a shallow part of the adjacent fault segment to the East.

3.1 Introduction

The M_w 7.8 Gorkha (Nepal) earthquake occurred on April 25th, 2015 in the central Himalaya, on a tectonic boundary resulted from the India-Eurasia collision. It caused more than 8000 fatalities, and was the largest seismic event since the 1956 Assam-Tibet Nepal M_w 8.6 earthquake along Himalayan arc (*Bilham et al.*, 2001). The CMT solution and preliminary finite-fault inversions of seismic data suggested that the earthquake rupture occurred along a NWW trending fault with a primarily thrust mechanism and a minor component of dextral slip. Both the CMT solution and seismically determined finite-fault models indicate that the dip angle of the fault is small (e.g. 7° in global CMT solution (*iris.edu*, 2015)

and 10° in the USGS determined finite-fault model (*earthquakes.usgs.gov*, 2015)). Geologically, the most active structure along the Himalayan arc is the Main Himalayan Thrust fault (MHT), which reaches the surface at Main Frontal Thrust fault (MFT), and absorbs about 20 mm/yr of the India-Eurasia convergence in Nepal (*Lavé and Avouac*, 2000). Analysis of GPS measurements before the Mw 7.8 Nepal earthquake indicates that the MFT is locked from surface to a distance of approximately 100 km down dip (*Ader et al.*, 2012). Most of the aftershocks of the 2015 event are located at least 30 km north of the MFT, suggesting that if the earthquake occurred along the MHT, it may not have ruptured the shallow part of the fault. It has been suggested that the MFT can be viewed as one of the splays of thrust faults rooting in a mid-crustal décollement (e.g., *Pandey et al.*, 1999; *Avouac*, 2003; *Ader et al.*, 2012). However, the geometry of the décollement (in particular, its dip angle), is not well known. In this paper, we use observations of surface deformation from Global Positioning System (GPS) and Synthetic Aperture Radar (SAR) collected by ALOS-2 satellite of the Japanese Space Agency to derive the slip distribution due to he 2015 M_w 7.8 Gorkha earthquake and constrain the geometry of the earthquake rupture.

3.2 Data and Methods

The data used in the inversion include vector displacements measured at 13 GPS stations and Line-Of-Sight (LOS) displacements derived from Synthetic

Aperture Radar (SAR) data from 3 tracks of the ALOS-2 satellite (Figure 3.1). The raw GPS data are from the network deployed by the Caltech Tectonics Observatory and processed by Advanced Rapid Imaging and Analysis (ARIA) Center for Natural Hazards at JPL (*Galetzka et al.*, 2015). Both horizontal and vertical components of the GPS displacements were used in the inversion. ALOS-2 data were processed using GMTSAR (*Lindsey et al.*, 2015). The unwrapped InSAR phase was detrended by removing a linear ramp estimated from far-field LOS displacements for each track to account for possible orbital errors and/or ionosphere variations. InSAR data were down-sampled using a recursive algorithm that enables denser sampling in areas of larger gradients in LOS displacements (*Simons et al.*, 2002; *Fialko*, 2004). To avoid over-sampling in areas with large phase gradients due to noise (atmospheric delays, decorrelation, unwrapping errors, etc.), our down-sampling of the InSAR data was implemented iteratively using model predictions (e.g. *Lohman and Simons*, 2005). An initial slip model was estimated from inversion of coarsely sampled LOS displacement maps. Synthetic interferograms were computed using the slip model, and down-sampled using the quad-tree curvature-based algorithm. The bounding coordinates of each resolution cell (bin) were then used to compute the average LOS displacements from the observed interferograms. A new slip model was then derived from the updated dataset. Usually, a few iterations are sufficient to achieve a solution that stops changing with subsequent iterations. To avoid spurious shallow slip, a relatively dense sampling around the fault trace was retained through all iterations. Figure 3.2 shows the

down-sampled LOS displacements from 3 tracks of ALOS-2 data that are used in the inversion. The radar incidence angles were computed by averaging the original values in respective resolution cells.

Our kinematic inversions assumed that fault slip can be approximated by a superposition of rectangular dislocations in a homogeneous elastic half-space (*Okada*, 1985). The fault geometry was constrained by the assumption that the rupture plane intersects the surface along the MFT between 84.34°E and 86.19°E. The $\sim$ 185 km long and 160 km wide fault was divided into patches which sizes gradually increase with depth to ensure a relatively uniform model resolution (e.g. *Fialko*, 2004). Each individual patch was allowed to have a thrust and a right-lateral slip component of up to 10 m. Laplacian smoothing was applied between adjacent fault patches to avoid abrupt variations in slip. We further regularized the inversion problem by requiring no slip at the fault edges (except at the surface). We determined the optimal values of smoothness of the model and relative weighting between GPS and InSAR LOS data as described by *Wang and Fialko* (2014). The selection of the smoothness and relative weighting between ALOS-2 and GPS data used in this study is shown in Figure 3.3.

The initial inversions were performed assuming a dip angle of 10°. However, we found that the best-fitting model failed to provide a good fit to data from the ascending and descending tracks (T147 and T048) simultaneously, regardless of what model parameters (e.g. degree of smoothing or relative weighting between GPS and InSAR data sets) were chosen. We then allowed the dip angle to vary

in the range of 1° - 15°, and solved for the slip distribution for each assumed geometry. For each run, we quantified the misfit between the model and the data by calculating

$$\chi^2 = \frac{1}{N}\sum_{i=1}^{N}(\frac{d_i - d_i'}{\sigma_i})^2 \tag{3.1}$$

where d and d' represent vectors of observations and model predictions, respectively; σ represents the corresponding uncertainty for each dataset (LOS displacements from 3 ALOS-2 tracks and horizontal displacements at 13 GPS sites); N is the length of the data vector. Uncertainties in InSAR data were estimated by computing the variation of the LOS displacements in the far field of each interferogram, where the deformation due to earthquake is expected to be negligible. The estimated Root-Mean-Square (RMS) of the LOS displacements in the far field are 2.3, 5.4 and 4.1 cm for track T047, T048 and T157, respectively. We note that the variation estimated this way only provides a qualitative measure of accuracy of the InSAR measurements, and does not reflect the uncertainty of individual data points. The GPS uncertainties are computed as part of the GPS solutions, and are mostly < 3 mm for horizontal components and < 1 cm for vertical component.

3.3 Results

We found that a model with a dip angle of 7° fits the LOS displacements from of all 3 ALOS-2 tracks as well as GPS data very well, with a low misfit of $\chi^2 = 1.1561$. The preferred coseismic slip model is shown in Figure 3.4. The model

is characterized by dominantly thrust slip, with minor contribution of dextral component, concentrated in a relatively narrow (compared to the along-strike rupture dimension) zone between $\sim$ 50 and $\sim$ 100 km along the down-dip direction. The maximum slip is $\sim$ 5.8 m at a depth of $\sim$ 8 km with respect to sea level. The total moment is $6.08 \times 10^{20} Nm$, corresponding to a moment magnitude of $M_w = 7.79$, in excellent agreement with the seismic moment (*earthquakes.usgs.gov*, 2015). The slip on the central part of the rupture seems to have extended further down-dip, compared to both the eastern and western tips of the rupture that appear to taper to a width of 20-30 km (see Figures 3.4 and 3.8). Most of the aftershocks occurred along the eastern half of the fault, around the patches of relatively large coseismic slip, including the M_w 7.3 aftershock on May 12th, 2015 (magenta circle in Figure 3.4).

Figure 3.5 shows a comparison of the ALOS-2 data with predictions of the best-fitting slip model (Figure 3.4). The model is able to reproduce InSAR measurements from all 3 tracks (Figure 3.5) as well as GPS measurements (Figure 3.1).

It was suggested that the MHT geometry involves two ramp-flats, with the top flat lying at $\sim$ 5 to 10 km depth (*Avouac*, 2003). To allow for listric (curved) fault geometry, we performed another set of inversions in which the fault surface was parameterized as :

$$z = -\frac{2a}{\pi} \arctan \frac{y}{b} \tag{3.2}$$

where z is the depth of the fault at a distance of y from the surface trace (i.e. MFT); a and b are geometric parameters that were varied in the inversion. Specifically, a represents the depth of the fault at infinite distance from the surface trace (corresponding to the depth of the flat in the ramp-flat décollement system), while b controls the fault curvature near the surface (corresponding to the geometry of the ramp in the ramp-flat décollement system). A planar fault is particular case of equation (2), given sufficiently large b. Using the same parameters for smoothness and relative weighting between datasets as before, we inverted for the slip distribution on a curve fault described by equation (3.2) for a range of values of $a \in [1 : 1 : 30]$ km and $b \in [1 : 10 : 300]$ km. The slip model yields the lowest misfit of $\chi^2_{curved} = 1.0349$ for $a = 18$ km and $b = 81$ km. This can be compared with $\chi^2_{planar} = 1.1561$ for the case of a planar fault, suggesting that a ramp-flat décollement model is in better agreement with surface deformation data. The overall slip distribution based on the curved fault is quite similar to that of a planar fault with a dip angle of 7° (Figure 3.4). The two models are very similar down to depth of 10 km, where most of coseismic slip occurred (Figure 3.6). We also ran a suite of inversions in which we relaxed the assumptions that the fault plane intersects the surface at the trace of MFT. In these inversions, the fault strike was fixes at 285 °, and the fault was required to go through an assumed hypocenter. Because the hypocenter depth is only approximately constrained by seismic data, we allowed it to vary between 4 and 20 km. The fault dip was allowed to vary between 1 to 15 degrees. The model misfits are shown in Figure 3.7, and the family of

fault geometries that fit the data equally well are shown by gray lines in Figure 3.6. The respective slip distribution is quite similar to that of the planar fault that intersects the surface at the location of MFT. The best-fitting geometries are close to sub-surface geometries of the MHT suggested by previous studies (*Avouac*, 2003; *Nábělek et al.*, 2009). Somewhat shallower depths of the geodetic models compared to the inferred geometries of the MHT (Figure 3.6) might be attributed to the neglect of increases in elastic rigidity with depth (e.g. *Fialko*, 2004). However, we note that the seismically determined origin depth is in better agreement with the best-fitting geodetic models than with the previously suggested geometry of the MHT (Figure 3.6). The geodetically inferred dip angles are in fact an upper bound, as model does not take into account surface topography. The average slope due to topography across the MHT is 2 to 5 degrees (Figure 3.6), and a half-space model is expected to bias the dip angle (measured with respect to the horizontal) by a value of the order of the topographic slope. More sophisticated simulations that take into account surface topography are needed to refine the slip model of the 2015 Gorkha earthquake.

3.4 Discussion

Seismicity along the Himalayan arc is known to occur along a relatively narrow zone which follows the front of high Himalaya, and tends to shut off underneath the higher Himalaya (elevations higher than 3500 m, see the gray line in

Figure 3.4) (e.g. *Pandey et al.*, 1995, 1999; *Avouac*, 2003). The coseismic slip due to the 2015 M_w 7.8 Nepal earthquake is also concentrated in a fairly narrow zone (between $\sim$ 50 and $\sim$ 100 km) from the MFT at the deep end of the seismogenic zone. The extent of interseismic locking at $\sim$ 100 km north of the MFT likely marks the brittle-ductile transition and changes in rate dependence of friction due to eh elevated pressure and temperature.

Our slip model shows that the 2015 rupture did not propagate into shallow part of the MHT. Analysis of GPS measurements made before the earthquake indicates that the MHT is locked from surface to a distance of approximately 100 km down dip (*Ader et al.*, 2012). Recent investigations of the Quaternary geomorphology along the MFT showed that at least two great earthquakes had ruptured to the surface in Nepal in the past 1000 years (*Sapkota et al.*, 2013). Particularly, the 1934 Bihar-Nepal M 8.2 earthquake ruptured a $\sim$ 150 km-long segment of the MFT between 85.8° E and 87.3° E, immediately to the east of the 2015 rupture (Figure 3.8). Unless the degree of seismic coupling varies along the fault strike , the lack of shallow slip during the 2015 Gorkha earthquake implies future seismic hazard, in particular because this part of the fault has been brought closer to failure by the 2015 earthquake. Observations of post-seismic deformation (in particular, the occurrence of afterslip on the upper section of the MFT) will provide important constraints on the degree of seismic coupling and seismic hazard on this part of this fault.

3.5 Conclusions

We used the surface displacement data provided by GPS and InSAR to model the coseismic slip distribution and fault the geometry of the 2015 M_w 7.8 Gorkha earthquake in Nepal. Aftershocks of the 2015 event were mostly surrounding the areas of high coseismic slip. The best-fitting model suggests a shallow dip angle of 7° for the MHT. The 2015 Gorkha earthquake ruptured the deep part of the seismogenic zone, with little or no slip in the shallow part (within 50 km from the MFT). This is in contrast to the 1934 Bihar-Nepal event, whose rupture had likely reached the surface, implying increased seismic hazard on the fault section updip of the 2015 event.

Acknowledgement

We thank Jean-Philippe Avouac, Rebecca Bendick and the Associate Editor for their thoughtful reviews. This work was funded by the National Science Foundation grant EAR-1321932. Original ALOS-2 data are copyright by Japanese Aerospace Exploration Agency (JAXA). The data and computer codes used in this paper are available form the corresponding author.

This chapter, in full, is a reprint of the published paper appearing as: Wang, K., and Y. Fialko (2015), "Slip model of the 2015 Mw 7.8 Gorkha (Nepal) earthquake from inver- sions of ALOS-2 and GPS data", *Geophysical Research Letters*, 42, 7452-7458, doi:10.1002/2015GL065201. The author of this dissertation is the

primary investigator of work presented in this chapter.

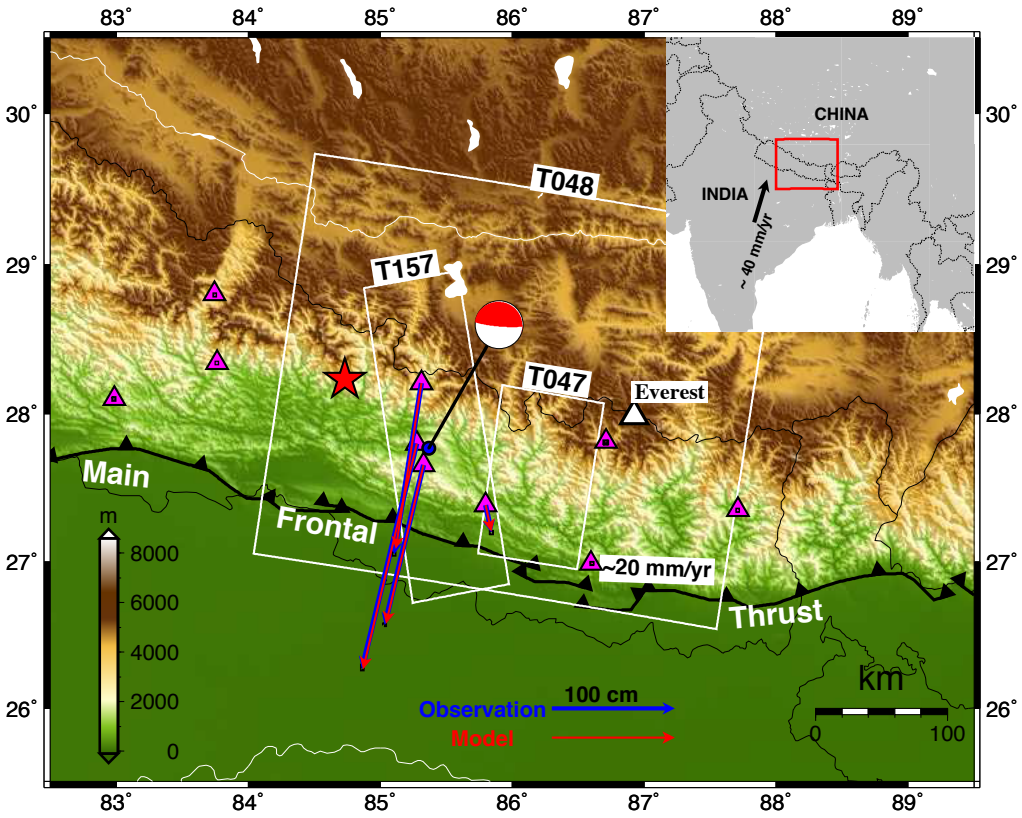

Figure 3.1: Tectonic setting of the 25 April, 2015 Mw 7.8 Nepal earthquake.Thick black line represents the surface trace of the Main Frontal Thrust (MFT) (*Ader et al.*, 2012). The red star denotes the epicenter *earthquakes.usgs.gov* (2015), and the beachball denotes the Centroid Moment Tensor *iris.edu* (2015) of the Mw 7.8 mainshock. White boxes show the coverage of ALOS-2 data (ascending track T157, descending track T048, and 5th sub-swath of descending track T047). Blue and red arrows represent the observed and modeled horizontal surface displacements at GPS sites (magenta triangles)

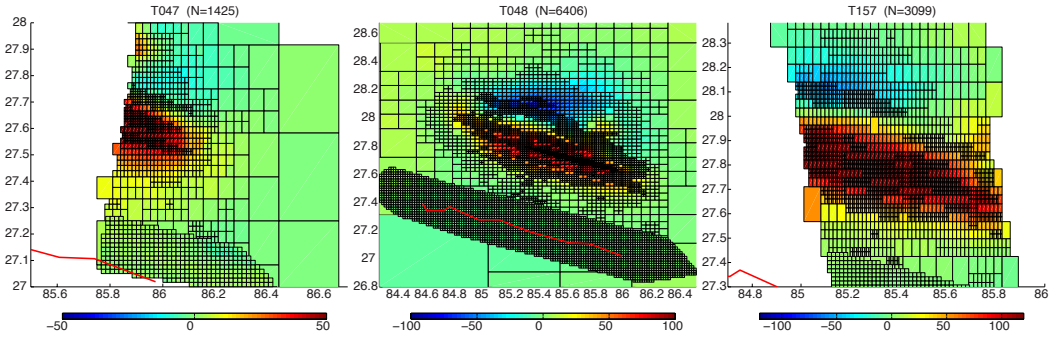

Figure 3.2: Down-sampling of InSAR measurements Data are averaged in each bounding box (bin). Total number of points obtained after down-sampling is indicated in parenthesis in the subtitles. The red solid line in each panel denotes the surface trace of MFT corresponding to the 2015 Gorkha rupture.

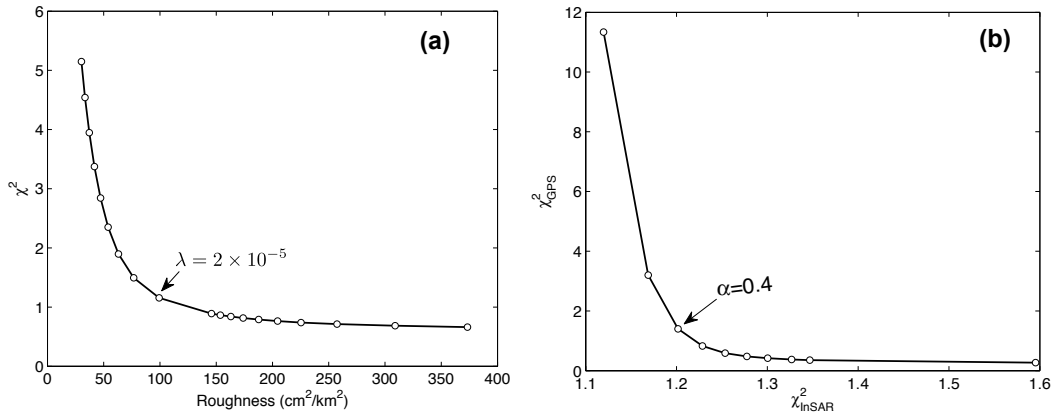

Figure 3.3: Determination of the smoothness and relative weighting between datasets in the inversion of the coseismic slip model of the 2015 Gorkha earthquake. (a) Trade-off curve of the model misfit versus the roughness of the model. The inversion is minimizing the objective function $F(m, \lambda) = \| Gm - d \| + \lambda \| Hm \|$, where m is the vector of unknown (slip) components, d is the data vector, G is the matrix of Green's function, H is the finite difference approximation of the Laplacian operator used to smooth the model. Here we defined the roughnes of the model as $r = \| Hm \|^2 / S$, where S is the total area of the fault model. $\lambda = 2 \times 10^{-5}$ was chosen as the optimal value in the inversion. (b) Tradeoff-curve of the GPS misfit χ^2_{GPS} versus InSAR misfit χ^2_{InSAR}. The ratio of relative weighting of GPS data to that of InSAR data α was chosen such that the χ^2_{GPS} is close to one (i.e. average misfit of the model is commensurate with the measurement uncertainty), while χ^2_{InSAR} is smallest. $\alpha = 0.4$ was chosen as the optimal value in the inversion.

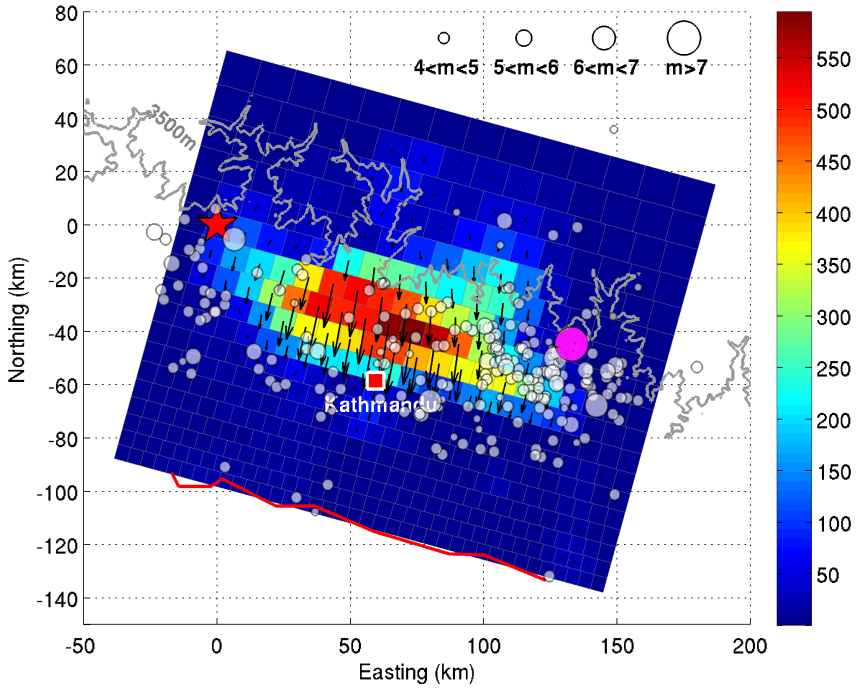

Figure 3.4: Surface projection of the coseismic slip model of the 25 April M_w 7.8 Gorkha earthquake. Red line represents the surface trace of MFT used to constrain the strike of the fault plane. Red star denotes the epicenter of the M_w 7.8 mainshock. Gray dots denote the aftershocks of $m > 4$ from 25 April to 31 May, 2015. The M_w 7.3 aftershock of May 12th, 2015 is shown by a magenta circle. Color shows the slip magnitude in cm, and arrows correspond to the slip directions. The gray line represents the surface elevation of 3500m. Red square denotes the city of Kathmandu. The origin corresponds to the epicenter of the mainshock (84.731°E, 28.230°N)

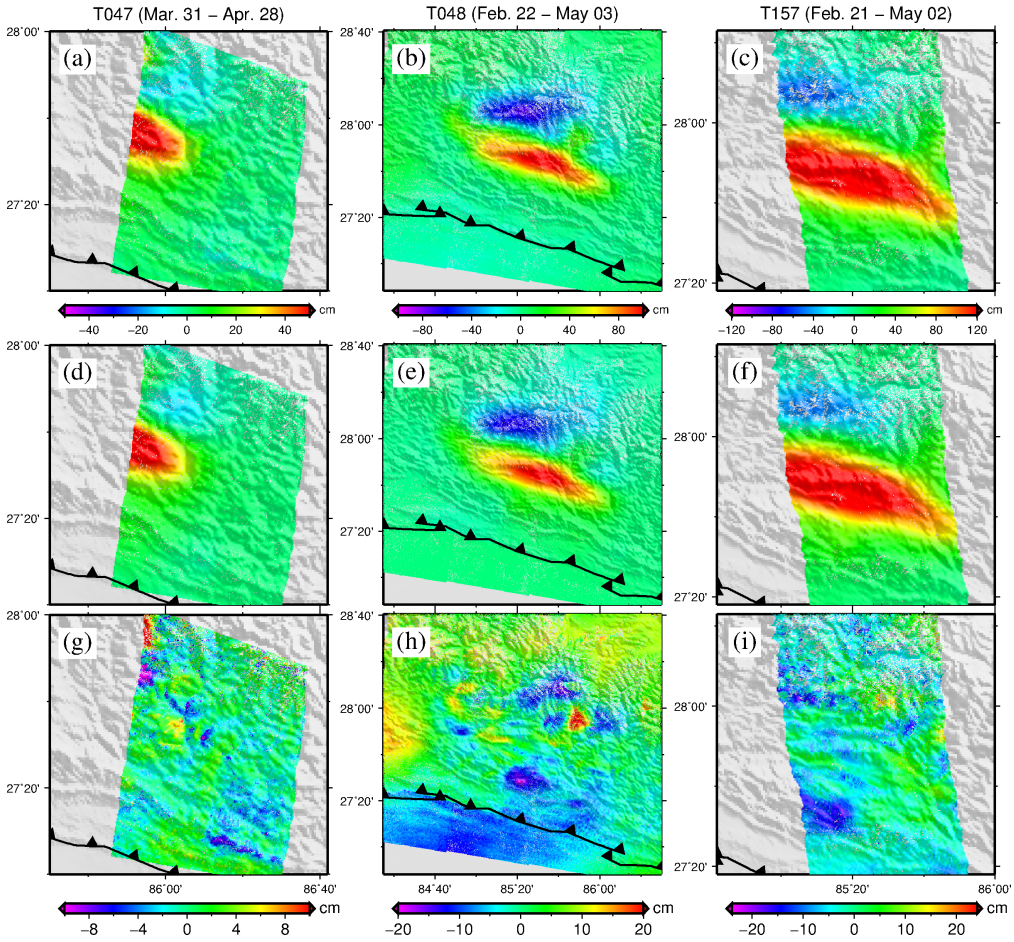

Figure 3.5: Comparison of observed and modeled LOS displacements from 3 ALOS-2 tracks. The forward calculation is based on a model assuming a planar fault with the dip angle of 7° that intersects the surface at the trace of MFT (Figure 2). The top (a–c), middle (d–e) and bottom (g–i) panels are observations, model predictions and residuals, respectively. Note the differences in color scales between the data/models and the residuals. Sub-titles denote the track numbers and SAR acquisition dates (in parentheses; all in year 2015)

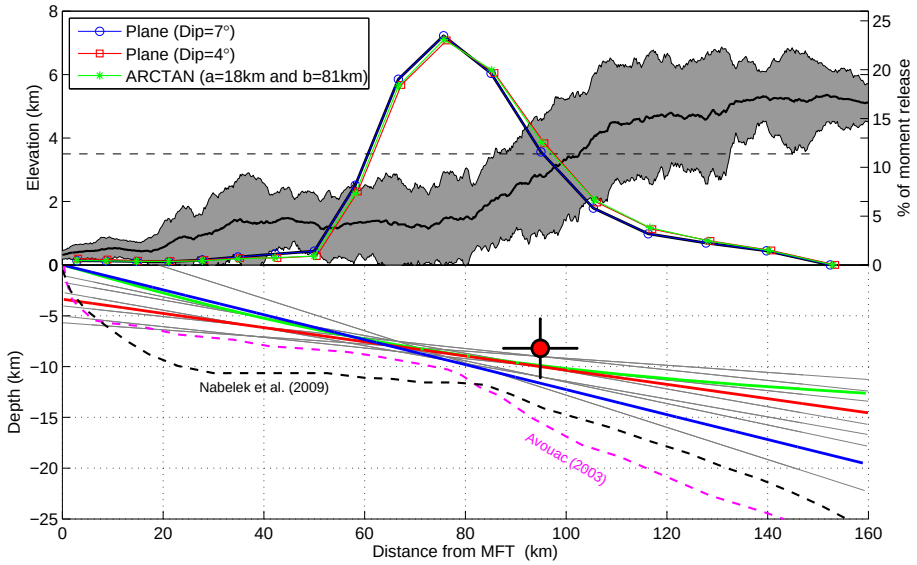

Figure 3.6: Comparison of slip models assuming planar and curved fault geometry. (a) moment release and topography along dip direction. The shaded gray area shows the elevation variations along the direction normal to the average strike of MFT (285°) as marked by red line in Figure 3.4. The blue red and green lines show the percentages of moment release as a function of distance from MFT for the three best-fitting fault geometries. (b) geometries of the fault models at depth (blue for planar fault of dip angle of 7° that intersects the surface at MFT, green for curved fault approximated by an arctan function, red for planar fault with dip angle of 4°). Thin gray lines represent the geometries of planar faults yielding low misfits (see Figure 3.7)

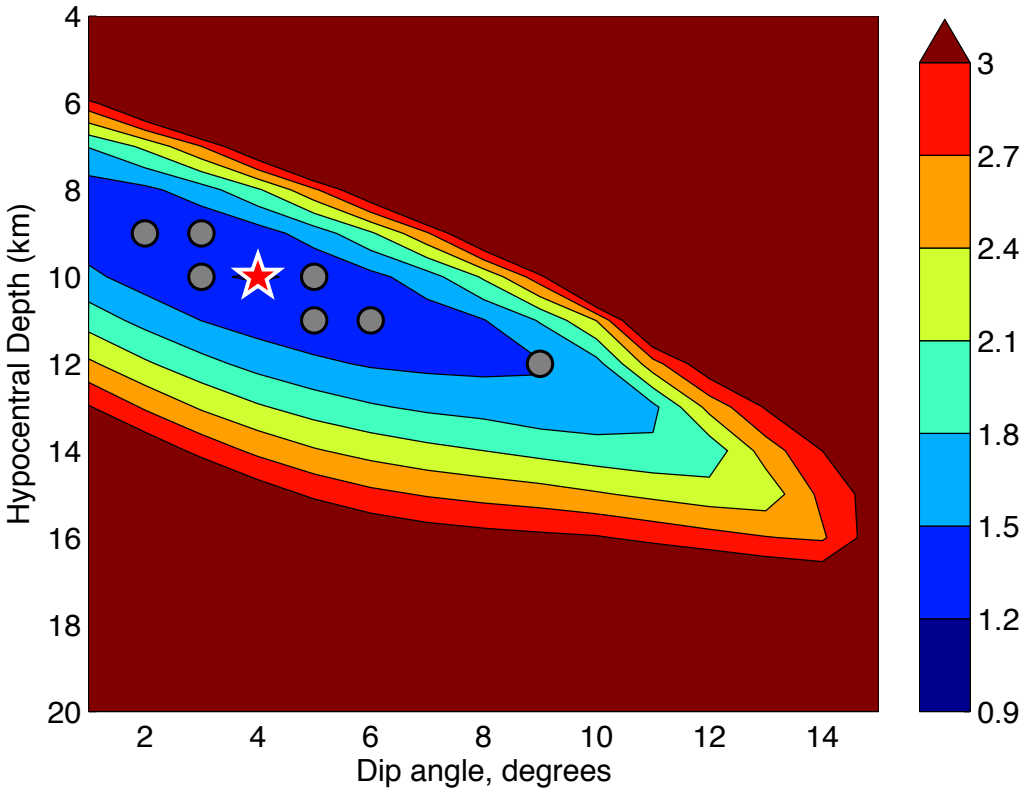

Figure 3.7: Model misfit as a function of 'hypocentral' depth and dip angle. The fault strike was fixed at 285 degree, and the fault was required to go through assumed hypocenter, which was allowed vary between 4 and 20 km. The fault dip was allowed between 1 to 15°.

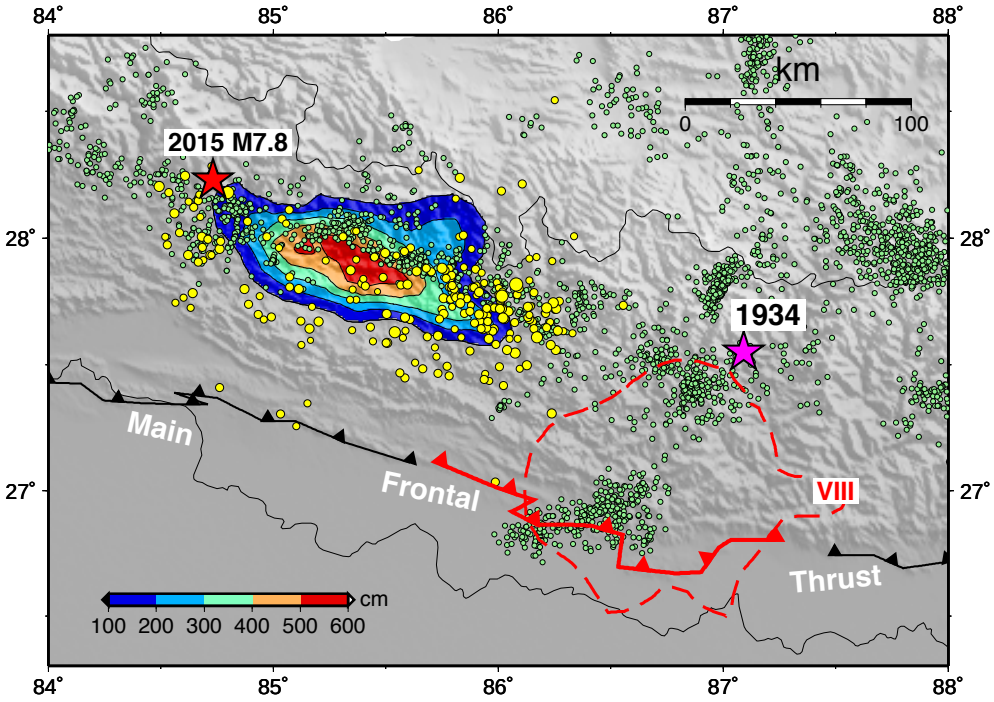

Figure 3.8: Spatial relationship between the 2015 M_w 7.8 Gorkha earthquake and the 1934 M_w 8.6 Bihar-Nepal earthquake. Color represents the coseismic slip of the 2015 event. Yellow dots denote the aftershocks of the 2015 event from April 25, 2015 to May 31 2015. Lightgreen dots denote the background seismicity from 1995 to 2002 (*Ader et al.*, 2012). Red solid and dashed lines represent the inferred rupture segment and the isoseismal intensity of VIII of the 1934 Bihar-Nepal earthquake, respectively (*Sapkota et al.*, 2013). Magenta star denotes the relocated epicenter of the 1934 event (*Chen and Molnar*, 1977).

Bibliography

Ader, T., J.-P. Avouac, J. Liu-Zeng, H. Lyon-Caen, L. Bollinger, J. Galetzka, J. Genrich, M. Thomas, K. Chanard, S. N. Sapkota, S. Rajaure, P. Shrestha, L. Ding, and M. Flouzat (2012), Convergence rate across the Nepal Himalaya and interseismic coupling on the Main Himalayan Thrust: Implications for seismic hazard, *Journal of Geophysical Research*, *117*(B4), B04,403.

Avouac, J.-P. (2003), Mountain building, Erosion, and the seismic cycle in the Nepal himalaya, *Advances in Geophysics*, *Elsevier*, 1–80.

Bilham, R., V. K. Gaur, and P. Molnar (2001), Earthquakes: Himalayan Seismic Hazard, *293*(5534), 1442–1444.

Chen, W.-P., and P. Molnar (1977), Seismic moments of major earthquakes and the average rate of slip in central Asia, *Journal of Geophysical Research*, *82*(20), 2945–2969.

earthquakes.usgs.gov (2015), Earthquake hazard program, *http://earthquake.usgs.gov/earthquakes/eventpage/us20002926#general_summary, (Accessed 30 June 2015)*.

Fialko, Y. (2004), Probing the mechanical properties of seismically active crust with space geodesy: Study of the coseismic deformation due to the 1992 Mw 7.3 Landers (southern California) earthquake , *Journal of Geophysical Research*, *109*(B3).

Galetzka, J., D. Melgar, J. F. Genrich, J. Geng, S. Owen, E. O. Lindsey, X. Xu, Y. Bock, J. P. Avouac, L. B. Adhikari, B. N. Upreti, B. Pratt-Sitaula, T. N. Bhattarai, B. P. Sitaula, A. Moore, K. W. Hudnut, W. Szeliga, J. Normandeau, M. Fend, M. Flouzat, L. Bollinger, P. Shrestha, B. Koirala, U. Gautam, M. Bhatterai, R. Gupta, T. Kandel, C. Timsina, S. N. Sapkota, S. Rajaure, and N. Maharjan (2015), Slip pulse and resonance of the Kathmandu basin during the 2015 Gorkha earthquake, Nepal, *Science*, *349*(6252), 1091–1095.

iris.edu (2015), Moment Tensor for MW 7.9 (GCMT) NEPAL, *http://ds.iris.edu/spud/momenttensor/9925741, (Accessed 30 June 2015).*

Lavé, J., and J.-P. Avouac (2000), Active folding of fluvial terraces across the Siwaliks hills, Himalayas of central nepal, *Journal of Geophysical Research*, *105*(B3), 5735–5770.

Lindsey, E., R. Natsuaki, X. Xu, M. Shimada, M. Hashimoto, and D. Sandwell (2015), Line-of-sight displacement from ALOS-2 interferometry: Mw 7.8 Gorkha Earthquake and Mw 7.3 aftershock, *Geophysical Research Letters*, *42*, 6655-6661.

Lohman, R. B., and M. Simons (2005), Some thoughts on the use of InSAR data to constrain models of surface deformation: Noise structure and data downsampling, *Geochemistry, Geophysics, Geosystems*, *6*(1), Q01,007.

Nábělek, J., G. Hetényi, J. Vergne, S. Sapkota, B. Kafle, M. Jiang, H. Su, J. Chen, B.-S. Huang, and H.-C. Team (2009), Underplating in the Himalaya-Tibet Collision Zone Revealed by the Hi-CLIMB Experiment, *Science*, *325*(5946), 1371–1374.

Okada, Y. (1985), Surface deformation due to shear and tensile faults in a half-space, *Bulletin of the Seismological Society of America*, *75*(4), 1135–1154.

Pandey, M. R., R. P. Tandukar, J. P. Avouac, J. Lavé, and J. P. Massot (1995), Interseismic strain accumulation on the Himalayan crustal ramp (Nepal), *Geophysical Research Letters*, *22*(7), 751–754.

Pandey, M. R., R. P. Tandukar, J. P. Avouac, J. Vergne, and T. Héritier (1999), Seismotectonics of the Nepal Himalaya from a local seismic network, *Journal of Asian Earth Sciences*, *17*(5-6), 703–712.

Sapkota, S. N., L. Bollinger, Y. Klinger, and P. Tapponnier (2013), Primary surface ruptures of the great Himalayan earthquakes in 1934 and 1255, *Nature Geoscience*, *6*(2), 152–152.

Simons, M., Y. Fialko, and L. Rivera (2002), Coseismic Deformation from the 1999 Mw 7.1 Hector Mine, California, Earthquake as Inferred from InSAR and GPS Observations, *Bulletin of the Seismological Society of America*, *92*(4), 1390–1402.

Wang, K., and Y. Fialko (2014), Space geodetic observations and models of post-seismic deformation due to the 2005 M7.6 Kashmir (Pakistan) earthquake, *Journal of Geophysical Research: Solid Earth*, *119*(9), 7306–7318.

Chapter 4

Observations and modeling of co- and post-seismic deformation due to the 2015 Mw 7.8 Gorkha (Nepal) earthquake

Abstract

We use space geodetic data to investigate the co- and postseismic deformation due to the 2015 M_w 7.8 Gorkha earthquake that occurred along the central Himalayan arc. Because the earthquake area is characterized by strong variations in surface relief and material properties, we developed finite element models that explicitly account for topography and 3-D elastic structure. Compared to slip

models that are based on analytic solutions for dislocations in a homogeneous elastic half-space, models including elastic heterogeneity and topography exhibit somewhat larger (up to ∼10%) slip amplitude. GPS observations spanning ∼2 years following the earthquake show overall southward movement and uplift in the epicentral area, qualitatively similar to the coseismic deformation pattern. We computed the line-of-sight (LOS) displacement histories from 3 tracks of the Sentinel-1A/B Interferometric Synthetic Aperture Radar (InSAR) satellite, using Persistent Scatter (PS) method. InSAR observations reveal an uplift of up to ∼70 mm over ∼20 months after the mainshock, concentrated primarily at the downdip edge of the ruptured asperity. Kinematic inversions of GPS and InSAR data, and forward models of stress-driven creep indicate that the observed postseismic transient is dominated by afterslip on a down-dip extension of the seismic rupture. The Main Himalayan Thrust (MHT) updip of the 2015 rupture remained locked after the earthquake, indicative of future seismic hazard. A poro-elastic rebound may have contributed to the observed uplift and southward motion, but the predicted surface displacements are small (on the order of 10 mm or less). We also tested a wide range of visco-elastic relaxation models, including 1-D and 3-D variations in the viscosity structure. All tested visco-elastic models predict opposite signs of horizontal and vertical displacements compared to those observed. Available surface deformation data appear to rule out the hypothesis of a low viscosity channel beneath the Tibetan Plateau which has been invoked to explain the long-term uplift and variations in topography at the plateau margins.

4.1 Introduction

The 2015 M_w 7.8 Gorkha (Nepal) earthquake occurred along the central Himalaya arc, a convergent boundary between Indo-Australian and Eurasian plates. It was the largest seismic event along the Himalaya arc in the past 80 years, resulting in considerable human and economic losses. At present, the most active structure along the Himalaya range is the Main Frontal Thrust (MFT), the southernmost branch of the Main Himalaya Thrust (MHT) system, which absorbs about half of the total convergence rate of ∼40 mm/yr between India and Eurasia (*Lavé and Avouac*, 2000). GPS measurements made before the 2015 Gorkha earthquake suggest that the thrust is locked from its surface trace to ∼100 km to the north (*Ader et al.*, 2012). Inversions of seismic and geodetic data showed that the 2015 Gorkha rupture did not reach the surface, and that most of the moment release was concentrated in the deeper part of the seismogenic zone (between ∼50 and 100 km North of the MFT trace) (e.g. *Fan and Shearer*, 2015; *Lindsey et al.*, 2015; *Wang and Fialko*, 2015). How the shallow portion of the MFT responds to stress changes induced by the 2015 Gorkha earthquake is important for assessing the future seismic hazard along the central Himalaya arc (*Wang and Fialko*, 2015; *Mencin et al.*, 2016).

Previous models of the Gorkha event are mostly based on analytic or semi-analytic solutions for dislocations in a homogeneous or layered elastic half-space (e.g. *Lindsey et al.*, 2015; *Wang and Fialko*, 2015; *Elliott et al.*, 2016; *Whipple*

et al., 2016). The epicentral area of the 2015 Gorkha earthquake is characterized by strong variations in surface relief and material properties. The elevation above the sea level increases from a few hundred meters in the India plain to over ∼5 km in southern Tibet. Seismic topography studies reveal large changes in the crustal thickness and seismic velocities across the Himalaya range (e.g. *Monsalve et al.*, 2008; *Schulte-Pelkum et al.*, 2005). These lateral variations may introduce a bias in slip models based on assumptions of a homogeneous or layered elastic half-space. More sophisticated models are also warranted by detailed high-quality space geodetic observations of coseismic deformation due to the 2015 M_w 7.8 earthquake, including data from the ALOS-2 and Sentinel-1 Interferometric Synthetic Aperture Radar (InSAR) missions, as well as the continuous Global Positioning System (GPS) network in Nepal (*Ader et al.*, 2012; *Lindsey et al.*, 2015; *Wang and Fialko*, 2015; *Elliott et al.*, 2016).

Large earthquakes generate sudden stress changes in the ambient rocks that may activate a variety of time-dependent relaxation processes. Commonly considered models for postseismic deformation include visco-elastic relaxation in the lower crust and upper mantle, aseismic slip updip and/or downdip of the coseismic rupture, and poro-elastic rebound in the fluid-saturated upper crust. If contributions of various relaxation mechanisms to the observed postseismic deformation can be identified and evaluated, they may provide valuable constraints on in situ mechanical properties of the host rocks. In particular, measurements of postseismic deformation following the 2015 Gorkha earthquake may provide insights into

frictional properties of the MHT, effective viscosities of the lower crust and upper mantle beneath southern Tibet, and mechanisms of convergence and uplift in an active collision zone.

In this paper, we first refine the coseismic slip model of the 2015 Gorkha using Finite Element Models (FEM) that explicitly account for lateral variations in material properties and surface topography across the Himalaya range. We then present the GPS and InSAR observations of postseismic deformation over ~2 years after the Gorkha earthquake. We compare the observed postseismic deformation to models assuming various relaxation mechanisms (i.e. afterslip, visco-elastic relaxation and poro-elastic rebound) to explore what mechanism (or a combination of mechanisms) may have contributed to the early-stage postseismic deformation due to the 2015 Gorkha earthquake.

4.2 Coseismic slip models

4.2.1 Refinement of the coseismic slip model with FEM

To account for lateral variations in surface topography and material properties, we use Finite Element Models (FEM) to calculate surface displacements due to fault slip. FEM simulations are performed using Abaqus (*Abaqus/Simulia*, 2017). Slip on a fault is implemented using the split-node approach (e.g., *Melosh and Raefsky*, 1981) as follows (Figure 4.1): (1) The entire model domain is meshed in a way such that the two sides of the earthquake rupture have the same node

distributions. (2) An extra ("dummy") node is assigned to each node pair on a fault which shares the same coordinates. This dummy node does not belong to any finite element. (3) A linear constraint is defined for each node pair and the corresponding dummy node. (4) The nodes on both sides of the fault are then split by applying a displacement boundary condition along the direction of slip on a fault.

The fault geometry we adopted in our FEM simulations is based on one of the best-fitting solutions of *Wang and Fialko* (2015). The strike and dip angles of the fault are 285.4° and 7°, respectively. The depth of the fault plane at the surface trace of the MFT is 4 km. Similar fault geometries were suggested by a number of studies of the 2015 Gorkha earthquake (e.g. *Elliott et al.*, 2016; *Lindsey et al.*, 2015; *Whipple et al.*, 2016). The dimension of our finite element model is 1200 km × 1200 km × 400 km along strike, dip, and vertical directions, respectively. To better resolve the displacement and stress fields close to the fault rupture, the element size gradually decreases toward the fault (Figure 4.2). The fault plane was discretized into ∼3000 triangular elements which sizes gradually increase along the dip direction, with the smallest size of ∼3 km at the top edge of the fault plane. The model contains ∼1.1 million tetrahedron elements, with elements in the epicentral area as small as ∼1 km. We used the SRTM Digital Elevation Model (*Farr and Kobrick*, 2000) to incorporate topography into our finite element mesh. Vertical coordinates are referenced to the mean elevation south of the earthquake rupture (1.2 km above sea level). Unfortunately, no high-

resolution seismic tomography model is available for the study area. As the most significant variations in geophysical (e.g. crustal thickness and seismic velocities) and geomorphologic (e.g. surface elevation) features in the study region occur in the longtitudal direction, we adopted a 2-D velocity structure derived from the regional seismic topography (*Monsalve et al.*, 2008). Elastic moduli were calculated from P and S velocities assuming empirical relations between density and seismic velocities (*Brocher*, 2005). Below the depth of 70 km, material parameters are taken from the Preliminary Reference Earth Model (PREM). Figure 4.2b shows the assumed distribution of the Young's modulus along the profile perpendicular to the MFT from the India plain to the southern Tibet. Note that our FE model accounts for not only variations in elastic moduli with depth, but also for lateral variations in crustal thickness and material properties across the Himalaya range.

We evaluated the effects of lateral variations in the elastic properties and topography on surface deformation by comparing surface displacements predicted by FEM simulations with homogeneous elastic half-space models (*Wang and Fialko*, 2015). Results of this comparison are shown in Figure 4.3. Differences between the analytic solutions and numerical (FEM) solutions assuming no topography and spatially uniform elastic moduli are within 20 mm, or $\sim$1% for all three components of surface displacements (second row of panels in Figure 4.3). These differences characterize the accuracy of numerical models. The effect of surface topography on the calculated surface displacements is up to $\sim$50 mm, in case of a homogeneous medium (third row in Figure 4.3). When both the surface topography and

variations in material properties are included, the difference between the FEM and Okada's solutions is up to 0.2 m (>10%) for the vertical component of surface displacements (fourth row in Figure 4.3).

The Green functions calculated with FEM accounting for topography and spatial variations in material properties were used to invert for the coseismic slip distribution due to the 2015 Gorkha earthquake. We calculated the three components of surface displacements due to a unit slip along strike and dip directions on each node on a fault. Linear interpolation was used to calculate displacements at observation points that did not coincide with the mesh nodes at the surface. Surface displacement data and inversion parameters (relative weighting of different data sets, model smoothing, etc.) are the same as in *Wang and Fialko* (2015).

Figure 4.5 shows a comparison of coseismic slip models based on FEM solutions assuming (a) homogeneous elastic properties and flat surface, and (b) spatially variable elastic properties and surface topography (Figure 4.2). The two slip models are similar to each other, as well as to the dislocation model of *Wang and Fialko* (2015). The main difference is a somewhat larger slip amplitude in a model that accounts for topography and heterogeneity. The slip amplitude depends on the degree of smoothing applied in the inversions (a weaker smoothing yields a larger difference in slip amplitude). The two models shown in Figure 4.5 have similar posterior data fits, with the optimal value of smoothing determined by a trade-off between model roughness and data fit in each case. We find that for a wide range of smoothing parameters that yield reasonably good data fits, the model

that takes into account material heterogeneity and surface topography always has a moderately larger (∼10%) slip amplitude compared to the reference (homogeneous flat) model.

4.2.2 Coseismic slip model of the M_w 7.3 aftershock

The M_w 7.8 Gorkha earthquake was followed by a sequence of large ($M_w >$ 5) aftershocks. Most of these aftershocks occurred at the eastern end of the mainshock rupture, including the largest (M_w 7.3) aftershock of May 12th, 2015. The source parameters of the M_w 7.3 aftershock, including the hypocentral depth, fault attitude, etc, are not well constrained. The estimated hypocentral depth of the M_w7.3 aftershock is 15 km, almost twice as large as that of the mainshock (8.3 km), although the mainshock epicenter is further away from the MFT trace (Figure 4.6). Some studies suggested that the mainshock and the M_w 7.3 aftershock may have ruptured different faults (e.g. *Feng et al.*, 2016). Because the M_w 7.3 aftershock likely plays a role in driving postseismic relaxation, and might help constrain the subsurface geometry of the MHT fault system, we performed inversions of surface deformation data for the coseismic slip model of the M_w7.3 event.

The data used in the inversions include line-of-sight (LOS) displacements derived from ALOS-2 InSAR data from the ascending track A156 (strip-mode), and the descending track D048 (ScanSAR mode). We did not use the C-band data because of a poor phase correlation. The inversion procedure (data downsampling, calculation of Green functions, regularization, relative weighting between datasets

etc.) is the same as that used for the mainshock (*Wang and Fialko*, 2015). We performed two sets of inversions to explore the fault geometries admissible by the data. In the first test (hereafter referred to as "test A"), we required the fault plane to go through the seismically determined hypocenter, while the dip angle of the fault was allowed to vary. In the second test ("test B"), we allowed both the hypocenter depth and fault dip to vary. The fault strike was fixed at 285.4° in all tests. Figure 4.6a shows the spatial relationship of the M_w 7.3 aftershock with the mainshock. The aftershock occurred at the periphery of coseismic rupture, effectively extending the latter further to the East. Similar to the mainshock, the M_w 7.3 aftershock was dominated by thrust motion with a small amount of dextral slip. The maximum slip close to the epicenter is ∼4 m, smaller than the value of ∼6 m estimated by *Feng et al.* (2016), although the inferred maximum slip depends on the degree of smoothing. The total moment release from the aftershock is 8.1×10^{19} N m, assuming the shear modulus of 33 GPa. The corresponding moment magnitude is $M_w = 7.2$, in reasonable agreement with the seismically determined value. Tests A and B revealed a trade-off between the rupture depth and dip: a deeper rupture would imply a steeper dip. Figure 4.7 quantifies this trade-off, and Figure 4.8 shows the model fit to the data. Given that the seismologic estimate of the hypocenter depth is subject to significant uncertainties, geodetic constraints on the geometry of the aftershock rupture unfortunately do not allow one to distinguish between a planar fault (*Wang and Fialko*, 2015; *Whipple et al.*, 2016) and a ramp-and-flat structure (e.g. *Avouac*, 2007; *Elliott et al.*, 2016). In

any case, our results indicate that the M_w 7.3 aftershock likely occurred on the same fault as the mainshock. Because a shallowly dipping planar fault results in a slightly better fit to the data for both the M_w 7.8 mainshock and the M_w 7.3 aftershock, we use the respective geometry in all calculations below.

4.3 Postseismic deformation

4.3.1 GPS data

We used data from 32 continuous GPS (cGPS) sites within an area between 82-86 deg. E and 26-30 deg. N (Figure 4.9). We initially processed the raw GPS data using GAMIT/GLOBK (*Herring et al.*, 2015). We compared the position time series with solutions from the Nevada Geodetic Laboratory (NGL) and found the two solutions to be in good agreement. As the NGL solutions are routinely updated, we decided to use them in this study.

The NGL data products include time series of station coordinates in the reference frame IGS08, as well as estimates of position changes due to the reference frame, interseismic deformation, seasonal variations (e.g., due to hydrological loading), and the postseismic deformation following the 2015 Gorkha earthquake. To better resolve the contribution due to the postseismic deformation from other terms, we modeled the GPS position time series $x(t)$ before the 2015 Gorkha earth-

quake as:

$$x(t) = p_1 + p_2 t + \sum_{i=1}^{2}(p_{2i+1}\cos 2\pi\frac{t}{T/i} + p_{2i+2}\sin 2\pi\frac{t}{T/i}) \tag{4.1}$$

where p_1 denotes the initial position at a certain reference time, p_2 the secular velocity; $T = 1$ yr and $i = 1, 2$ corresponds to annual and semi-annual cycles (seasonal components), respectively. Some of the sites were deployed days to months after the 2015 Gorkha mainshock. For those sites, we used parameters p_1 to p_6 estimated from the nearest cGPS sites which have sufficiently long (>500 days) pre-earthquake recordings. We then subtracted the estimated secular and seasonal components (4.1) from the original time series to obtain time series $y(t)$ that mainly reflect postseismic deformation due to the 2015 Gorkha earthquake. Here, we assumed that the amplitude of seasonal signals does not change from year to year. Such an assumption was insufficient for some sites, as manifested by periodic variations in the residuals. We therefore visually checked time series $y(t)$ after correcting for secular and seasonal contributions. If any periodic variations were still apparent in the time series $y(t)$, we approximated the residuals as follows:

$$y(t) = q_1 + q_2 \log_{10}(1 + t/\tau) + \sum_{i=1}^{2}(q_{2i+1}\cos 2\pi\frac{t}{T/i} + q_{2i+2}\sin 2\pi\frac{t}{T/i}) \tag{4.2}$$

where τ is a constant characterizing how fast the postseismic transients decay with time. Estimation of τ is strongly affected by the early-epoch data. Depending on the dominant mechanism(s) involved in postseismic relaxation, τ could vary spatially (e.g., *Rousset et al.*, 2012). Unfortunately, most of the GPS sites with high signal-to-noise ratio (SNR) used in this study do not have recordings immediately

after the earthquake. We therefore assumed that the decay rate τ is uniform throughout the GPS network and estimated it using the north component of the displacement time series at site CHLM, which has the largest SNR and almost continuous recordings during the entire observation period following the mainshock. The estimated time constant $\tau = 27 \pm 5$ days was used to refine secular and seasonal components at other sites, assuming that the postseismic deformation signal decays logarithmically (eq. 4.2). To avoid spurious fitting, we only used sites with post-earthquake data spanning at least 300 days. We also corrected for offsets in the time series that might be due to equipment changes or local aftershocks.

Figure 4.9 shows the cumulative GPS displacements ∼700 days (from Apr. 26 2015 to Mar. 17 2017) after the 2015 Gorkha earthquake. Similar to the pattern of coseismic (*Wang and Fialko*, 2015) and early postseismic (*Mencin et al.*, 2016; *Gualandi et al.*, 2016) motion, most of the sites continued to move southward ∼2 years after the earthquake (Figure 4.9a). Displacements north of the rupture area are much larger compared to displacements south of the rupture. For instance, the north component of displacement at CHLM, a site just north of the mainshock rupture, reaches up to ∼90 mm during the observation period, whereas displacements at sites located updip of the coseismic rupture (e.g. NAST, DAMA, HETA, BTNI) are an order of magnitude smaller (<10 mm). Most of the sites experienced a relative uplift after the Gorkha earthquake, with the exception of site KKN4 that subsided at a rate greater than the estimated uncertainties (Figure 4.9b). Some sites within the Kathmandu basin, e.g. NAST, show rapid (>100 mm/yr) pre-

earthquake subsidence, most likely due to water extraction. Because data shown in Figure 4.9b represent changes with respect to the pre-seismic rates (where available), a relative uplift at NAST is a result of slowing down of subsidence after the earthquake.

4.3.2 InSAR data

The epicentral area of the 2015 Gorkha earthquake is well imaged by several SAR missions, in particular Sentinel-1A/B and ALOS-2. The L-band ALOS-2 data were instrumental for studies of coseismic deformation due to the Gorkha earthquake (e.g., *Lindsey et al.*, 2015; *Wang and Fialko*, 2015). The use of ALOS-2 data for measurements of postseismic deformation is somewhat limited because of large revisit times, changes of acquisition modes, and strong ionospheric artifacts. We therefore primarily relied on the Sentinel-1A/B data in this study, and used the ALOS-2 data to independently verify the results.

Because of the rugged topography, thick vegetation, and snow cover along the Himalaya front, the C-band Sentinel-1 data suffer from phase decorrelation. To mitigate the correlation problem, we analyzed the Sentinel-1 data using the Persistent Scatter (PS) approach (*Ferretti et al.*, 2001; *Hooper et al.*, 2004). We first geometrically aligned the images to a single master and generated the corresponding master-to-slave interferograms with GMT5SAR (*Sandwell et al.*, 2011; *Xu et al.*, 2017). No filtering was applied at the stage of making the interferograms. The selection of persistent scatterers was performed with StaMPS version 3.3 (*Hooper*

et al., 2007). Once the persistent scatters are identified, the interferometric phase at the respective pixels can be computed between any given acquisition dates by combining the original master-to-slave pairs. We verified this procedure by checking the phase residuals in closed circuits of interferograms. We found that the phase residuals in any closed circuit are generally on the order of 10^{-6} radians or less (Figure 4.10). This indicates good clock and orbital controls of the Sentinel-1 satellites. In total, we generated more than 200 interferograms for each of the three tracks covering the earthquake area (A085, D019 and D121). Interferograms were unwrapped individually to avoid a potential propagation of errors in the default "3D unwrapping" procedure in StaMPS.

One of the most significant limitations to InSAR measurements of a low-amplitude deformation is the variability of water vapor in the atmosphere. The resulting atmospheric phase delays may consist of a stratified and a turbulent component (e.g., *Ding et al.*, 2008; *Parker et al.*, 2015). The stratified component is expected to spatially correlate with topography and exhibit systematic temporal (e.g. seasonal) variations. The turbulent component, on the other hand, is expected to be essentially random both spatially and temporally. In our study area, the topography varies from a few hundreds meters in northern India to >5 km kilometers in southern Tibet (Figure 4.2). Such significant variations in surface elevation are expected to produce significant atmospheric phase delays across the Himalayan range. Indeed, many interferograms show a strong correlation between the radar phase and topography. We applied a correction for the elevation-dependent

humidity by performing a linear regression between the unwrapped radar phase and the digital elevation model. Data from the earthquake rupture area were excluded to prevent a possible contribution from surface deformation. We removed the best-fitting linear dependence of the radar phase on topography from each interferogram. Interferograms were also "flattened" by subtracting the best fitting plane to account for possible orbital errors.

We next applied a correction for the turbulent part of atmospheric delays using CANDIS (Code for Atmospheric Noise Depression through Iterative Stacking) (*Tymofyeyeva and Fialko*, 2015). The CANDIS algorithm exploits the fact that the radar phase of interferograms sharing a common acquisition contains the same contributions from atmospheric delays. The method applies if the deformation signal is linear or quasi-linear on a time scale that corresponds to a time span of an averaging stencil. An iterative procedure is used to improve estimates of atmospheric delays and deformation signals (*Tymofyeyeva and Fialko*, 2015).

The residual radar phase corrected for the atmospheric delays is used to obtain the line-of-sight (LOS) displacement histories using the Small Baseline Subset (SBAS) method (e.g., *Berardino et al.*, 2002; *Tong and Schmidt*, 2016). The initial rough estimate of the LOS displacement time series was obtained using a relatively strong smoothing in time. The estimated (quasi-linear) deformation signal was subtracted from the interferograms to update the atmospheric phase screens (APS). The updated APS were subtracted from the original interferograms, and the LOS displacement time series were recomputed with reduced temporal smoothing. The

amount of smoothing was gradually reduced in each subsequent iteration to allow recovery of non-linear signals. The iterations continued until convergence criteria were met.

Figure 4.11 shows the postseismic LOS displacements for ∼1.7 years after the earthquake from three Sentinel-1 tracks covering the earthquake area. The LOS displacements from all three tracks show a region of decreases in radar range (an uplift, if the horizontal motion is ignored) at the down-dip edge of the coseismic rupture. The maximum LOS displacements are up to ∼70 mm for both the ascending track A085 and the descending track D019 during the observation period. The LOS displacements from the descending track D121 are somewhat smaller, in part because of differences in the radar incidence angle: the deformation anomaly is in the far range of track D121, but in the near range of tracks A085 and D019. A shallower incidence angle for track D121 reduces sensitivity to vertical motion. The positive LOS displacement anomaly seen in Figure 4.11 is indeed indicative of uplift, as (i) the same pattern is observed in data from the ascending and descending tracks, and (ii) the GPS data show that horizontal displacements are mainly in the North-South direction (Figure 4.9a), which has only a small component in the satellite line of sight. The LOS displacements also reveal subsidence in the Kathmandu basin, likely due to water pumping in the city of Kathmandu. We used ALOS-2 data to independently verify results of our analysis of Sentinel-1 data. We computed average LOS velocities from several ALOS-2 interferograms from track D048 (Figure 4.12a). While the velocities are noisier because of a relatively small

number of radar acquisitions, the main features seen in Sentinel-1 data (Figure 4.11) are also present in the average LOS velocities derived from ALOS-2 data (Figure 4.12b).

Figure 4.13 shows the time series of LOS displacements derived from Sentinel-1 data in the regions of anomalous deformation: site A is in the area of positive LOS displacements, and site B is in the area of negative LOS displacements, close to the cGPS site NAST. Although a relatively strong smoothing was applied in the SBAS time series analysis, the LOS displacements at site A clearly show a decaying signal, consistent with what one would expect from a postseismic transient. Given that data from the three Sentinel-1 tracks used in this study were acquired on different dates, similarities in both spatial (Figure 4.11) and temporal (Figure 4.13) patterns of surface deformation suggest that the results are robust. We also performed a number of sensitivity tests in which only a subset of interferograms was used to compute the displacement time series. Results were similar to those shown in Figures 4.11 and Figure 4.13. Finally, a comparison of InSAR time series with cGPS data from site NAST shows a reasonable agreement (Figure 4.13b). The LOS velocities derived from the InSAR time series analysis are somewhat smaller than the GPS velocity; this may be due to averaging of the InSAR data over a finite area around the cGPS site.

4.4 Modeling of Postseismic Deformation

In this section we evaluate predictions of models of postseismic deformation due to various relaxation mechanisms, and compare them to InSAR and GPS data to investigate which mechanism (or a combination of mechanisms) may have contributed to the observed postseismic deformation over a period of ∼2 years following the 2015 Gorkha earthquake.

4.4.1 Viscoelastic relaxation

We compute surface displacements due to visco-elastic relaxation using the same finite element model that was used in the inversions for coseismic fault slip (Section 4.2.1). To validate the FEM results, we compared surface displacements predicted by the finite element model to semi-analytic solutions (*Wang et al.*, 2006), using the same coseismic slip model and rheologic structure. In particular, we assumed a 1-D layered structure with a 20 km thick elastic layer underlain by a visco-elastic half-space with the dynamic viscosity of 10^{18} Pas. Figures 4.14a and b show the surface displacements due to visco-elastic relaxation 500 days after the earthquake calculated using the two methods. The model predictions are in excellent agreement, indicating that our numerical model is sufficiently accurate. Both models show pronounced subsidence and northward motion (up to ∼0.4 m) in the epicentral area, opposite to the sense of the observed displacements (Figures 4.9 and 4.11).

To account for possible lateral variations in rheologic properties across the Himalaya front (e.g., *Royden et al.*, 1997; *Clark and Royden*, 2000; *Huang et al.*, 2014), we considered a suite of models in which the lower crust beneath the Tibetan Plateau includes a layer with reduced viscosity (Figure 4.15). In these models, we assumed that the entire 50 km thick crust of the Indian plate is elastic and that the upper mantle below both India and southern Tibet is visco-elastic with the dynamic viscosity of 10^{20} Pa s. We considered a range of viscosities of the lower crust of southern Tibet η_T, as well as distances from the MFT trace, L_T, at which the transition to viscosity η_T occurs.

Figure 4.16 shows the predicted surface displacements due to visco-elastic relaxation for a laterally heterogeneous rheologic structure with $L_T = 120$ km and $\eta_T = 10^{18}$ Pas. Similar to a model that assumes a 1-D layered rheologic structure (Figure 4.14), the heterogeneous model also predicts northward motion and subsidence in the epicentral area, opposite to the observed pattern. The predicted InSAR range changes (Figure 4.17) are also opposite to the observed range changes (Figure 4.11). The modeled northward displacements at some of the GPS sites are up to ∼50 mm 2 years after the event. The surface displacements in case of the laterally heterogeneous model are generally smaller than those predicted by the 1-D layered model. This is because in the heterogeneous model, the region that undergoes relaxation is further away from the earthquake rupture. The amplitude of surface displacements decreases for a larger L_T. All results below correspond to $L_T = 120$ km (the distance from the MFT trace beyond which the Tibetan Plateau

reaches its average elevation of more than 4 km above the sea level, Figure 4.15).

Other variables explored in our forward models include different thicknesses and depths of the low viscosity layer beneath southern Tibet, and different viscosity contrasts across the Himalaya range. None of the tested models produced a sense of motion consistent with the GPS and InSAR observations. We therefore conclude that visco-elastic relaxation was not the dominant mechanism of post-seismic deformation in the first ∼2 years following the Gorkha earthquake, at least in the near-to-intermediate field (within ∼150 km from the earthquake rupture). Models including a low viscosity layer in the lower crust beneath Tibet do predict southward motion in the far field, in particular north of the 29 deg. N latitude (Figure 4.16). Measurements of the surface deformation over a broader area may provide further constraints on the effective rheology of the lower crust and upper mantle beneath the southern Tibet.

4.4.2 Poroelastic Rebound

We evaluated potential contributions due to poro-elastic rebound by differencing models of coseismic displacements under drained and undrained conditions. We assumed that the poro-elastic rebound is confined to the top 20 km of the crust, and the drained and undrained values of the Poisson's ratio of 0.25 and 0.28, respectively. The coseismic slip model of *Wang and Fialko* (2015) was used in this calculation. Figure 4.18 shows the predicted surface displacements due to the poro-elastic rebound. Overall, the poro-elastic rebound model does predict the

southward motion and uplift south of the downdip edge of the coseismic rupture, qualitatively consistent with the GPS and InSAR measurements. However, the displacements predicted by the poro-elastic rebound are much smaller (<10 mm) than the observed displacements. Increasing the difference between the drained and undrained values of the Poisson's ratio can amplify the displacement magnitude, but less than by a factor of two for reasonable values of poro-elastic material parameters. Smaller assumed values of the thickness of the fluid saturated layer would decrease the magnitude of predicted surface displacements. We conclude that while the poro-elastic rebound may have contributed to the observed deformation transient, its contribution is relatively small. Similar conclusions were reached in several previous studies of large shallow earthquakes (e.g., *Barbot et al.*, 2008; *Gonzalez-Ortega et al.*, 2014).

4.4.3 Afterslip

Kinematic Inversions

An overall similarity between patterns of coseismic and postseismic displacements (southward motion and uplift) documented by space geodetic observations is suggestive of a continued slip on a fault that produced the earthquake. To get an insight into the spatial distribution of afterslip, we performed kinematic inversions of the observed surface displacements. We assumed that afterslip occurred on the same fault plane as the coseismic rupture. We used the fault geometry based on

the coseismic slip model of *Wang and Fialko* (2015), extended both in strike and dip directions. We assumed that the fault has a dip angle of 7° and the depth of the fault plane at the surface trace of the MFT is 4 km. We calculated the Green functions using analytic solutions for a dislocation in a homogeneous elastic half-space (*Okada*, 1985).

Both the GPS and InSAR data were used in the inversions. For the GPS data, we used the horizontal components of the cumulative displacements as shown in Figure 4.9a. InSAR observations were made over somewhat different time periods. To ensure consistency between the two data sets, we scaled the LOS displacements shown in Figure 4.11 by a factor F that accounts for the InSAR time span for each track, assuming that the LOS displacement histories follow the same logarithmic function (time constant τ of 27 days) that best fits the GPS timeseries,

$$F = \frac{\log(1 + t_{gps}/\tau)}{\log(1 + t_2/\tau) - \log(1 + t_1/\tau)}, \tag{4.3}$$

where t_{gps} is the duration of the GPS time series (starting immediately after the earthquake), and t_1 and t_2 are the start and the end times of the respective InSAR timeseries.

The InSAR data were downsampled iteratively during the inversion using the current best-fitting model to avoid oversampling in areas with large phase gradients due to noise (atmospheric perturbations, unwrapping errors, etc.) (*Wang and Fialko*, 2015). To investigate the model sensitivity to different data sets, we inverted the GPS and InSAR data separately, as well as jointly. Figure 4.19 shows

the best-fitting afterslip models derived from the GPS data only, as well as from the joint inversion. In both cases afterslip is found to occur downdip of (and next to) the coseismic rupture. The cumulative afterslip ∼700 days after the mainshock is in excess of ∼0.3 m. Compared to the afterslip model derived using the GPS data alone, the joint GPS/InSAR inversion suggest a more compact slip distribution. Also, the maximum slip in the joint inverse model is closer to the downdip edge of the coseismic rupture, suggesting that addition of InSAR data does improve the model resolution. The preferred model fits the data reasonably well (Figure 4.20).

Stress-driven afterslip

Kinematic inversions indicate that the observed postseismic deformation ∼2 years following the 2015 Gorkha earthquake can be well explained by an afterslip model with most of the slip occurring at the downdip end of the coseismic rupture. To verify whether the slip amplitude and distribution are consistent with relaxation of coseismic stress changes on a fault plane, we performed a suite of numerical simulations assuming that the evolution of afterslip is governed by the rate and state friction. Simulations were performed using the Fourier-domain fictitious body force code RELAX (*Barbot and Fialko*, 2010). Afterslip was only allowed in areas on a fault that experienced a coseismic increase in the Coulomb stress. The geometry of the fault was the same as the one used in kinematic inversions. Assuming quasi-steady creep, the slip rate on the velocity-strengthening part of

the fault can be expressed as (*Barbot et al.*, 2009):

$$v = 2v_0 \sinh \frac{\Delta\tau}{a\sigma} \tag{4.4}$$

where v_0 is a reference slip rate, $\Delta\tau$ is the coseismic shear stress change, a is the rate and state friction parameter characterizing the direct effect (*Dieterich*, 1979), and σ is the effective normal stress on a fault.

Stress-driven afterslip models that allowed for creep on a shallow part of the MFT updip of the 2015 rupture produced large horizontal displacements south of the epicenter, which are not observed by the cGPS network. This indicates that the shallow part of the MFT is locked, and will release coseismic stress increases due to the Gorkha event in future earthquakes. Thus we allowed for the velocity-strengthening behavior on a fault plane only below the 2015 rupture. The transition from velocity-weakening to velocity-strengthening behavior is parameterized in our model by the distance from the surface trace of the MFT, y_0. We performed forward simulations over a wide range of model parameters, including v_0, $a\sigma$ (see eq. 4.4), and y_0. Optimal values of these parameters that rendered the best agreement between the model predictions and the GPS data are: $y_0 = 110$ km, $v_0 = 3.2 \times 10^{-7}$ m/s, and $a\sigma = 6.5$ MPa. The respective results are shown in Figure 4.21. Assuming an effective normal stress of $\sigma = 100$ MPa, this yields an estimate of $a = 6.5 \times 10^{-2}$, which is on the order of typical values of the rate dependence parameter $(a - b) \simeq 10^{-3} - 10^{-2}$ suggested by laboratory experiments (*Marone*, 1998; *Mitchell et al.*, 2016). There is a relatively poor agreement between

the data and the model predictions between the eastern tip of the 2015 rupture and the M_w7.3 aftershock (e.g. at the cGPS sites JIR2 and XBAR). While the model shown in Figure 4.21 is not a result of a formal inversion, a local misfit may be indicative of the along-strike variations in the fault geometry or frictional properties (in particular, the depth of transition from velocity-weakening to velocity strengthening friction), or some combination of both. Overall, a good qualitative agreement between the model predictions and geodetic observations suggests that the near-field postseismic deformation during ∼2 yrs after the mainshock was dominated by afterslip on the downdip extension of the coseismic rupture, in response to the stress changes imparted by the 2015 earthquake and its large aftershocks.

4.5 Discussion

Rheologic properties of the lower crust and upper mantle in an active collision zone such as Tibet are of considerable interest as they bear on a number of tectonic and geodynamic problems. There is a long-standing debate about the mechanisms responsible for uplift and topographic variations in continental orogens. In particular, a weak lower crust was proposed to explain the uplift of wide plateaus in the absence of significant internal shortening (*Zhao and Morgan*, 1987; *Burov and Watts*, 2006; *Royden et al.*, 1997). *Clark and Royden* (2000) suggested that the lateral extrusion of the low-viscosity lower crust is responsible for the outward growth of the Tibetan Plateau, and that topographic variations across

the plateau margins can be explained by a viscous pressure drop within the lower crustal channel of constant thickness. According to this model, gentle topographic slopes (such as those in the North-East and South-East margins of Tibet) are associated with a relatively low viscosity of channel material in foreland (10^{18} Pa s), while steep slopes (such as those in Nepal) are due to high viscosity of channel material in foreland (10^{21} Pa s). The model implicitly assumes very low viscosities in the lower crust beneath much of the Tibetan Plateau ($10^{16} - 10^{17}$ Pa s) to prevent viscous pressure losses (and the associated elevation changes) in the plateau proper. Results presented in this study indicate that the lower crustal viscosity cannot be low either in the foreland or in the adjacent plateau. In the context of the channel flow model (*Royden et al.*, 1997; *Clark and Royden*, 2000), the observed postseismic deformation due to the 2015 Gorkha earthquake does not provide useful constraints on the viscosity of the lower crustal material in the foreland, given that the time span of observations is short compared to the expected relaxation time. However, our results do rule out low ($< 10^{18}$ Pa s) viscosities beneath the Tibetan Plateau. Specifically, InSAR LOS and GPS displacements $\sim$2 years after the mainshock show overall southward and upward motion, while the visco-elastic relaxation models predict northward and downward motion in the epicentral area, regardless of the rheologic structure assumed in the model. For the effective viscosity of 10^{18} Pas in the lower crust 120 km north of the MFT, the northward displacements predicted by the visco-elastic relaxation models are up to $\sim$4 cm during the observation period (Figure 4.16). The discrepancy be-

tween the observations and model predictions would be larger if any visco-elastic relaxation occurred in the foreland (see Figure 4.14). The amplitude of surface displacements due to visco-elastic relaxation could be reduced by assuming that a transition from strong to weak lower crust occurs further to the North (larger L_T, Figure 4.15). However, this would be inconsistent with the assumption that the topographic slopes are controlled by the viscosity of material in the underlying lower crust (*Royden et al.*, 1997; *Clark and Royden*, 2000). Our models assume a simple linear Maxwell rheology. However, note that the predicted spatial patterns of surface displacements would be similar in case of more complex (e.g., the Burgers or the power-law) rheologies (*Barbot and Fialko*, 2010; *Takeuchi and Fialko*, 2012, 2013; *Huang et al.*, 2014).

As surface displacements due to visco-elastic relaxation and afterslip have opposite signs in the near field of the Gorkha earthquake rupture, an important question is whether some visco-elastic relaxation could be overprinted in the presence of afterslip. To constrain an admissible range of the effective viscosities η_T of the lower crust of southern Tibet, we subtracted the displacements predicted by the preferred stress-driven afterslip model (section 4.3.2) in the limit of full relaxation from the GPS observations, and compared the residual displacements to results of forward models of visco-elastic relaxation. Figure 4.22 shows the misfit of visco-elastic models for different values of η_T. The difference between the residual displacements and model predictions is minimized for the effective viscosities of the lower crust beneath southern Tibet of $\eta_T > 5 \times 10^{18}$ Pa s. This estimate

is based only on the amplitude of horizontal displacements, and does not imply that a non-negligible contribution of visco-elastic relaxation in the near field of the 2015 Gorkha event is required by the data. The lower bound on the viscosity might be reduced if one assumes a shallower transition from the velocity-weakening to velocity-strengthening friction (Figure 4.21a), which will increase the amplitude of afterslip (thereby allowing for a larger visco-elastic contribution). However, we note that models assuming a low-viscosity lower crust beneath high Tibet predict substantial southward movement and uplift on the Tibet side (e.g. north of 28.5°N latitude, see Figure 4.16). No evidence for such deformation is apparent in the InSAR data (Figure 4.11). Observations over longer time periods and broader areas will further refine constraints on the rheologic structure and effective properties of the Tibetan lithosphere.

It may be instructive to compare observations and models of postseismic deformation due to the Gorkha earthquake to studies of other large events that occurred in a similar setting. *Huang et al.* (2014) used InSAR and GPS observations spanning a comparable period (< 2 years) after the 2008 Wenchuan (China) earthquake that occurred at the eastern margin of the Tibetan Plateau. They concluded that the data are best explained in terms of visco-elastic relaxation in the lower crust (with the inferred transient viscosity of $\sim 10^{18}$ Pa s) and upper mantle beneath Tibet; afterslip was argued to be an unlikely mechanism because the best-fitting kinematic models required slip at an unreasonably large depth. Because of the challenging surface conditions, the analysis of *Huang et al.* (2014)

however was based on a rather limited InSAR data set. *Wang and Fialko* (2014) considered postseismic deformation that occurred over ∼5 years after the 2005 M_w7.6 Kashmir (Pakistan) at the Western end of the Himalayan Arc. They found that the near-field deformation was dominated by afterslip on a downdip extension of the earthquake rupture, possibly with a minor contribution from a poro-elastic rebound, similar to the results of this study. The lower bound on the effective viscosity of the ductile substrate in the northwestern Himalaya estimated by *Wang and Fialko* (2014) was 10^{19} Pa s, although their model did not consider possible lateral variations in the rheologic structure. Similar values of the effective viscosity were also reported in studies of postseismic transients of large events in central Tibet (e.g., *Ryder et al.*, 2011, 2014). The effective viscosities in the interior of the Tibetan Plateau constrained by geodetic observations of postseismic transients are thus much higher than the values implied by fluid-mechanical models of topography variations across the plateau margins (e.g., *Royden et al.*, 1997; *Clark and Royden*, 2000).

Our results indicate that the near-field postseismic deformation over ∼2 years following the 2015 Gorkha earthquake is best explained by afterslip on the MFT with most of the slip concentrated at the downdip end of the coseismic rupture. Little or no afterslip is found on the shallow part of the fault, which experienced a coseismic increase in the shear stress of the order of megapascals. The lack of shallow creep indicates velocity-weakening (i.e., seismogenic) behavior of the shallow section of the MFT. This is consistent with models of interseismic

deformation that indicate that the MFT is locked all the way from the surface to the seismic/aseismic transition ∼100 km to the North of the fault trace (e.g., *Ader et al.*, 2012). Recent numerical models informed by geologic observations suggest that partial ruptures of the MFT can result from a complex fault geometry (*Qiu et al.*, 2016). Loading from the 2015 Gorkha event, and the accelerated postseismic creep at the bottom of the seismogenic zone (Figure 4.21a) are bringing the shallow section of the MFT closer to failure.

4.6 Conclusions

The 2015 M_w7.8 Gorkha (Nepal) earthquake occurred along the central Himalaya arc. The epicentral area of the earthquake is characterized by substantial variations in surface elevation and crustal properties. We constructed finite element models to explicitly account for the surface topography and lateral variations in material properties to refine the coseismic slip model of the 2015 Gorkha earthquake, and interpret the observed postseismic deformation. Forward models show that surface topography has a relatively minor effect on surface deformation and therefore on results of inverse models. Compared to slip inversions assuming a homogeneous elastic half-space, inversions that use Green functions computed using finite element models that account for both topography and material variations across the Himalaya produce ∼10% more slip at the depth of seismic asperities. Finite fault inversions of the ALOS-2 InSAR observations of the M_w7.3 (May 12,

2015) aftershock suggest that the latter likely occurred on the same fault as the mainshock. Neither the mainshock nor the aftershock models allow one to distinguish between a planar and a ramp-and-flat fault geometry, although a planar geometry gives rise to a slightly better fit to the data. Postseismic deformation over ∼2 years after the 2015 Gorkha earthquake is characterized by the southward and upward surface motion in the epicentral area. This pattern is opposite to predictions of visco-elastic relaxation models, but is well explained by models of afterslip at the downdip end of the earthquake rupture. The maximum afterslip exceeds 0.3 m over the observation period. The lack of slip on a shallow portion of the MFT during and after the 2015 Gorkha earthquake implies continued seismic hazard in the Kathmandu area. The observed postseismic deformation is inconsistent with models assuming low ($< 10^{18}$ Pa s) effective viscosity in the lower crust beneath the Tibetan Plateau.

Acknowledgement

This work was supported by NSF (grant EAR-1547516) and NASA (grant NNX14AQ15G). GPS data used in this study are from a network designed and installed by J.-P. Avouac and colleagues. Raw GPS RINEX files are provided by UNAVCO. Time series of the station positions are provided by Nevada Geodetic Laboratory. Sentinel-1 data are provided by the European Space Agency (ESA) through Alaska Satellite Facility (ASF) and UNAVCO. ALOS-2 data are courtesy

of the Japanese Space Agency (JAXA). SAR data processing was performed on the Comet cluster at the San Diego Supercomputing Center (SDSC). Data and modeling results used in this study are available from the authors.

This chapter, in full, is a preprint of the material being submitted to *JGR*, which may appear as: Wang, K., and Y. Fialko, "Observations and modeling of co- and post-seismic deformation due to the 2015 Mw 7.8 Gorkha (Nepal) earthquake", *Journal of Geophysical Research: Solid Earth*. The author of this dissertation is the primary investigator of work presented in this chapter.

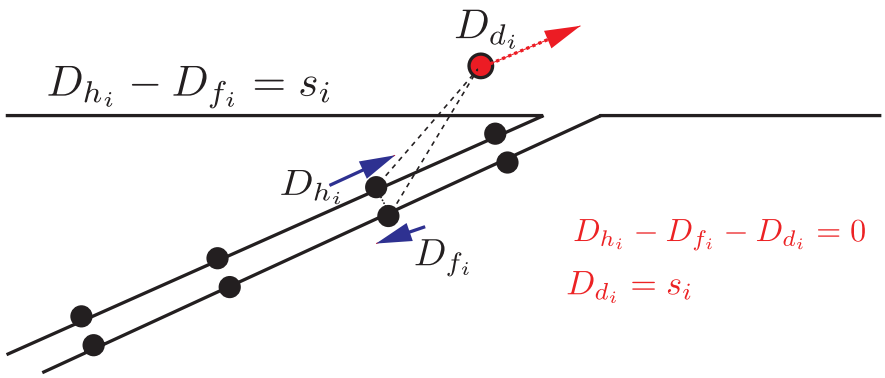

Figure 4.1: A diagram illustrating the "split node" technique in FEM. A dummy node d_i is tied to each node pair h_i – f_i on fault by forming a linear equation $D_{h_i} - D_{f_i} = s_i$, where D are displacements, and s_i is the slip vector. The node pair on a fault is split by applying a boundary condition $D_{d_i} = s_i$ to the dummy node associated with the node pair.

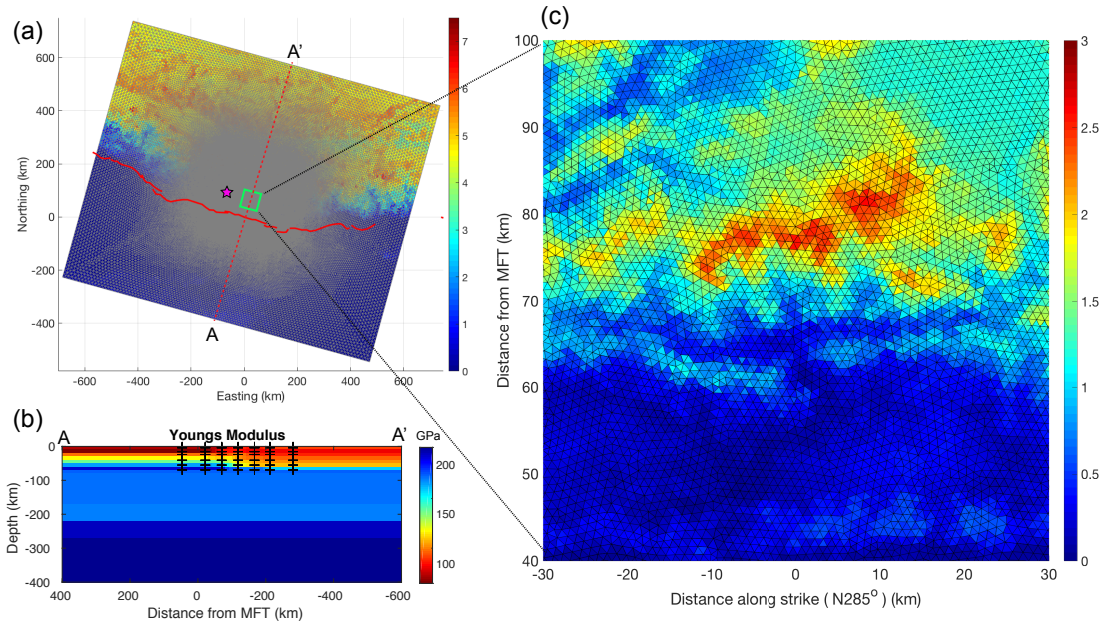

Figure 4.2: FEM mesh and elastic structure used in numerical simulations. (a) Top-view of the model mesh. The mesh size gradually decreases toward the earthquake rupture. The red curve denotes the MFT trace. The magenta star denotes the epicenter of the 2015 M_w7.8 Gorkha earthquake. (b) The Young's modulus variations along a profile normal to the MFT. The black crosses denote centers of resolution cells in the seismic tomography model of *Monsalve et al.* (2008). (c) Zoom-in of the FEM mesh in an area near the 2015 rupture (green box in panel (a)).

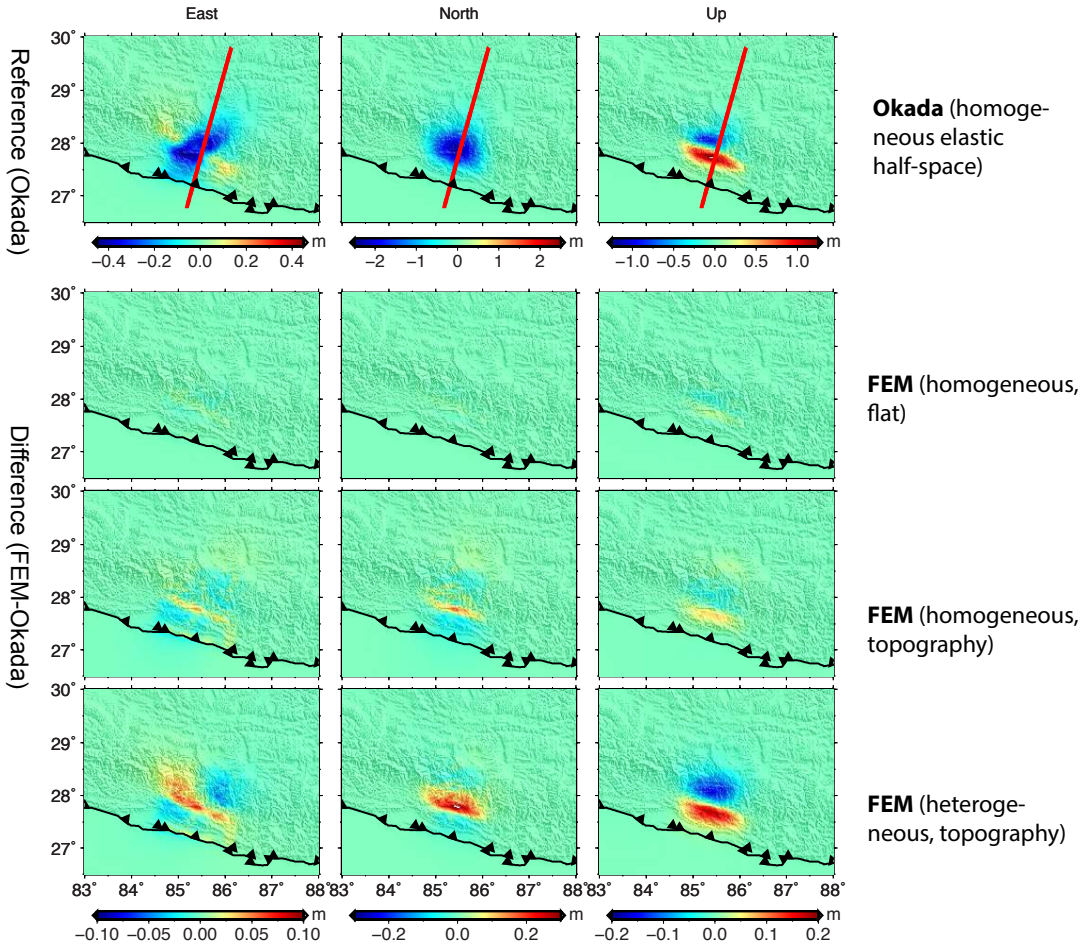

Figure 4.3: Forward calculations of coseismic surface displacements due to the 2015 M_w7.8 Gorkha earthquake. The coseismic slip model is from *Wang and Fialko* (2015). The elastic structure is from the seismic tomography model (*Monsalve et al.*, 2008). The bottom three rows represent differences in surface displacements between homogeneous half-space and FEM models. Surface displacements along a profile denoted by a red line are shown in Figure 4.4.

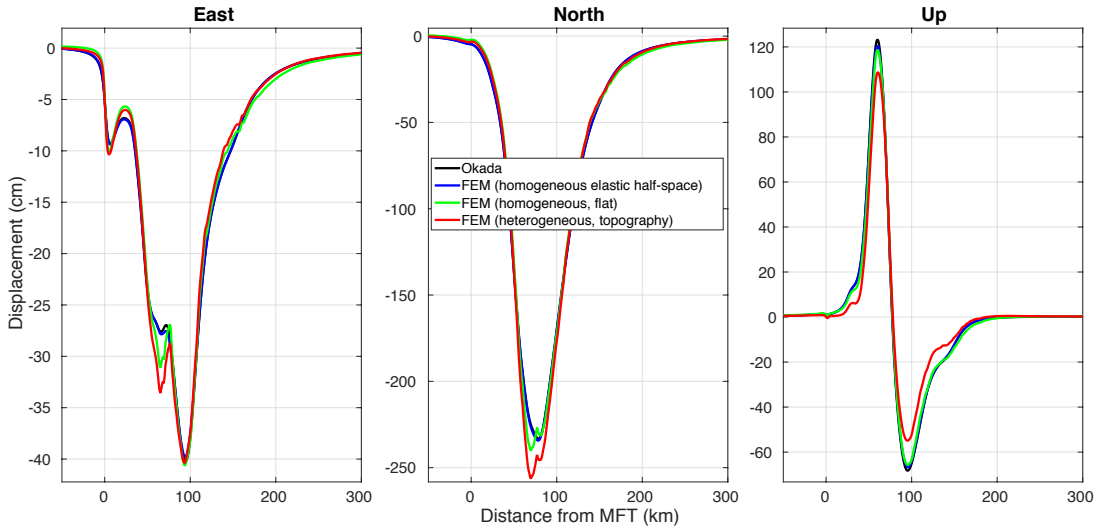

Figure 4.4: Predicted surface displacements along a profile perpendicular to the MFT (red line in Figure 4.3) due to the 2015 Gorkha for models with and without surface topography and/or variations in material properties

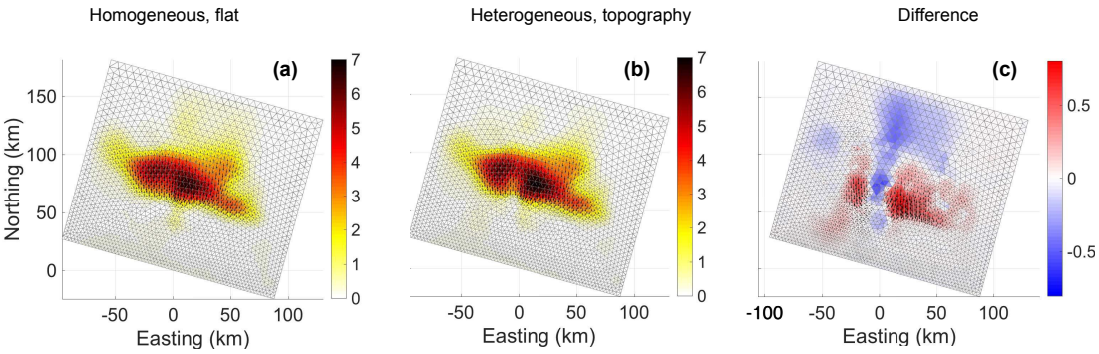

Figure 4.5: Comparison of coseismic slip models from inversions using FEM Green's functions assuming: (a) homogeneous elastic medium with no surface topography; (b) heterogeneous elastic structure from seismic tomography, with surface topography; (c) the difference between (a) and (b).

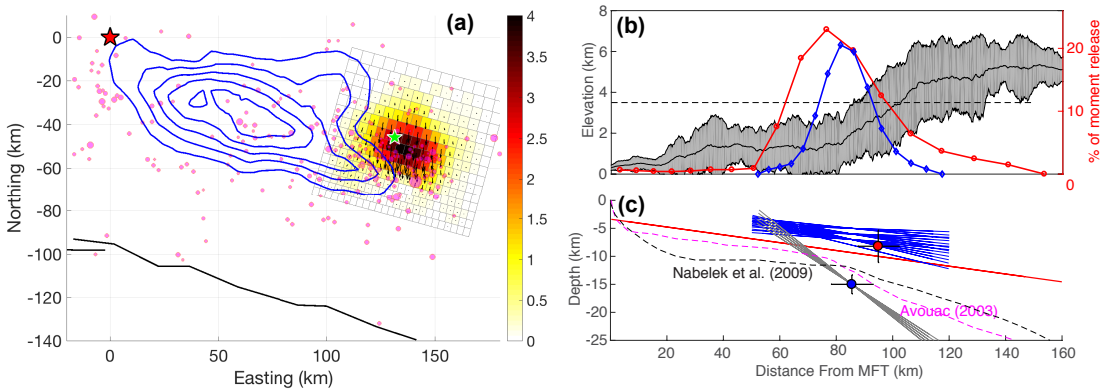

Figure 4.6: Coseismic slip model of the M_w7.3 aftershock of May 12, 2015. (a) Map view illustrating spatial relationships between the mainshock and the M_w7.3 aftershock. Blue contours represent coseismic slip due to the mainshock (1 m increments, starting from 1 m). Red and green stars denote the epicenters of the mainshock and the M_w7.3 aftershock, respectively. Black line represents the surface trace of the MFT. (b) Moment release of the mainshock (red) and aftershock (blue), and surface topography (shaded grey) in the direction normal to the mean strike of the MFT (N285.4°) in the study area. (c) Cross-section view showing geometries of the best-fitting fault models. Red line denotes the preferred mainshock solution of *Wang and Fialko* (2015). Gray and blue lines denote admissible solutions for the aftershock (tests A and B, see the main text). Red and blue circles with error bars denote the USGS-determined hypocenters of the mainshock and the M_w7.3 aftershock, respectively. The dashed magenta and black lines denote the geometries of the MHT inferred by *Avouac* (2003) and *Nábělek et al.* (2009), respectively.

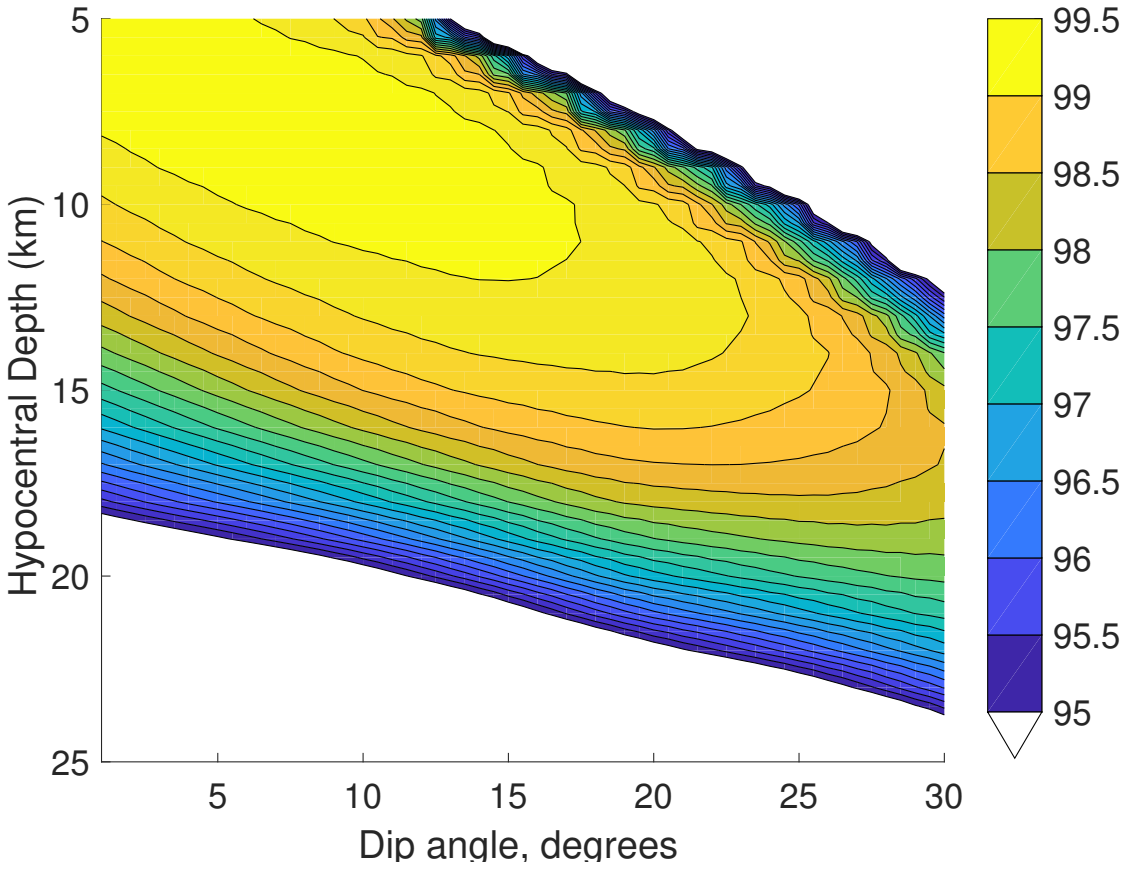

Figure 4.7: Percentage of variance reduction of the ALOS-2 data as a function of the hypocentral depth and the dip angle of the rupture plane of the Mw 7.3 aftershock. Note a trade-off between the hypocentral depth and the dip angle.

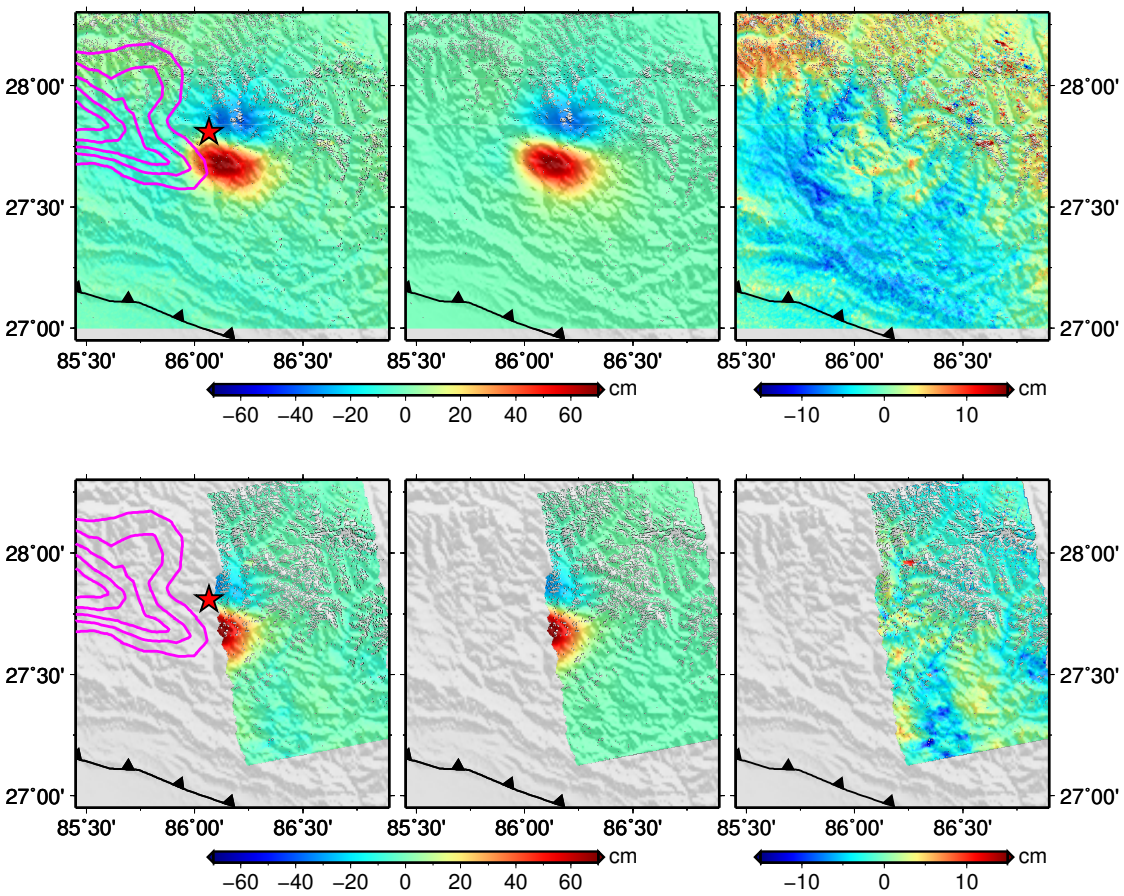

Figure 4.8: Comparison of the observed and modeled LOS displacements due to the Mw 7.3 aftershock on 05/12/2015 from two ALOS-2 tracks. Panels in the top row correspond to the descending track D048 (2015/05/03-2015/05/17), and panels in the bottom row correspond to the ascending track A156 (2015/04/27-2015/05/25). Red star represents the aftershock epicenter. Magenta contours denote the coseismic slip due to the mainshock.

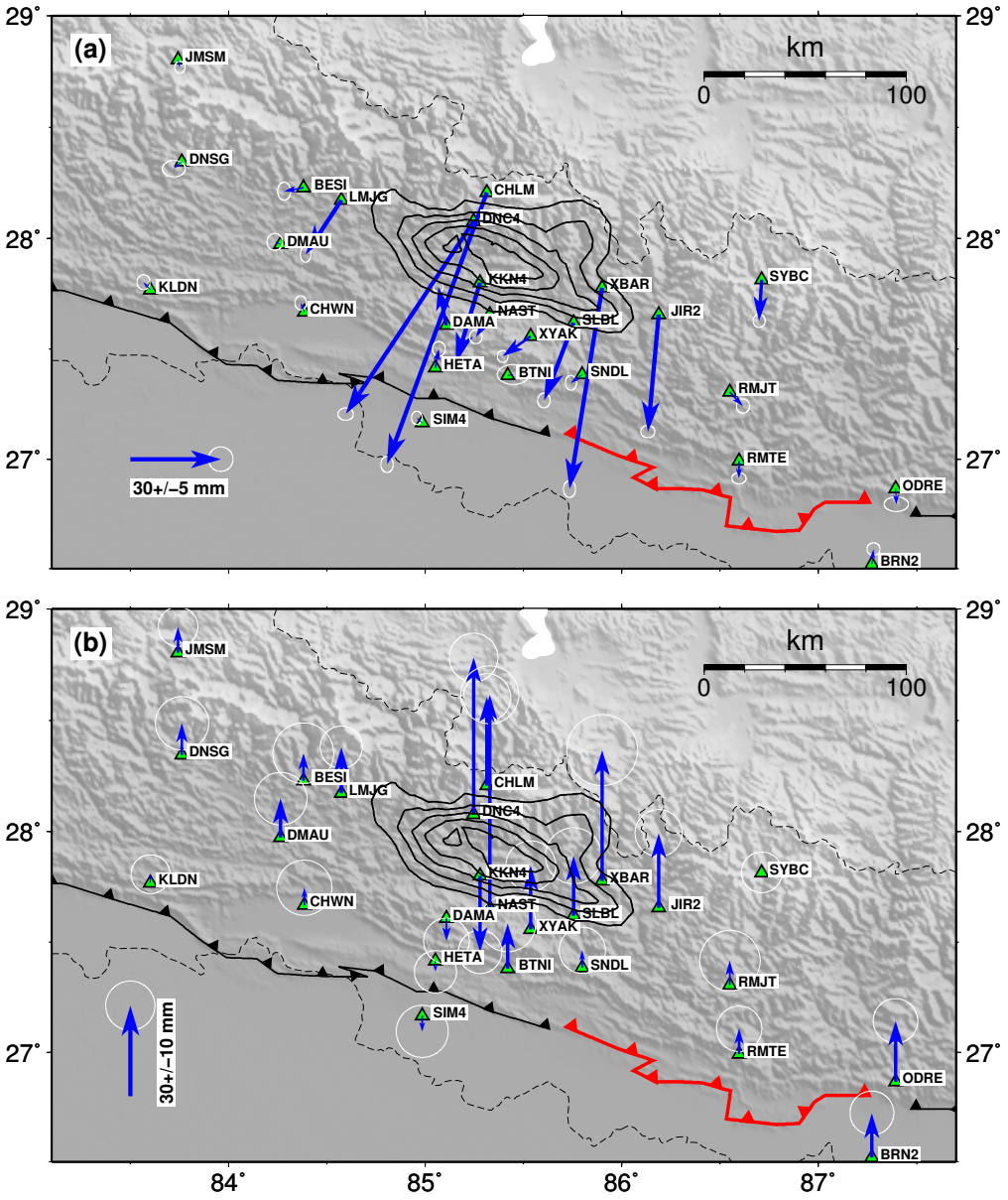

Figure 4.9: Cumulative postseismic GPS displacements due to the 2015 Gorkha earthquake ∼2 years after the mainshock: (a) horizontal component; (b) vertical component. The error ellipses represent the standard deviation of difference between the observed time series and the logarithmic function (eq. 4.2) after correcting for the secular and seasonal variations. The black contours represent the coseismic slip at 1 m increments starting from 1 m. Lines with triangles represents the Main Frontal Thrust (MFT) in the study area. The section that was possibly ruptured during the 1933 Nepal-Bihar earthquake is marked in red. Only sites with post-earthquake recordings spanning more than 300 days are shown.

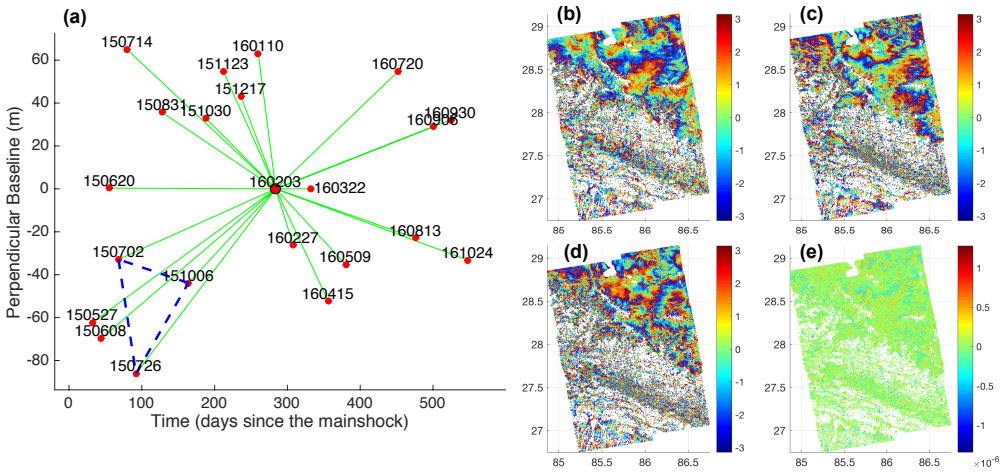

Figure 4.10: Phase closure test of Sentinel-1A data. (a) Baseline distribution of acquisitions from the ascending track A085. Labels denote the acquisition dates (yymmdd). Green lines represent the master-slave interferograms used to select the persistent scatters. (b), (c), (d) interferograms denoted by dashed blue lines in panel (a). (e) the sum of the interferograms (b), (c), and (d) forming a closed loop.

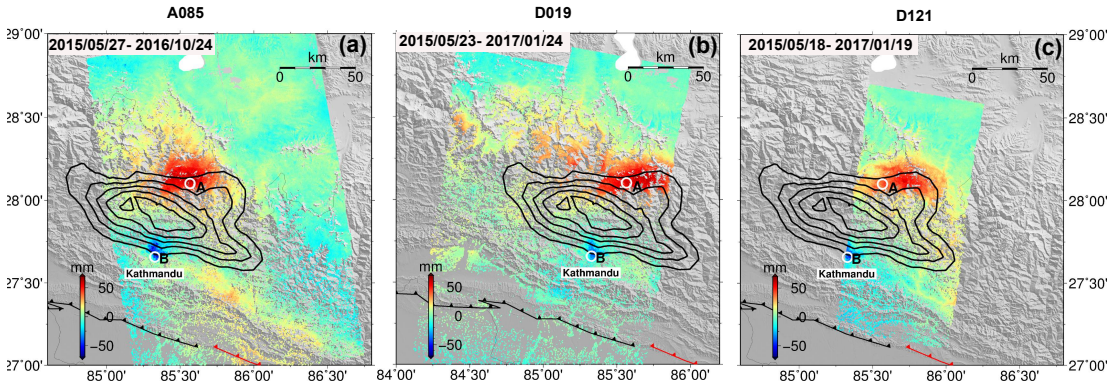

Figure 4.11: Postseismic LOS displacements from Sentinel-1 (a) ascending track A085, (b) descending track D019, and (c) descending track D121. Positive LOS displacements correspond to surface motion toward the satellite. Observation periods for each track are indicated in the top-left corner of each panel. The time series of the LOS displacements at locations A and B indicated by white circles are shown in Figure 4.13.

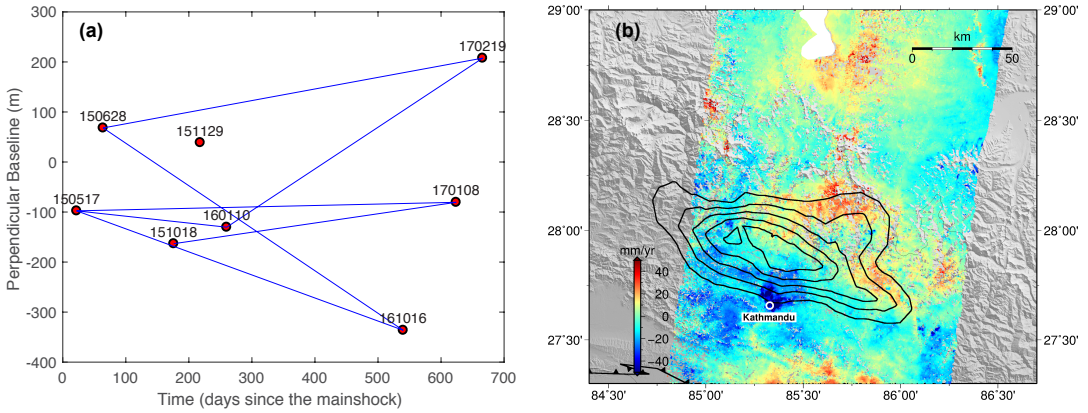

Figure 4.12: ALOS-2 data spanning the postseismic period from the descending track D048 (ScanSAR mode). (a) baseline vs time plot. Labels denote the acquisition dates (yymmdd). Blue lines represent interferograms used to calculate the mean line-of-sight velocities shown in panel (b). We only used data from the 3rd and 4th sub-swathes that cover the earthquake area. Interferograms were corrected fro long-wavelength artifacts (e.g. due to ionospheric perturbations and/or orbital errors) by removing the best-fitting plane from the unwrapped radar phase. (b) Mean LOS velocities correspond to the ground motion toward the satellites.

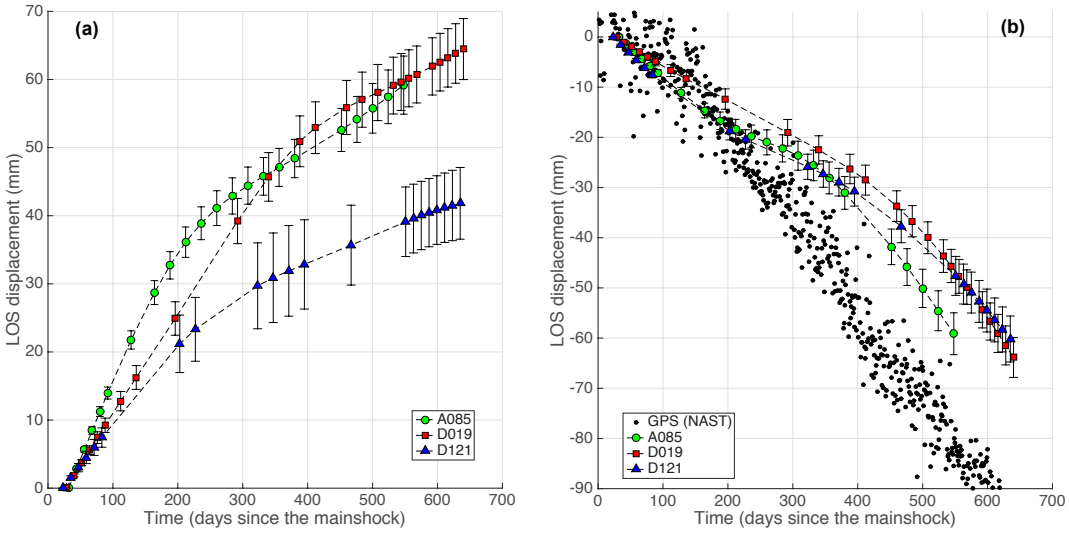

Figure 4.13: LOS displacement time series at (a) site A in the area of positive LOS displacements at the downdip end of the coseismic rupture; (b) site B in the area of negative LOS displacements near the cGPS site NAST (Kathmandu basin). The error bars represent the standard deviation of the LOS displacements for persistent scatters (PS) within a circle of 500 m radius. The GPS displacements are projected on the LOS of the ascending track A085.

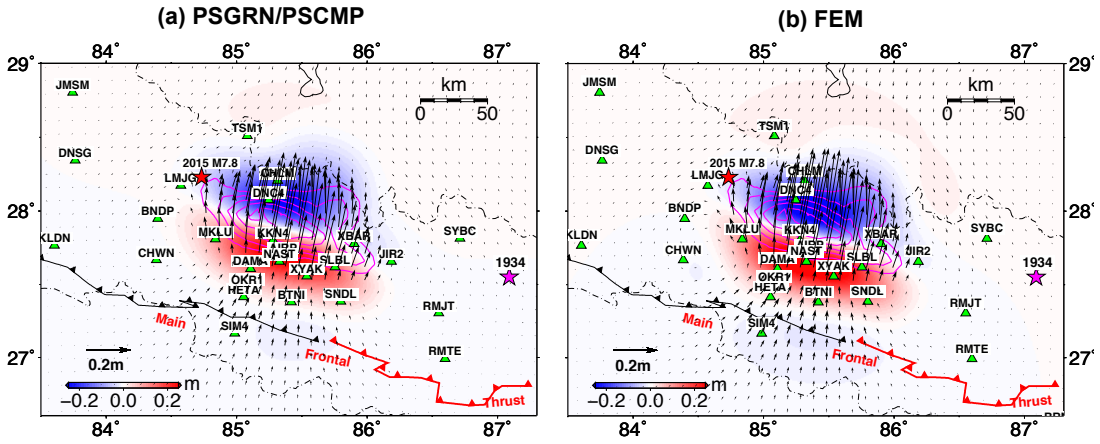

Figure 4.14: Predicted surface displacements due to visco-elastic relaxation 500 days after the 2015 Gorkha earthquake, assuming a 20 km thick elastic upper crust, and visco-elastic lower crust and upper mantle with the dynamic viscosity of 10^{18} Pa s. Results obtained using (a) PSGRN/PSCMP (*Wang et al.*, 2006), and (b) FEM simulations. Color represents the vertical motion. Green triangles denote the GPS stations used in this study.

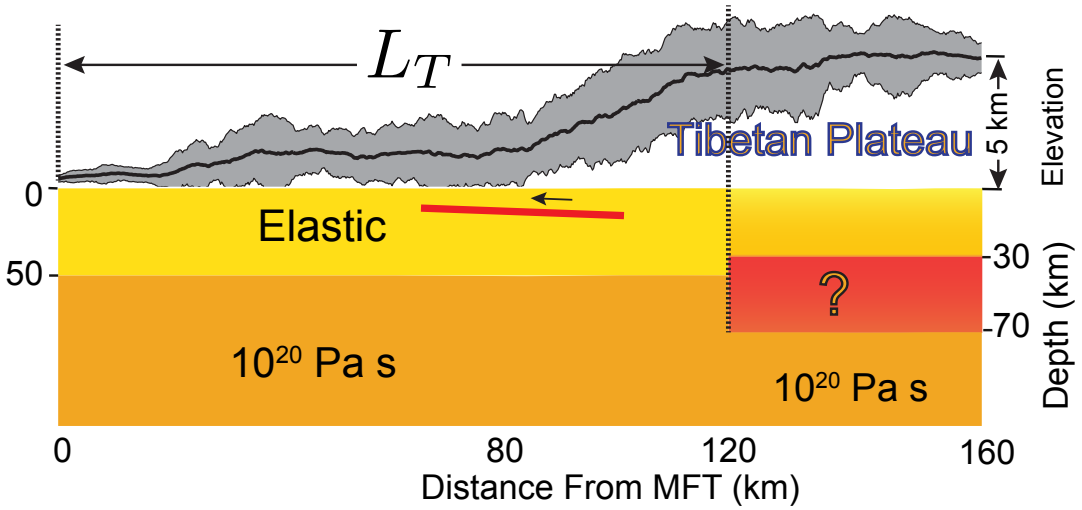

Figure 4.15: Model setup for the heterogeneous rheologic structure of the lithosphere across Himalaya. Red solid line denotes the 2015 Gorkha earthquake rupture. A lateral transition in rheology of the lower crust occurs at a distance L_T from the MFT surface trace. The entire 50 km thick Indian crust and the top 30 km of the Tibetan crust are assumed to be elastic. The upper mantle beneath both the Indian plate the southern Tibet is assumed to be visco-elastic with an effective viscosity of 10^{20} Pa s.

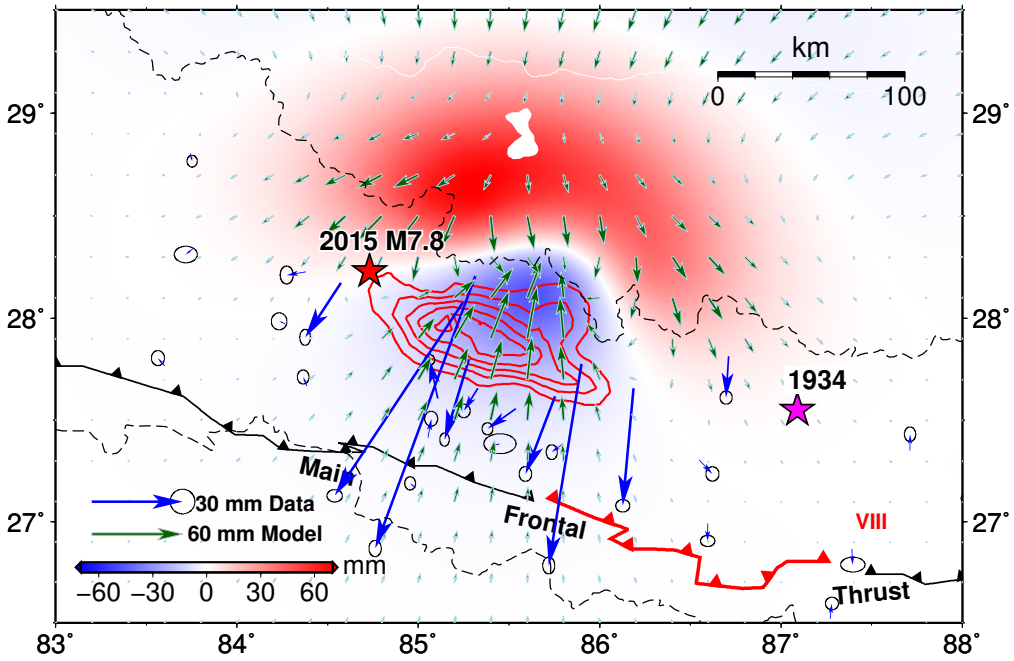

Figure 4.16: Predicted surface displacements due to viscoelastic relaxation for a heterogeneous rheologic structure with L_T=120 km and $\eta_T = 10^{18}$ Pa s (see Figure 4.15). Color represents vertical displacements.

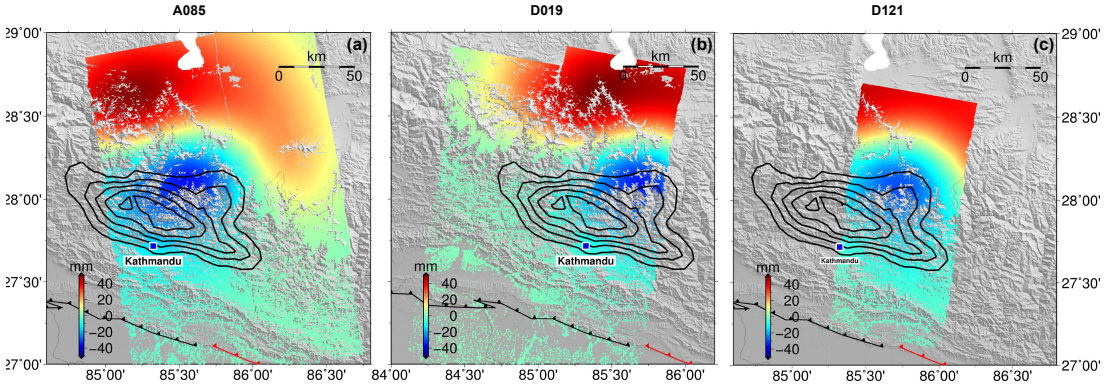

Figure 4.17: Predicted InSAR LOS displacements due to viscoelastic relaxation for a heterogeneous rheologic structure with L_T=120 km and $\eta_T = 10^{18}$ Pa s (see Figure 4.15).

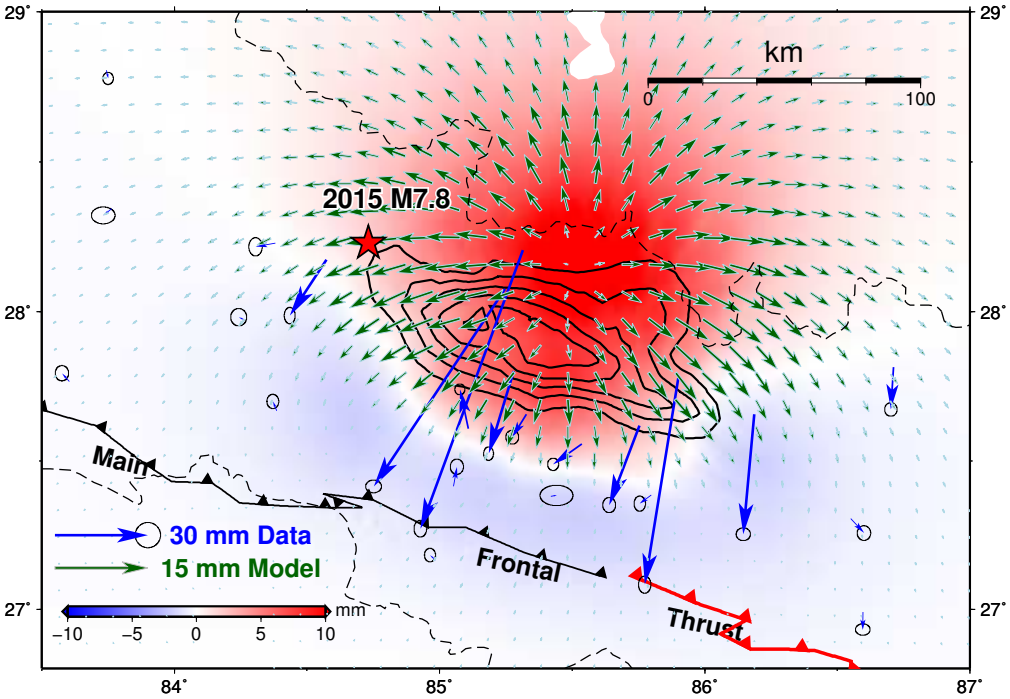

Figure 4.18: A comparison between GPS observations and predicted surface displacements due to poroelastic rebound.

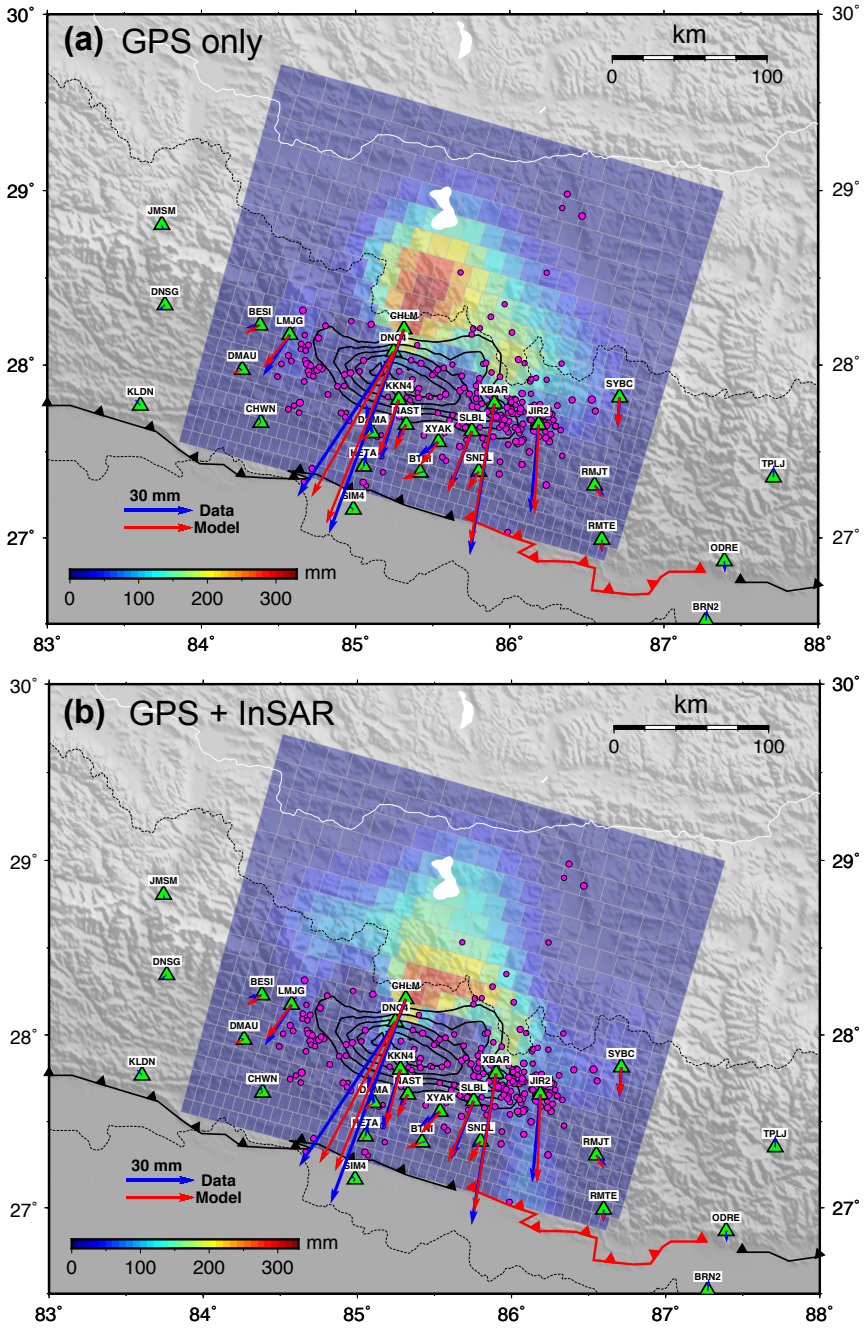

Figure 4.19: Kinematic inversions for afterslip following the 2015 Gorkha earthquake using (a) the horizontal GPS displacements only, (b) both GPS and InSAR LOS displacements. Purple circles denote the $M4+$ aftershocks.

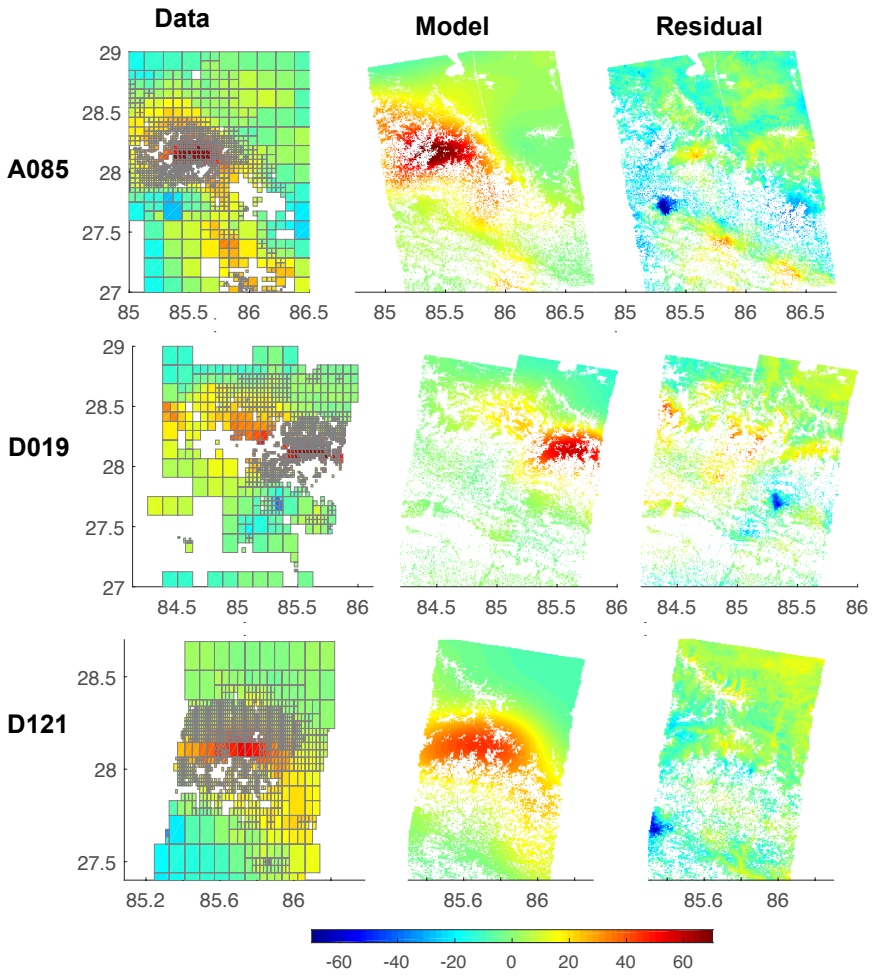

Figure 4.20: Comparison of the observed and modeled LOS displacements due to afterslip from three Sentinel-1 tracks. Original LOS displacements shown in Figure 4.11 were scaled according to the observation period of each track to match the time span of the GPS observations, as described in the main text. Downsampling of InSAR data was performed iteratively using best-fitting models in each iteration (see (*Wang and Fialko*, 2015) for details). Color denotes the displacement amplitude, in mm.

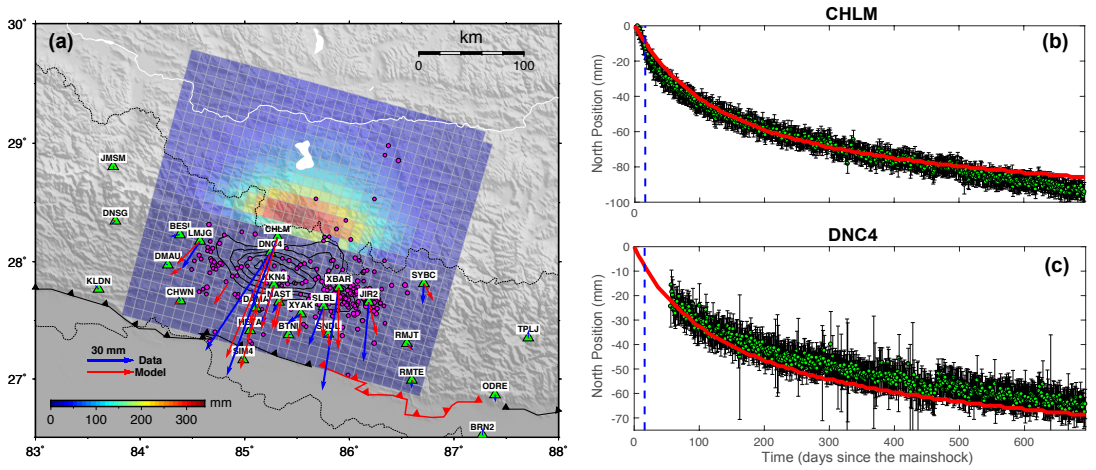

Figure 4.21: A comparison between the GPS observations and stress-driven afterslip models. (a) Cumulative afterslip predicted by the stress-driven afterslip model during the GPS observation period. (b) and (c) Observed (green dots with error bars) and predicted (red curve) time series of the north component of the displacement time series at the GPS sites CHLM and DNC4, respectively.

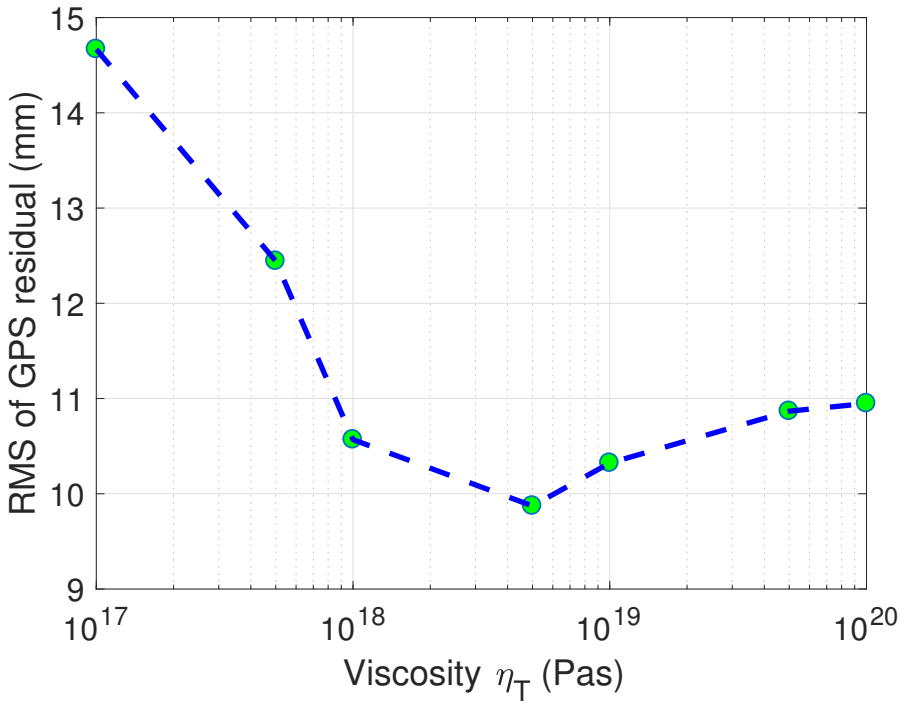

Figure 4.22: RMS of the difference between visco-elastic models and the residual GPS displacements (after subtracting the displacements due to afterslip) as a function of the effective viscosity η_T in the lower crust of southern Tibet.

Bibliography

Abaqus/Simulia (2017), A general purpose three-dimensional finite element program, http://www.3ds.com/products/simulia/overview/.

Ader, T., J.-P. Avouac, J. Liu-Zeng, H. Lyon-Caen, L. Bollinger, J. Galetzka, J. Genrich, M. Thomas, K. Chanard, S. N. Sapkota, S. Rajaure, P. Shrestha, L. Ding, and M. Flouzat (2012), Convergence rate across the Nepal Himalaya and interseismic coupling on the Main Himalayan Thrust: Implications for seismic hazard, *Journal of Geophysical Research: Solid Earth*, *117*, B04,403, doi:10.1029/2011JB009071.

Avouac, J.-P. (2003), Mountain building, erosion, and the seismic cycle in the Nepal Himalaya, *Advances in Geophysics*, *46*, 1–80, doi:http://dx.doi.org/10.1016/S0065-2687(03)46001-9.

Avouac, J. P. (2007), Dynamic processes in extensional and compressional cettings – mountain building: From earthquakes to geological Deformation, in *Treatise on Geophysics*, pp. 377–439, Elsevier.

Barbot, S., and Y. Fialko (2010), A unified continuum representation of post-seismic relaxation mechanisms: semi-analytic models of afterslip, poroelastic rebound and viscoelastic flow, *Geophysical Journal International.*, *182*, 1124–1140, doi:10.1111/j.1365-246X.2010.04678.x.

Barbot, S., Y. Hamiel, and Y. Fialko (2008), Space geodetic investigation of the coseismic and postseismic deformation due to the 2003 Mw 7.2 Altai earthquake: Implications for the local lithospheric rheology, *Journal of Geophysical Research: Solid Earth*, *113*(B3), B03,403, doi:10.1029/2007JB005063.

Barbot, S., Y. Fialko, and Y. Bock (2009), Postseismic deformation due to the Mw 6.0 2004 Parkfield earthquake: Stress-driven creep on a fault with spatially variable rate-and-state friction parameters, *Journal of Geophysical Research: Solid Earth*, *114*(B7), B07,405, doi:10.1029/2008JB005748.

Berardino, P., G. Fornaro, R. Lanari, and E. Sansosti (2002), A new algorithm for surface deformation monitoring based on small baseline differential sar interferograms, *IEEE Transactions on Geoscience and Remote Sensing*, *40*(11), 2375–2383, doi:10.1109/TGRS.2002.803792.

Brocher, T. M. (2005), Empirical relations between elastic wavespeeds and density in the Earth's crust, *Bulletin of the Seismological Society of America*, *95*(6), 2081–2092, doi:10.1785/0120050077.

Burov, E., and A. Watts (2006), The long-term strength of continental lithosphere: "jelly sandwich", or "crème brûlée"?, *GSA Today*, *16*, 4–10, doi:10.1130/1052-5173(2006)016⟨4.

Clark, M. K., and L. H. Royden (2000), Topographic ooze: Building the eastern margin of Tibet by lower crustal flow, *Geology*, *28*(8), 703–706, doi:10.1130/0091-7613(2000)28⟨703:TOBTEM⟩2.0.

Dieterich, J. H. (1979), Modeling of rock friction 1. Experimental results and constitutive equations, *Journal of Geophysical Research: Solid Earth*, *84*, 2161–2168, doi:10.1029/JB084iB05p02161.

Ding, X., Z. Li, J. Zhu, G. Feng, and J. Long (2008), Atmospheric effects on InSAR measurements and their mitigation, *Sensors*, *8*(9), 5426–5448, doi:10.3390/s8095426.

Elliott, J. R., R. Jolivet, P. J. González, J. P. Avouac, J. Hollingsworth, M. P. Searle, and V. L. Stevens (2016), Himalayan megathrust geometry and relation to topography revealed by the Gorkha earthquake, *Nature Geoscience*, *9*(2), 174–180, doi:10.1038/ngeo2623.

Fan, W., and P. M. Shearer (2015), Detailed rupture imaging of the 25 April 2015 Nepal earthquake using teleseismic P waves, *Geophysical Research Letters*, *42*(14), 5744–5752, doi:10.1002/2015GL064587.

Farr, T., and M. Kobrick (2000), Shuttle Radar Topography Mission produces a wealth of data, *AGU EOS*, *81*, 583–585.

Feng, W., E. Lindsey, S. Barbot, S. Samsonov, K. Dai, P. Li, Z. Li, R. Almeida, J. Chen, and X. Xu (2016), Source characteristics of the 2015 Mw 7.8 Gorkha (Nepal) earthquake and its Mw 7.2 aftershock from space geodesy, *Tectonophysics*, doi:https://doi.org/10.1016/j.tecto.2016.02.029.

Ferretti, A., C. Prati, and F. Rocca (2001), Permanent scatterers in SAR interferometry, *IEEE Transactions on Geoscience and Remote Sensing*, *39*(1), 8–20, doi:10.1109/36.898661.

Gonzalez-Ortega, A., Y. Fialko, D. Sandwell, F. Alejandro Nava-Pichardo, J. Fletcher, J. Gonzalez-Garcia, B. Lipovsky, M. Floyd, and G. Funning (2014), El Mayor-Cucapah (M_w7.2) earthquake: Early near-field postseismic deformation from InSAR and GPS observations, *Journal of Geophysical Research: Solid Earth*, *119*(2), 1482–1497, doi:10.1002/2013JB010193.

Gualandi, A., J.-P. Avouac, J. Galetzka, J. F. Genrich, G. Blewitt, L. B. Adhikari, B. P. Koirala, R. Gupta, B. N. Upreti, B. Pratt-Sitaula, and J. Liu-Zeng (2016), Pre- and post-seismic deformation related to the 2015, Gorkha earthquake, Nepal, *Tectonophysics*, doi:https://doi.org/10.1016/j.tecto.2016.06.014.

Herring, T., R. King, and S. McClusky (2015), Introduction to GAMIT/GLOBK.

Hooper, A., H. Zebker, P. Segall, and B. Kampes (2004), A new method for measuring deformation on volcanoes and other natural terrains using InSAR persistent scatterers, *Geophysical Research Letters*, *31*(23), L23,611, doi: 10.1029/2004GL021737.

Hooper, A., P. Segall, and H. Zebker (2007), Persistent scatterer interferometric synthetic aperture radar for crustal deformation analysis, with application to Volcán Alcedo, Galápagos, *Journal of Geophysical Research: Solid Earth*, *112*(B7), B07,407, doi:10.1029/2006JB004763.

Huang, M.-H., R. Bürgmann, and A. M. Freed (2014), Probing the lithospheric rheology across the eastern margin of the Tibetan Plateau, *Earth and Planetary Science Letters*, *396*, 88–96, doi:https://doi.org/10.1016/j.epsl.2014.04.003.

Lavé, J., and J.-P. Avouac (2000), Active folding of fluvial terraces across the siwaliks hills, himalayas of central nepal, *Journal of Geophysical Research: Solid Earth*, *105*(B3), 5735–5770, doi:10.1029/1999JB900292.

Lindsey, E. O., R. Natsuaki, X. Xu, M. Shimada, M. Hashimoto, D. Melgar, and D. T. Sandwell (2015), Line-of-sight displacement from ALOS-2 interferometry: Mw 7.8 Gorkha Earthquake and Mw 7.3 aftershock, *Geophysical Research Letters*, *42*(16), 6655–6661, doi:10.1002/2015GL065385.

Marone, C. (1998), Laboratory-derived friction laws and their applicaiton to seismic faulting, *Annual Review of Earth and Planetary Sciences*, *26*(1), 643–696, doi:https://doi.org/10.1146/annurev.earth.26.1.643.

Melosh, H., and A. Raefsky (1981), A simple and efficient method for introducing faults into finite element computations, *Bulletin of the Seismological Society of America*, *71*(5), 1391–1400.

Mencin, D., R. Bendick, B. N. Upreti, D. P. Adhikari, A. P. Gajurel, R. R. Bhattarai, H. R. Shrestha, T. N. Bhattarai, N. Manandhar, J. Galetzka, et al. (2016),

Himalayan strain reservoir inferred from limited afterslip following the Gorkha earthquake, *Nature Geoscience*, *9*, 533–537, doi:10.1038/ngeo2734.

Mitchell, E., Y. Fialko, and K. M. Brown (2016), Velocity-weakening behavior of Westerly granite at temperature up to 600° C, *Journal of Geophysical Research: Solid Earth*, *121*, 6932–6946, doi:10.1029/2012GC004241.

Monsalve, G., A. Sheehan, C. Rowe, and S. Rajaure (2008), Seismic structure of the crust and the upper mantle beneath the himalayas: Evidence for eclogitization of lower crustal rocks in the indian plate, *Journal of Geophysical Research: Solid Earth*, *113*(B8), doi:10.1029/2007JB005424, b08315.

Nábělek, J., G. Hetényi, J. Vergne, S. Sapkota, B. Kafle, M. Jiang, H. Su, J. Chen, B.-S. Huang, and H.-C. Team (2009), Underplating in the Himalaya-Tibet collision zone revealed by the Hi-CLIMB experiment, *Science*, *325*(5946), 1371–1374, doi:10.1126/science.1167719.

Okada, Y. (1985), Surface deformation due to shear and tensile faults in a half-space, *Bulletin of the Seismological Society of America*, *75*(4), 1135–1154.

Parker, A. L., J. Biggs, R. J. Walters, S. K. Ebmeier, T. J. Wright, N. A. Teanby, and Z. Lu (2015), Systematic assessment of atmospheric uncertainties for InSAR data at volcanic arcs using large-scale atmospheric models: Application to the cascade volcanoes, united states, *Remote Sensing of Environment* , *170*, 102–114, doi:https://doi.org/10.1016/j.rse.2015.09.003.

Qiu, Q., E. M. Hill, S. Barbot, J. Hubbard, W. Feng, E. O. Lindsey, L. Feng, K. Dai, S. V. Samsonov, and P. Tapponnier (2016), The mechanism of partial rupture of a locked megathrust: The role of fault morphology, *Geology*, *44*(10), 875–878, doi:10.1130/G38178.1.

Rousset, B., S. Barbot, J.-P. Avouac, and Y.-J. Hsu (2012), Postseismic deformation following the 1999 Chi-Chi earthquake, Taiwan: Implication for lower-crust rheology, *Journal of Geophysical Research: Solid Earth*, *117*(B12), B12,405, doi:10.1029/2012JB009571, b12405.

Royden, L. H., B. C. Burchfiel, R. W. King, E. Wang, Z. Chen, F. Shen, and Y. Liu (1997), Surface deformation and lower crustal flow in eastern Tibet, *Science*, *276*(5313), 788–790, doi:10.1126/science.276.5313.788.

Ryder, I., R. Bürgmann, and F. Pollitz (2011), Lower crustal relaxation beneath the Tibetan Plateau and Qaidam Basin following the 2001 Kokoxili earthquake, *Geophysical Journal International*, *187*(2), 613–630, doi:10.1111/j.1365-246X.2011.05179.x.

Ryder, I., H. Wang, L. Bie, and A. Rietbrock (2014), Geodetic imaging of late postseismic lower crustal flow in Tibet, *Earth and Planetary Science Letters*, *404*, 136–143, doi:https://doi.org/10.1016/j.epsl.2014.07.026.

Sandwell, D., R. Mellors, X. Tong, M. Wei, and P. Wessel (2011), Open radar interferometry software for mapping surface deformation, *EOS Transactions AGU*, *92*(28), doi:10.1029/2011EO280002.

Schulte-Pelkum, V., G. Monsalve, A. Sheehan, M. R. Pandey, S. Sapkota, R. Bilham, and F. Wu (2005), Imaging the Indian subcontinent beneath the Himalaya, *Nature*, *435*(7046), 1222–1225, doi:10.1038/nature03678.

Takeuchi, C., and Y. Fialko (2012), Dynamic models of interseismic deformation and stress transfer from plate motion to continental transform faults, *Journal of Geophysical Research: Solid Earth*, *117*, B05,403, doi:10.1029/2011JB009056.

Takeuchi, C., and Y. Fialko (2013), On the effects of thermally weakened ductile shear zones on postseismic deformation, *Journal of Geophysical Research: Solid Earth*, *118*, 6295–6310, doi:10.1002/2013JB010215.

Tong, X., and D. Schmidt (2016), Active movement of the Cascade landslide complex in Washington from a coherence-based InSAR time series method, *Remote Sensing of Environment*, *186*, 405–415, doi:https://doi.org/10.1016/j.rse.2016.09.008.

Tymofyeyeva, E., and Y. Fialko (2015), Mitigation of atmospheric phase delays in InSAR data, with application to the eastern California shear zone, *Journal of Geophysical Research: Solid Earth*, *120*(8), 5952–5963, doi:10.1002/2015JB011886.

Wang, K., and Y. Fialko (2014), Space geodetic observations and models of postseismic deformation due to the 2005 M7.6 Kashmir (Pakistan) earthquake, *Journal of Geophysical Research: Solid Earth*, *119*(9), 7306–7318, doi:10.1002/2014JB011122.

Wang, K., and Y. Fialko (2015), Slip model of the 2015 Mw 7.8 Gorkha (Nepal) earthquake from inversions of ALOS-2 and GPS data, *Geophysical Research Letters*, *42*(18), 7452–7458, doi:10.1002/2015GL065201.

Wang, R., F. Lorenzo-Martín, and F. Roth (2006), PSGRN/PSCMP–a new code for calculating co-and post-seismic deformation, geoid and gravity changes based on the viscoelastic-gravitational dislocation theory, *Computers & Geosciences*, *32*(4), 527–541, doi:https://doi.org/10.1016/j.cageo.2005.08.006.

Whipple, K. X., M. Shirzaei, K. V. Hodges, and J. R. Arrowsmith (2016), Active shortening within the Himalayan orogenic wedge implied by the 2015 Gorkha earthquake, *Nature Geoscience.*, *9*(9), 711–716, doi:doi:10.1038/ngeo2797.

Xu, X., D. T. Sandwell, E. Tymofyeyeva, A. González-Ortega, and X. Tong (2017), Tectonic and anthropogenic deformation at the Cerro Prieto geothermal step-over revealed by Sentinel-1A InSAR, *IEEE Transactions on Geoscience and Remote Sensing*, doi:10.1109/TGRS.2017.2704593.

Zhao, W.-L., and W. J. Morgan (1987), Injection of Indian crust into Tibetan lower crust: A two-dimensional finite element model study, *Tectonics*, *6*(4), 489–504, doi:10.1029/TC006i004p00489.

Chapter 5

Postseismic deformation due to the 2013 Mw 7.7 Balochistan earthquake observed with Sentinel-1 Interferometry

Abstract

The Mw 7.7 Balochistan earthquake occurred on September 24th, 2013 in southwestern Pakistan. The earthquake rupture was characterized by mostly left-lateral strike slip, with a limited thrust component, on the non-vertical (dip angle of 45-75 deg.) Hoshab fault in the Makran accretionary wedge. We used Interferometric Synthetic Aperture Radar (InSAR) data from Sentinel-1 mission

to derive the time series of postseismic displacements due to the 2013 Balochistan earthquake. Data from one ascending and two descending satellite tracks reveal robust post-seismic deformation during the observation period (November 2014 to April 2017). The postseismic InSAR observations are characterized by the line of sight (LOS) displacements primarily on the hanging wall side of the fault. The LOS displacements have different signs in data from the ascending and descending tracks (decreases and increases in the radar range, respectively), indicating that the postseismic deformation following the 2013 Balochistan earthquake was dominated by horizontal motion with the same sense as the coseismic motion. Kinematic inversions show that the observed InSAR LOS displacements are well explained by the left-lateral afterslip downdip of the high coseismic slip area. Contributions from the viscoelastic relaxation and poroelastic rebound seem to be small during the observation period. We also observe a sharp discontinuity in the postseismic displacement field on the North-East continuation of the 2013 rupture, along the Chaman fault. We verify that this discontinuity is not due to aftershocks, as the relative LOS velocities across this discontinuity show a gradually decelerating motion throughout the observation period. These observations are indicative of a creeping fault segment at the North-East end of the 2013 earthquake rupture that likely acted as a barrier to the rupture propagation. Analysis of Envisat data acquired prior to the 2013 event (2004-2010) confirms creep on the respective fault segment at a rate of 5-6 mm/yr. The creep rate has increased by more than an order of magnitude after the 2013 event. The inferred along-strike variations in

the degree of fault locking may be analogous to those on the central section of the San Andreas fault in California.

5.1 Introduction

The M_w 7.7 Balochistan earthquake occurred on September 24th, 2013 in southwestern Pakistan (Figure 5.1). Tectonically, the 2013 Balochistan earthquake occurred within a complex plate boundary where several major plates meet (*Avouac et al.*, 2014; *Jolivet et al.*, 2014). To the east, the India plate slides northward relative to the Eurasia plate along the Chaman fault system, a ∼1200 km long left-lateral fault system running from offshore of the Markran Coast of Pakistan all the way northward to Hindu Kush where it merges with the Pamir fault system (*Fattahi and Amelung*, 2016; *Szeliga et al.*, 2012). To the south, the Arabia and Ormara plates subduct northward beneath the Eurasia plate at a rate of ∼30 mm/yrs along the Makran range (*Ambraseys and Bilham*, 2003; *Lawrence et al.*, 1981). The 2013 Balochistan earthquake ruptured the Hoshab fault, a curved segment in the Makran range connecting the the left-lateral Chaman fault system to the northeast and the fold-and-thrust structures in the accretionary wedge to the southwest.

Geodetic and seismological observations suggest that the 2013 Balochistan earthquake involved mostly left-lateral strike slip, with a limited thrust component (*Avouac et al.*, 2014; *Jolivet et al.*, 2014; *Vallage et al.*, 2015, 2016), while

the fault dips $\sim 45 - 75^{\circ}$ to the northwest. Such a large strike-slip earthquake in an overall compressional regime is unprecedented. To reconcile the strike-slip motion with the overall crustal shortening within the accretionary prism, various hypotheses have been proposed, including dynamic stresses during the rupture on a curved fault (*Avouac et al.*, 2014), time-varying fault kinematics between multiple earthquakes (*Avouac et al.*, 2014) and bimodal slip behavior (*Barnhart et al.*, 2015). These ideals largely arise from the interpretation of coseismic surface displacements determined from optical and Synthetic Aperture Radar (SAR) satellite imagery.

Large earthquakes generate sudden stress changes in the ambient rocks that may lead to various postseismic relaxation processes. Commonly considered postseismic relaxation mechanisms include afterslip, poroelastic rebound and viscoelastic relaxations. If relative contribution from those mechanisms to the observed surface deformation can be evaluated, the latter may provide valuable information about in situ mechanical properties of the fault system and host rocks. However, discrimination of various deformation mechanisms is often hindered by the similarities in surface deformation patterns produced by different relaxation processes, especially in case of strike-slip earthquakes. While dominated by strikes-slip, the 2013 Balochistan earthquake occurred on a curved dipping fault. Such fault geometry may introduce substantial asymmetry in stress changes to facilitate discrimination of the different relaxation mechanisms. In this study, we use C-band Interferometric Synthetic Aperture Radar (InSAR) data collected by the

Sentinel-1A satellite to derive the time series of the postseismic displacements following the 2013 Balochistan earthquake. We compare the observed surface deformation with model of various postseismic relaxation processes to understand how the lithosphere responds to the stress changes due to the 2013 Balochistan earthquake.

5.2 Data

Data used in this study are from three tracks (one ascending track A115 and two ascending tracks D049 and D151) of Sentinel-1A (S1A) satellite covering the epicentral area of the 2013 Balochistan earthquake. There are between 35-40 scenes for each track, spanning the time period from October 2014 to April 2017. We processed the data with GMT5SAR (*Xu et al.*, 2017). The interferograms were unwrapped using the statistical-cost network-flow algorithm (SNAPHU) (*Chen and Zebker*, 2002). As InSAR range change is a relative measurement between two image acquisitions, the unwrapped phase is intrinsically ambiguous by the modulo of 2π. Because of the excellent performance in the Sentinel-1 SAR system, the sum of the wrapped phase around a closed loop is zero (*Wang and Fialko*, 2017; *Xu et al.*, 2017). Any nonzero phase closure indicates an ambiguity in the phase unwrapping. We thus formed all possible triangular loops to check the phase residual along those loops and then solved for the unwrapping ambiguity for each interferogram in a least-square sense such that after correction the unwrapped

phase is zero for any combination of interferograms forming a closed loop. We note that such a consistency check still allows for a multiple of 2π shift in all interferograms. This will not affect the time series analysis if the radar phase in each interferogram is referenced to a common pixel (ideally, chosen in a correlated stable area not affected by the deformation).

Because of the arid and sparsely vegetated environment in the Makran Coastal Range, the study area is characterized by high correlation of radar phase, except in the Balochistan desert where the reflective properties of the back-scatters may be highly variable due to the movement of the sand. Figure 5.2 shows range changes for the sequential interferograms (generated from two consecutive SAR images) along the ascending track A115. As shown in the figure, most of the interferograms are severely affected by the long-wavelength artifacts. Range changes across some of the interferograms are up to ~ 20 cm. Such large LOS displacements are unlikely due to the ground motion given the short time spans of the interferograms (12 to 24 days). We note that these ramp-like artifacts are not likely due to the orbital errors either, as a large orbital errors would result in significant phase discontinuities across the burst boundaries for TOPS SAR system which relies on orbital information for the image alignment. Except in a few interferograms made with images acquired in the very early stage of the mission, the burst discontinuities in most of the interferograms are negligible, implying the accuracy of the orbital control of the Sentinel-1 satellites. Instead, the long-wavelength artifacts are most likely due to the atmospheric phase delays. Atmospheric phase delays may con-

sist of stratified and turbulent components. The stratified component is expected to spatially correlate with topography and exhibit systematic temporal (e.g. seasonal) variations. The turbulent component, on the other hand, is expected to be essentially random both spatially and temporally. We applied the method of common-scene-stacking (CSS) (*Tymofyeyeva and Fialko*, 2015) to estimate the atmospheric phase screens (APS) corresponding to the turbulent component of the atmospheric delays. To reduce the potential aliasing of the turbulent atmospheric delays with the stratified component, we constrained the temporal baselines of the interferograms to be less than 90 days, 1/4 of the annual cycle expected of the seasonal variations.

Figure 5.3 shows the estimated atmospheric phase screens (APS) for the SAR images from the ascending track A115. Notably, the estimated APS capture not only the long-wavelength phase ramps, but also sharp discontinuities seen in some of the original interferograms. These discontinuities are unlikely due to unwrapping errors, as suggested by the high phase coherence across the respective boundaries. Instead, they are more likely related to development of precipitation along sharp fronts. The unwrapped phase after subtracting the estimated APS is shown in Figure 5.4. Compared to the original interferograms, the range changes in most of the APS-corrected interferograms are much smaller.

Interferograms corrected using the common-scene-stacking (CSS) described above may contain residual noise due to the stratified component of the atmospheric delay. We thus applied a correction for the elevation-dependent humidity

by performing a linear regression between the APS-corrected radar phase and the digital elevation model. We excluded the earthquake rupture area in this estimation to prevent a possible contribution from surface deformation. Interferograms were also flattened by subtracting the best fitting plane to account for potential orbital errors.

Upon removing the estimated atmospheric contributions, we computed the time series of the surface displacements along the satellite's line-of sight (LOS) using Small Baseline Subset (SBAS) method (e.g. *Berardino et al.*, 2002; *Schmidt and Bürgmann*, 2003; *Tong and Schmidt*, 2016). To reduce the error, we excluded the interferograms containing images of the first and last acquisition for each track, which effectively had no APS estimation in the common-scene-stacking step. The resulting cumulative LOS displacements during the respective observation period of each track (A115, D049 and D151) are shown in Figure 5.5. The postseismic InSAR observations reveal significant radar range changes primarily on the hanging wall side of the fault. The LOS displacements have different signs in data from the ascending and descending tracks (decreases and increases in the radar range, respectively), indicating that the postseismic deformation following the 2013 Balochistan earthquake was dominated by horizontal motion with the same sense as the coseismic motion. The LOS displacements in areas of maximum signal amplitude exhibit a clear time-decaying signal, consistent with the feature of a postseismic transient (Figure 5.5d). Among all three tracks, data from the ascending track A115 have the highest signal-to-noise ratio (SNR). LOS displace-

ments in this track are characterized by a monotonic range decrease throughout the observation period (Figure 5.6). The cumulative LOS displacements reach up to ∼150 mm at some locations (e.g. ∼ 20 km west of the rupture trace, Figure 5.5a).

Interseismic deformation rate across the fault system in the Makran accretionary prism, including the Hoshab fault, is ∼ 10 mm/yr (*Frohling and Szeliga*, 2016; *Penney et al.*, 2017), too small to explain the InSAR LOS displacements shown in Figure 5.5. Both the amplitude and the time dependence of the observed anomaly suggest that latter represents the postseismic deformation due to 2013 Balochistan earthquake. In the next section, we will quantitatively analyze the surface displacement fields expected of various relaxation mechanism (i.e. poroelastic rebound, viscoelastic relaxation and afterslip) and compare them to our observations to explore what mechanism(s) may have contributed to the postseismic deformation following the 2013 Balochistan earthquake.

5.3 Modeling of Postseismic Relaxation

5.3.1 Poroelastic rebound

Coseismic deformation produces changes in pore fluid pressure in the brittle upper crust. The resulting gradients in pore fluid pressure lead to the fluid flow in the host rocks and surface deformation. We approximate the surface deformation due to the fully relaxed poroelastic rebound by differencing the coseismic displace-

ments under undrained and drained conditions. We assume that the top 20 km of the Earth's crust is fluid-saturated and the change in Poisson's ratio is 0.05 (from an undrained value of 0.30 to a drained value 0.25). The coseismic displacements are calculated using the the code EDGRN/EDCMP (*Wang et al.*, 2003).

Simulations of postseismic response depend on the assumed static slip model. Several coseismic slip models are available for the 2013 Balochistan earthquake from inversions of geodetic and seismic data (e.g. *Avouac et al.*, 2014; *Barnhart et al.*, 2014; *Jolivet et al.*, 2014). The fault geometries and slip distributions of these models are generally similar to each other. In this study, we adopted the coseismic slip model of (*Avouac et al.*, 2014), which has the smoothest slip distribution among the three models mentioned above for our simulations of postseismic relaxation.

Figure 5.7 shows the predicted surface displacements due to the poroelastic rebound projected onto the line of sight of the Sentinel-1A data used in this study. In contrast to the observations, the modeled surface displacements due to the poroelastic rebound primarily concentrate at the locations of fault geometry change, where the pore pressure change is largest. The maximum LOS displacements due to the poroelastic rebound are around $\sim$ 2 cm for all three tracks. By comparing the InSAR observations (Figure 5.5) and model predictions (Figure 5.7), we conclude that contribution of poroelastic rebound to the observed InSAR displacements (if any) is negligible.

5.3.2 Viscoelastic relaxation

We next evaluate the viscoelastic response of the lithosphere to stress changes caused by the 2013 Balochistan earthquake. As little is know about the lithospheric structure in the Makran range, we assumed a 1-D layered structure consisting of an elastic upper crust and viscoelastic half-space. The calculations was performed with PSGRN/PSCMP (*Wang et al.*, 2006). The difference in 3-D surface displacements corresponding to the last and first InSAR acquisition times is projected onto the line of sight of the respective InSAR track to yield the model predicted LOS displacements. Figure 5.8 shows the predicted LOS displacements due to viscoelastic relaxation assuming an a 25km thick elastic layer underlain by a visco-elastic half-space with the dynamic viscosity of 10^{18} Pas. The predicted LOS displacements due to the viscoelastic relaxation have comparable magnitudes but different sign in radar range change across the fault. While the viscoelastic relaxation model predicts LOS displacements of the same sign as the observations on the hanging wall side of the fault, it considerably over predicts the deformation on the footwall side of the fault. The predicted radar range changes (increases for the ascending track and decrease for the descending track) east of the 2013 rupture track are up to $\sim$ 10 cm, which is not seen in the InSAR data.

Changing the viscosity of the substrate and thickness of the elastic layer affects the magnitudes of the surface deformation during the observation period but does not change the overall pattern of surface deformation. Models assuming

more complex rheologies (e.g. Burgers or power-law) are expected to predict similar spatial patterns of surface deformation, as they mainly differ in the temporal evolution of the stress relaxation. The first-order differences between the observations (Figure 5.5) and model predictions, particularly on the footwall side of the fault (Figure 5.8), suggest that the viscoelastic relaxation may have played only a limited role in the postseismic relaxations following the 2013 Balochistan over a time period considered in in this study.

5.3.3 Afterslip

The observed postseismic deformation pattern of dominantly horizontal along-strike motion on the hanging wall side of the fault is quite similar to that of the coseismic displacement field (*Avouac et al.*, 2014; *Vallage et al.*, 2015), suggestive of a continued slip on the fault that produced the earthquake. To explore the spatial distribution of afterslip, we performed kinematic inversions of the observed surface displacements. We assumed that afterslip occured on the same fault as the coseismic rupture. The fault geometry is based on the coseismic slip model of (*Avouac et al.*, 2014), extended to the total width (downdip diminesion) of 60 km. We calculated the Green functions using analytic solutions for a dislocation in a homogeneous elastic half-space (*Okada*, 1985). The InSAR LOS displacements shown in Figure 5.5 were downsampled iteratively using surface strain from a curved best-fitting model (*Wang and Fialko*, 2015). Among all three tracks, data from the descending track D049 have the lowest signal-to-noise ratio (SNR). We

thus only used data from the ascending track A115 and descending track D151 in the inversion. Data from the descending track D049 are used as an independent check on the model predictions. A Laplacian smoothing is applied between adjacent fault patches to avoid abrupt variations in slip. The method of selecting the optimal values of smoothness and relative weighting between datasets follows (*Wang and Fialko*, 2015).

Figure 5.9a shows the best-fitting afterslip model derived from the Sentinel-1A data from the ascending track A115 and the descending track D151, based on the fault geometry of (*Avouac et al.*, 2014). The afterslip in found to occur primarily at the downdip extension of the coseismic rupture. The cumulative afterslip during the observation period (from November 2014 to April 2017) is over $\sim$ 0.6 meters. Assuming a shear modulus of 33 GPa, the moment release from the afterslip is $\sim 9 \times 10^{19} Nm$ (equivalent to an earthquake of moment magnitude 7.2), about 17% of the coseismic moment. Similar to the coseismic slip, afterslip following the 2013 Balochistan earthquake is also dominated by strike-slip, with a small component of thrust.

It was suggested that the subparallel fold-and-thrust fault systems within the Makran range are connected by a flat décollement at the depth of $\sim$ 10 km (e.g. *Smith et al.*, 2012). To test if such a décollement has involved in the post-seismic relaxation of the 2013 Balochistan earthquake, we next assumed that the fault segments have the same dip angles as in the model of planar faults (*Avouac et al.*, 2014) down to the depth of 15 km, and then transition to a décolloment

with a a dip angle of 15°. The resulting best-fitting afterslip model is shown in Figure 5.9b. Similar to the afterslip model with planar fault segments (hereafter called model A), the afterslip model with a décollement (hereafter called afterslip B) is also characterized by dominantly left-lateral slip downdip of the coseismic rupture, although there are some differences between the two models in details. Both afterslip models fit the observations reasonably well (Figure 5.10 and Figure 5.11). Model B produces a better overall fit to the data close to the fault trace where local decreases in radar range are present in the data from both descending tracks (D151 and D049). We note that the afterslip based on the décollement fault geometry is also predominantly left-lateral, though décollements are generally developed as a result of crustal shortening. Future observations (e.g. from Sentinel-1A/B and ALOS2) will be useful to provide better constraints on the afterslip duration, distribution and the corresponding fault geometries.

5.4 Surface creep northeast of the 2013 Balochistan rupture

InSAR observations in this study show that the maximum postseismic deformation following the 2013 Balochistan earthquake occurs in a region ∼20-30 km west of the fault trace (Figure 5.5), consistent with models of afterslip below the seismic asperity. Data from the ascending track A115, in addition, reveal a sharp discontinuity in the LOS displacement field on the North-East continuation of the

2013 Balochistan rupture (red box in Figure 5.5a), suggestive of fault creep at a shallow depth. To verify if such a surface creep was activated as a result of the 2013 Balochistan earthquake, we examined the InSAR data in this area acquired by the Envisat mission prior to the 2013 event. Envisat data used in this study are from the IS6 swath of the ascending track A027. There are 45 scenes available from 2004 to 2010. To optimize radar phase coherence, interferograms were made with temporal and perpendicular baselines no greater than 300 days and 400 meters, respectively. Compared with Sentinel-1 mission, acquisitions of the Envisat data were much less frequent in time. We thus simply stacked all the interferograms satisfying the baseline conditions described above to obtain the mean LOS velocities during the observation period.

Figures 5.12a and b show the InSAR LOS velocities in the area of surface creep before and after the 2013 Balochistan earthquake, respectively. Compared with the postseismic Sentinel-1 observations, interseismic LOS velocities derived from the Envisat data are noisier, as no atmospheric corrections were applied. Nevertheless, a sharp discontinuity in the interseismic LOS velocity is clearly visible at same location where the postseismic surface creep was detected. The LOS velocities along a profile perpendicular to the surface creep are shown in Figure 5.13. Clearly, both interseismic and postseismic measurements exhibit sharp discontinuities in the LOS velocities at the same location. The offset in the interseismic LOS velocities across this discontinuity is $\sim$ 2 mm/yr. Assuming that the fault motion in this area is purely horizontal and using the average fault strike of 21°,

the creep rate is estimated to be 5-6 mm/yr. The overall relative motion between the Indian plate and the Eurasian plate in this region is ~ 3 cm/yr, which is partitioned along several sinistral faults, including the Chaman fault, the Ormach-Nal fault, the Ghazaband fault, and the fold-and-thrust structures to the east (e.g. *Szeliga et al.*, 2012; *Ul-Hadi et al.*, 2013). While at present no exact estimation of the strain partitioning along the those faults is available, the observed fault creep of $5 - 6$ mm/yr seems to accommodate a significant fraction of the crustal deformation across the corresponding fault segment.

The surface creep rate after the 2013 Balochistan earthquake is at least 5 times larger than that before the event (Figure 5.12b). To examine the spatiotemporal evolution of surface creep, for each epoch of the InSAR time series, we extracted the relative displacements across the discontinuity in LOS velocity shown in Figure 5.12b at different locations along the fault. We note that no temporal smoothing and corrections for atmospheric noise were applied in this analysis. Figure 5.14a shows the time series of the relative LOS displacements across the surface creep at different locations. The surface creep increases monotonically with time, suggesting that it is not due to aftershocks. Compared with the LOS displacements on the hanging wall of the fault around the maximum coseismic slip areas, the creep northeast of the 2013 rupture continuation seems be relatively steady throughout the observation period. The difference in temporal evolution of the surface deformation is indicative of the spatial variation in the frictional properties on a fault. Note that our analysis does not include the first year of postseismic

deformation. The data also show that the postseismic creep rate decreases with an increase in the distance from the 2013 rupture (Figure 5.14b). This is expected as the stress perturbation decreases away from the coseismic rupture.

5.5 Discussion

Models of dynamic rupture suggest that creeping segments act as barriers to seismic ruptures but may also serve as sites for nucleation of major earthquakes (*Kaneko et al.*, 2010; *Lapusta and Liu*, 2009). Coseismic rupture of the 2013 Balochistan earthquake propagated almost unilaterally southward along the curved Hoshab fault, with considerably reduced slip on the fault segment north of the epicenter. It was suggested that the the 2013 Balochistan earthquake rupture was limited by a creeping segment north of its rupture (e.g, *Avouac et al.*, 2014; *Jolivet et al.*, 2014). Geodetic measurements, including GPS and InSAR, have identified a segment of aseismic surface creep between $\sim 30^\circ - 33^\circ$N along the Chaman fault system (*Fattahi and Amelung*, 2016; *Szeliga et al.*, 2012), a few hundreds kilometers away from the 2013 Balochistan earthquake. Measurements of surface creep on the segment near North-East continuation of the 2013 rupture, however, had never been reported. Surface creep reported in this study thus provides direct evidence in support of the view that a creeping segment acted as barrier at the north end of the 2013 rupture. Low interseismic coupling as a result of the aseismic creep may also explain the overall low level of seismic activity along the Chaman

fault system. The inferred along-strike variations in the degree of fault locking may be analogous to those on the central section of the San Andreas fault in California, but at a smaller scale.

Previous studies on postseismic deformation following large continental strike-slip events have faced the difficulty separating the contributions of various relaxation processes, yielding non-unique conclusions regarding the driving mechanisms. While the 2013 Balochistan earthquake was dominated by strike-slip rupture, predictions of surface deformation due to various relaxation mechanisms are distinct enough to identify the dominant process, thanks to a curved dipping fault geometry. Specifically, InSAR observations from three tracks with different look geometries reveal robust postseismic deformation primarily on the hanging wall side of the fault. Surface displacements due to viscoelastic relaxation in a 1-D layered structure, however, are nearly anti-symmetric across the fault. Poroelastic rebound model predicts small surface displacements, mostly in areas around the fault tips and kinks. Instead, presented observations of postseimic deformation following the 2013 Balochistan earthquake are best explained by an afterslip model with most of the slip occurring downdip of the coseismic rupture. The viscosity in the mid-to-lower crust along the Chaman fault system in western Pakistan is thought to be fairly low (e.g. *Ul-Hadi et al.*, 2013). Our simulation suggests that this may not be the case, as the viscoelastic relaxation model with a relatively small viscosity ($<= 10^{18}$ Pas) in the substrate would predict significant surface deformation on the footwall side of the fault (Figure 5.8), which is not observed

by the InSAR analysis in this study. Results of this study are consistent with the crustal deformation model in the Makran accretionary wedge proposed by (*Jolivet et al.*, 2014), in which the Arabian plate subducts sub-horizontally underneath the Eurasian plate to produce the seismicity in the upper crust, whereas convergence between the two plates in the lower crust is accommodated by aseismic slip along the décollement at the wedge basal during the interseismic and postseismic periods.

Postseismic relaxation following the 2013 Balochistan earthquake is similar to other recent earthquake of similar magnitudes along the Himalayan range, including the 2005 Mw 7.6 Kashmir (Pakistan) and the 2015 Mw 7.8 Gorkha (Nepal) earthquake. Postseismic transients years after these earthquakes were also found to be dominated by aseismic afterslip primarily downdip of the coseismic rupture (*Wang and Fialko*, 2014, 2017). Viscoelastic relaxation, on the other hand, was suggested to be prevalent in the postseismic response to large subduction earthquakes, particularly over longer time scales(e.g. *Hu et al.*, 2004; *Wang et al.*, 2012). Recently launched SAR missions, including Sentinel-1A/B and ALOS-2, continue to provide measurements of surface deformation at high spatial and temporal resolution worldwide. Data from these missions over longer periods and wider areas will be useful to establish if viscoelastic relaxation plays an important role in case of the respective earthquakes.

5.6 Conclusions

We used Interferometric Synthetic Aperture Radar (InSAR) data from Sentinel-1 mission to derive the postseismic displacements due to the 2013 Mw 7.7 Balochistan earthquake in the Makran accretionary wedge in southwestern Pakistan. Data from one ascending and two descending satellite tracks reveal robust post-seismic deformation during the observation period from November 2014 to April, 2017. The postseismic InSAR observations are characterized by the line of sight (LOS) displacements primarily on the hanging wall side of the fault. The LOS displacements have different signs in data from the ascending and descending tracks (decreases and increases in the radar range, respectively), indicating that the postseismic deformation following the 2013 Balochistan earthquake was dominated by horizontal motion with the same sense as the coseismic motion. Kinematic inversions show that the observed InSAR LOS displacements are well explained by the left-lateral afterslip downdip of the high coseismic slip area. Compared with afterslip, contributions from the viscoelastic relaxation and poroelastic rebound seem to be small during the observation period of this study. We also documented a fault segment of surface creep northeast of the 2013 Balochistan rupture that may have acted as a barrier to the rupture propagation. Using Envisat data acquired between 2004 and 2010, we estimated that the interseismic creep rate along this segment was $\sim$ 5-6 mm/yr. Stress perturbation from the 2013 event has enhanced the surface creep rate on by a factor of at least 5. The inferred along-strike

variations in the degree of fault locking may be analogous to those on the central section of the San Andreas fault in California.

Acknowledgement

Sentinel-1 data are provided by the European Space Agency (ESA) through Alaska Satellite Facility (ASF) and UNAVCO. Envisat data are from the ESA's On-the-Fly service. SAR data processing was performed on the Comet cluster at the San Diego Supercomputing Center (SDSC). Data and modeling results used in this study are available from the authors.

This chapter, in full, is a preprint of the material being prepared for the submission to *JGR*, which may appear as: Wang, K., and Y. Fialko, " Postseismic deformation due to the 2013 Balochistan earthquake observed with Sentinel-1 interferometry",*Journal of Geophysical Research: Solid Earth*. The author of this dissertation is the primary investigator of work presented in this chapter.

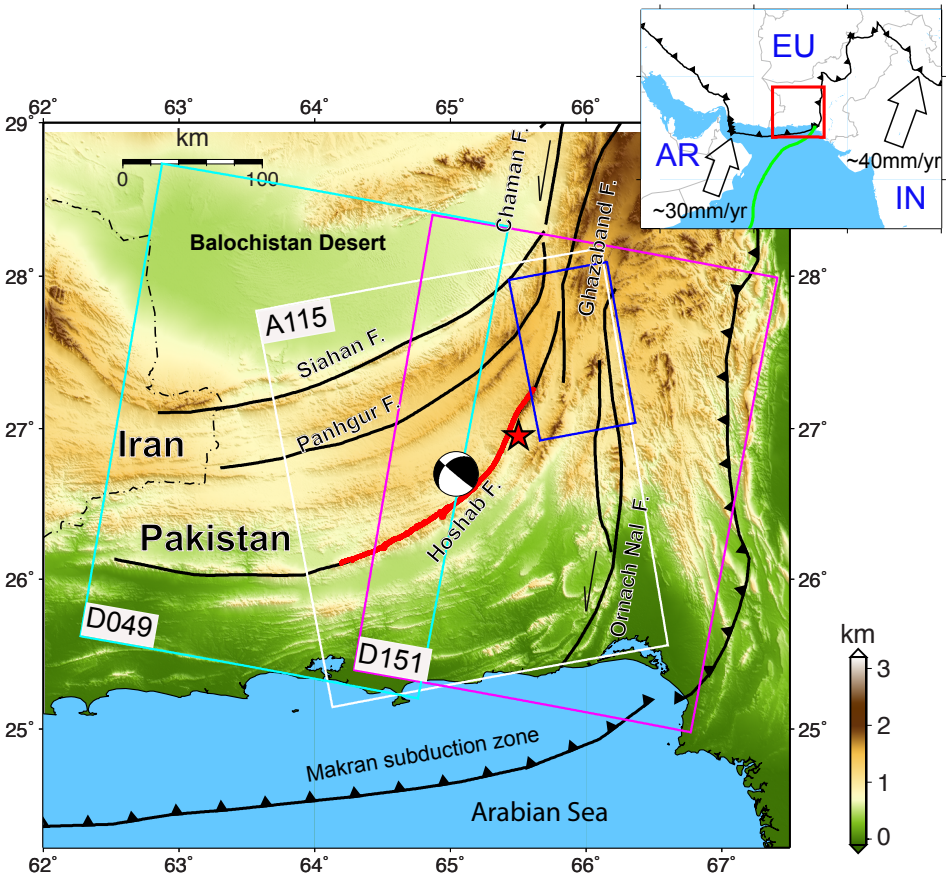

Figure 5.1: Tectonic setting of the 2013 Mw 7.7 Balochistan earthquake. Surface traces of the major active faults are from (*Mohadjer et al.*, 2016). Red thick curve denotes the surface trace of the fault ruptured in the 2013 Mw 7.7 Balochistan earthquake. Red star denotes the epicenter of the mainshock. Black beachball represents the location and focal mechanism of the centroid moment tensor of the mainshock. Solid line boxes show the scene coverages of SAR data used in this study (white, cyan and magenta are for the ascending track A115, descending track D049 and descending track D151 of the Sentinel-1A satellite, respectively; blue for the ascending track A027 of Envisat (IS6)). Inset shows the tectonic setting of the study area on a large scale. Plate boundary between the Arabian plate (AR) and Indian plate (IN) is denoted by the green line. The blacks line with triangles represents the boundary between the Arabian plate (AR) and the Eurasian plate (EU).

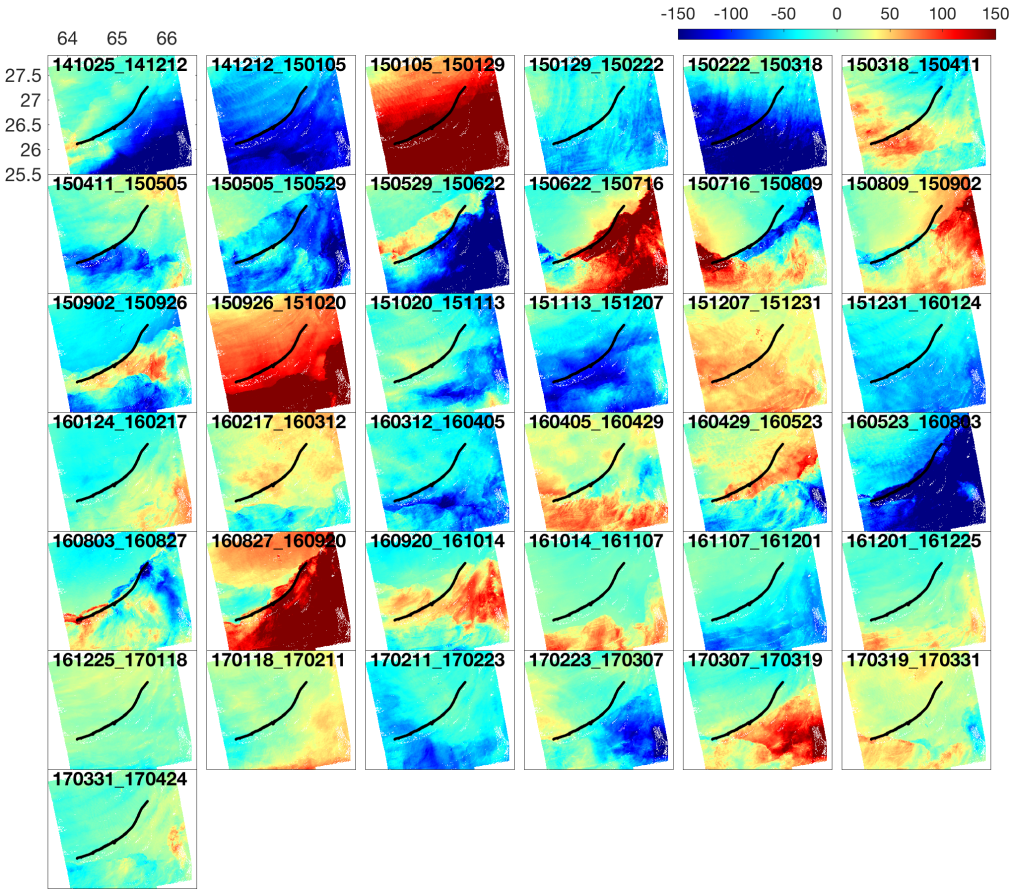

Figure 5.2: Radar range changes in sequential interferograms from the ascending track A115. Note that intertferograms between any two acquisition dates can be generated by simply summing up the sequential interferograms between the respective dates. Black curve in each panel denotes the surface trace of 2013 Balochistan rupture. Numbers in each panel denote the dates of the master and slave images (yymmdd). The radar range changes (colors) are in mm.

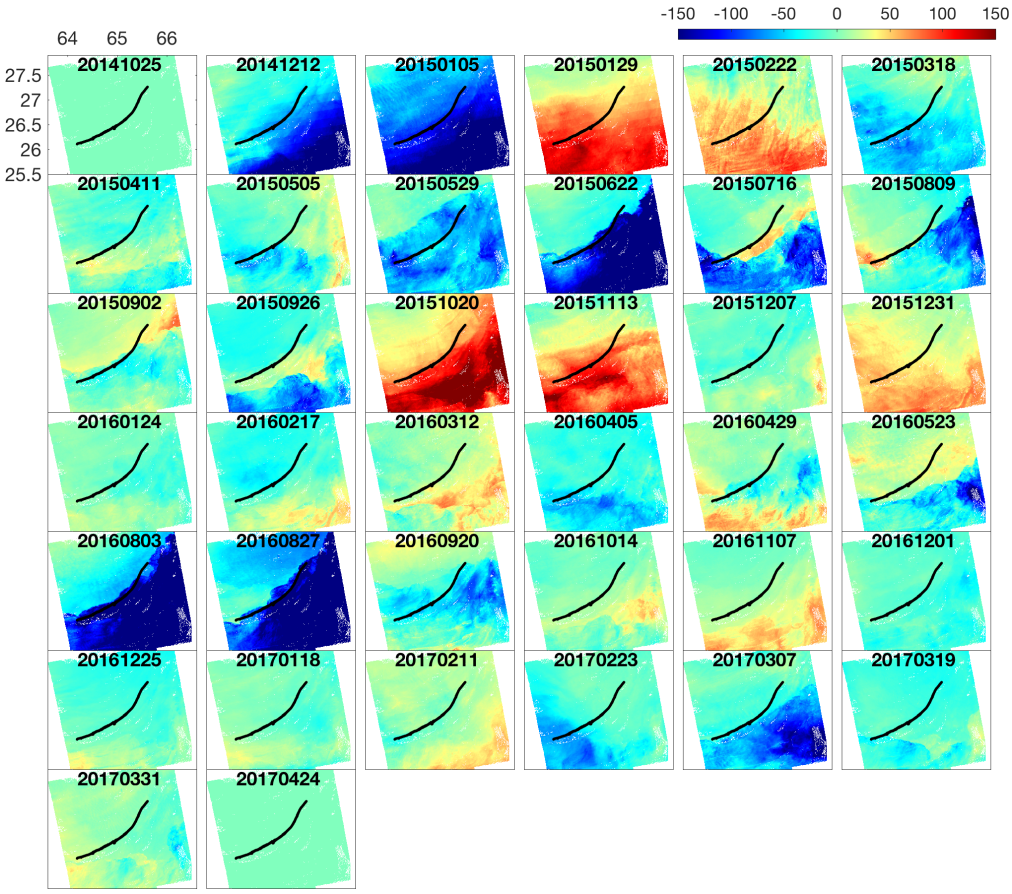

Figure 5.3: Estimated Atmospheric Phase Screens (APS) for SAR acquisitions from the ascending track A115 with Common-Scene-Stacking (CSS) (*Tymofyeyeva and Fialko*, 2015). Note that the estimated APS capture not only the long-wavelength phase ramps, but also sharp discontinuities seen in some of the original interferograms, which are likely related to development of precipitation along sharp fronts.

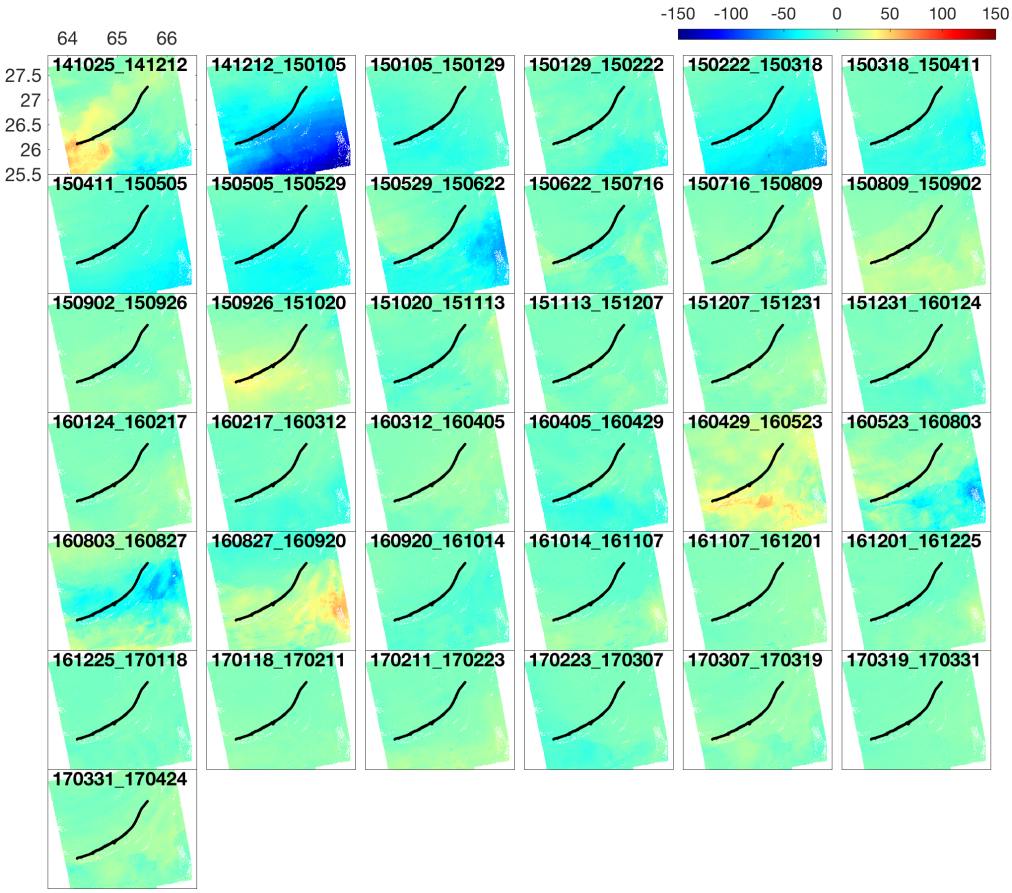

Figure 5.4: Radar range changes in the sequential interferograms from the ascending track A115 after subtracting the APS estimated with CSS. Black curve denote the surface trace of 2013 Balochistan rupture. Numbers in each panel denote the dates of SAR image acquisitions.

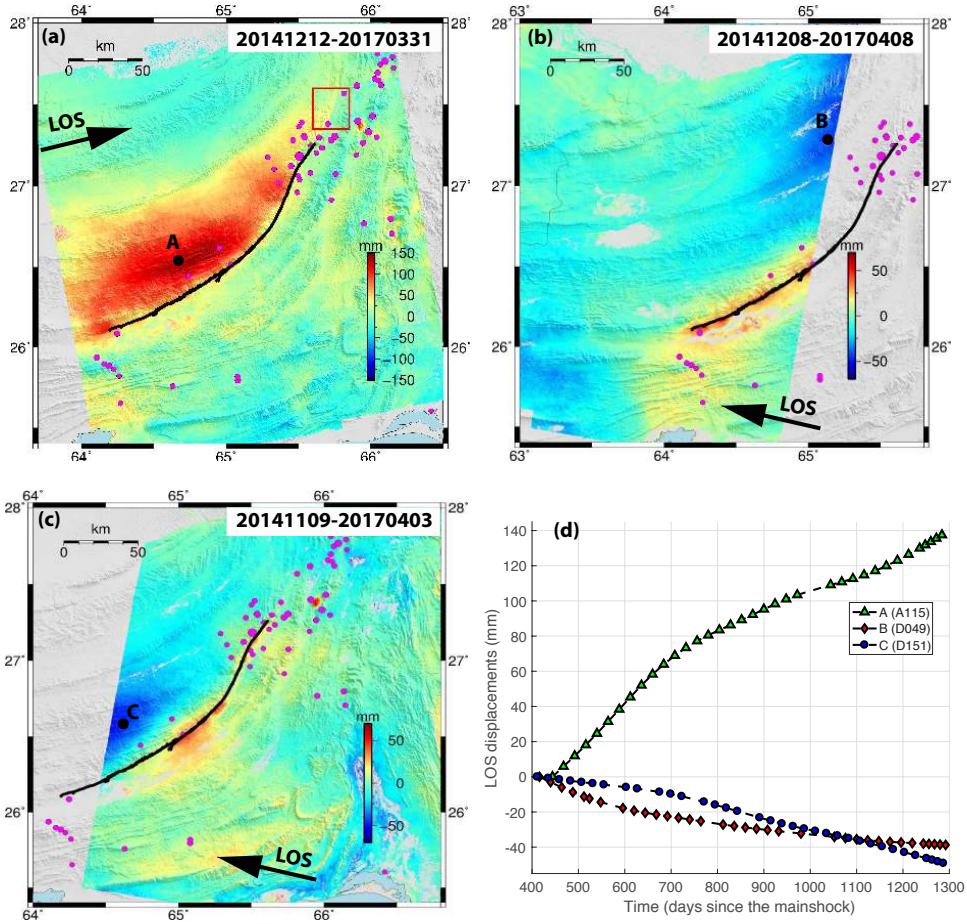

Figure 5.5: Cumulative postseismic InSAR LOS displacements due to the 2013 Balochistan earthquake. (a) LOS displacements along the ascending track A115. Rex box represents the area shown in Figure 5.12. (b) LOS displacements along the descending track D049. (c) LOS displacements along the descending track D115. The observation period for each track is indicated by the numbers at top-right corner of each panel. Arrow in each panel represents the direction of the line-of-sight of the corresponding track. (d) time series of the LOS displacements at selected points marked by A, B and C in panels of (a-c). Note that we excluded the first and last acquisition in the SBAS analysis.

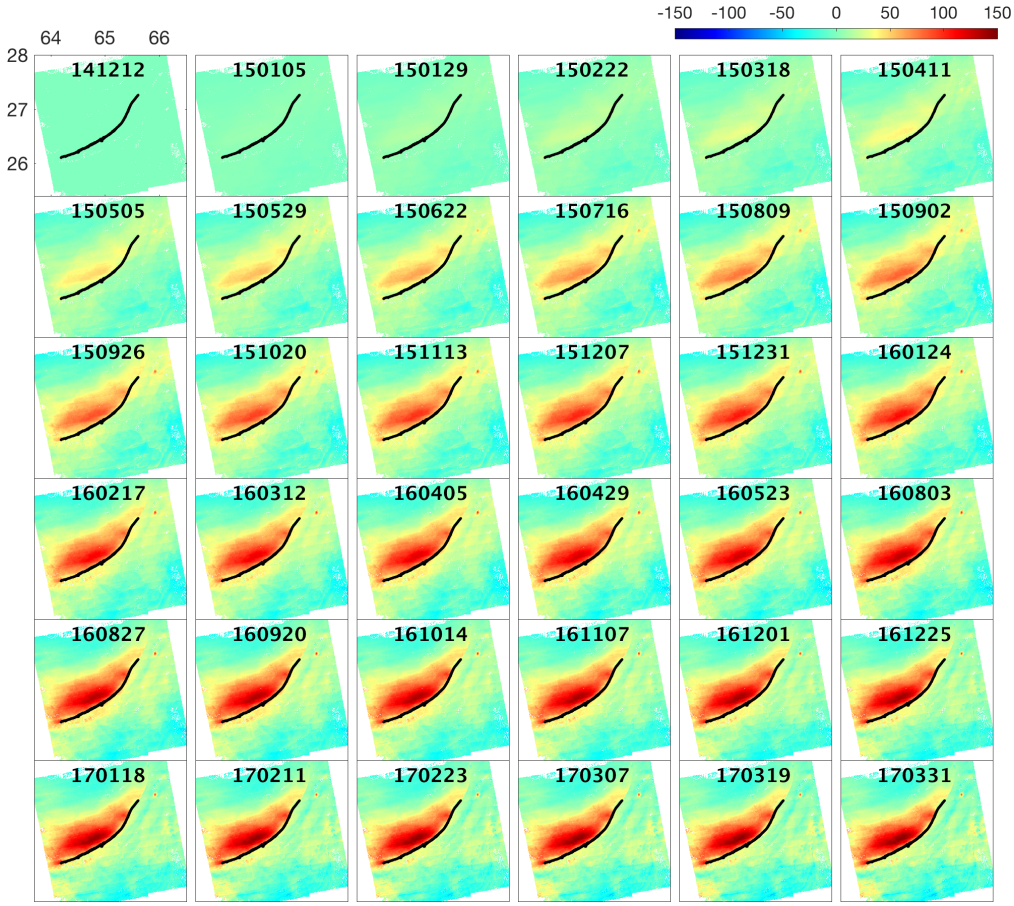

Figure 5.6: Time series of the postseismic displacements due to the 2013 Balochistan earthquake along the line-of-sight (LOS) direction of the ascending track A115. Positive LOS displacements correspond to the surface motion toward the satellite. Black curve denote the surface trace of 2013 Balochistan rupture. Numbers in each panel denote the dates of SAR image acquisitions. The units of the range change are in mm.

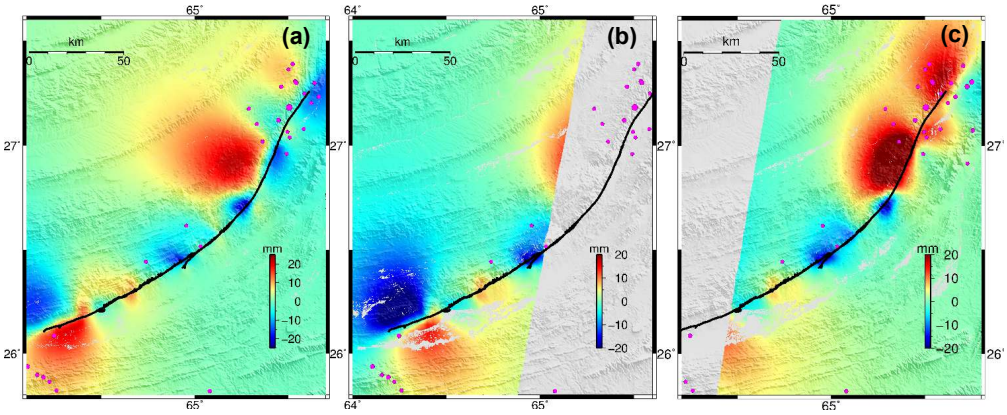

Figure 5.7: Model predicted InSAR LOS displacements due to the poroelastic rebound of the 2013 Balochistan earthquake. Panels (a-c) are for Sentinel-1A track A115, D049, D151, respectively.

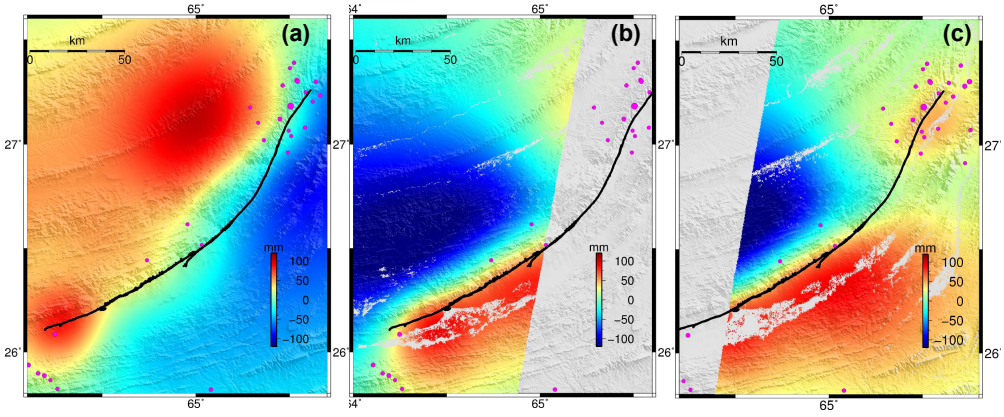

Figure 5.8: Model predicted LOS displacements due to the viscoelastic relaxation of the 2013 Balochistan earthquake during observation period of the respective InSAR tracks. The model has a 25 km thick elastic upper crust, underlain by the viscoelastic lower crust and upper mantle with a dynamic viscosity of 10^{18} Pas. The calculations was performed with PSGRN/PSCMP (*Wang et al.*, 2006).

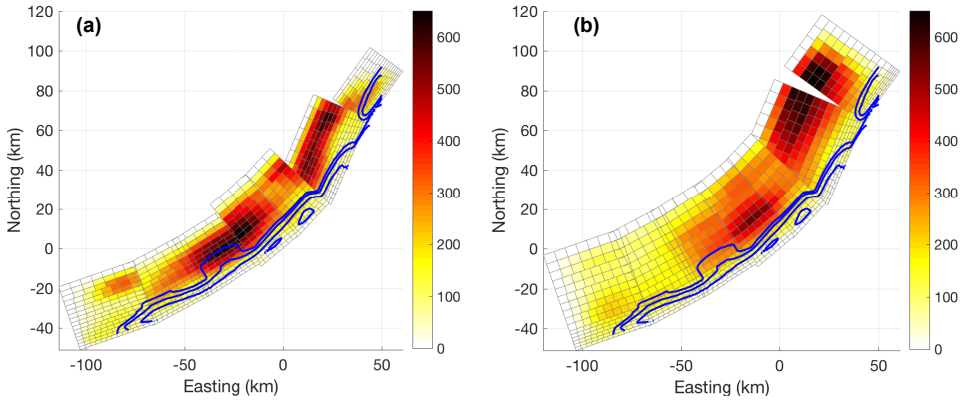

Figure 5.9: Kinematic inversions of the afterslip due to the 2013 Balochistan earthquake assuming that (a) the fault planes for afterslip have the same dip angles as the coseismic rupture; and (b) the faults in the Makran range are connected by a décollement with a dip angle of 15° at 15 km. Blue Line represent the coseismic slip contours at 2 m increments starting from 1m (*Avouac et al.*, 2014). Color represents the inverted afterslip in mm.

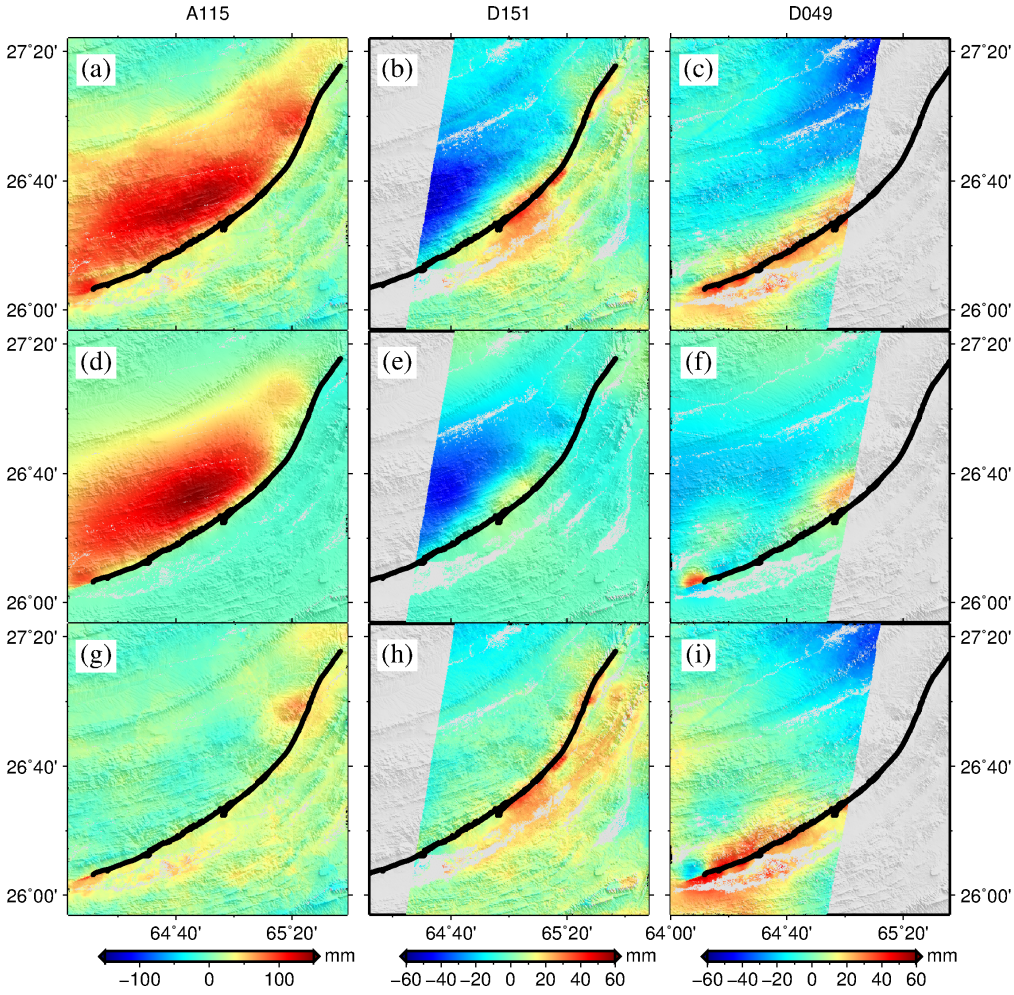

Figure 5.10: Comparison of the observed and modeled InSAR LOS displacements due to afterslip on planar faults. The forward calculation is based on the afterslip model of Figure 5.9a (model A). (a-c) Observations, (d-f) model predictions, and (g-i) residuals. Note that data from the descending track D049 were not used in the inversion, because of the relative poor signal-to-noise (SNR) ratio.

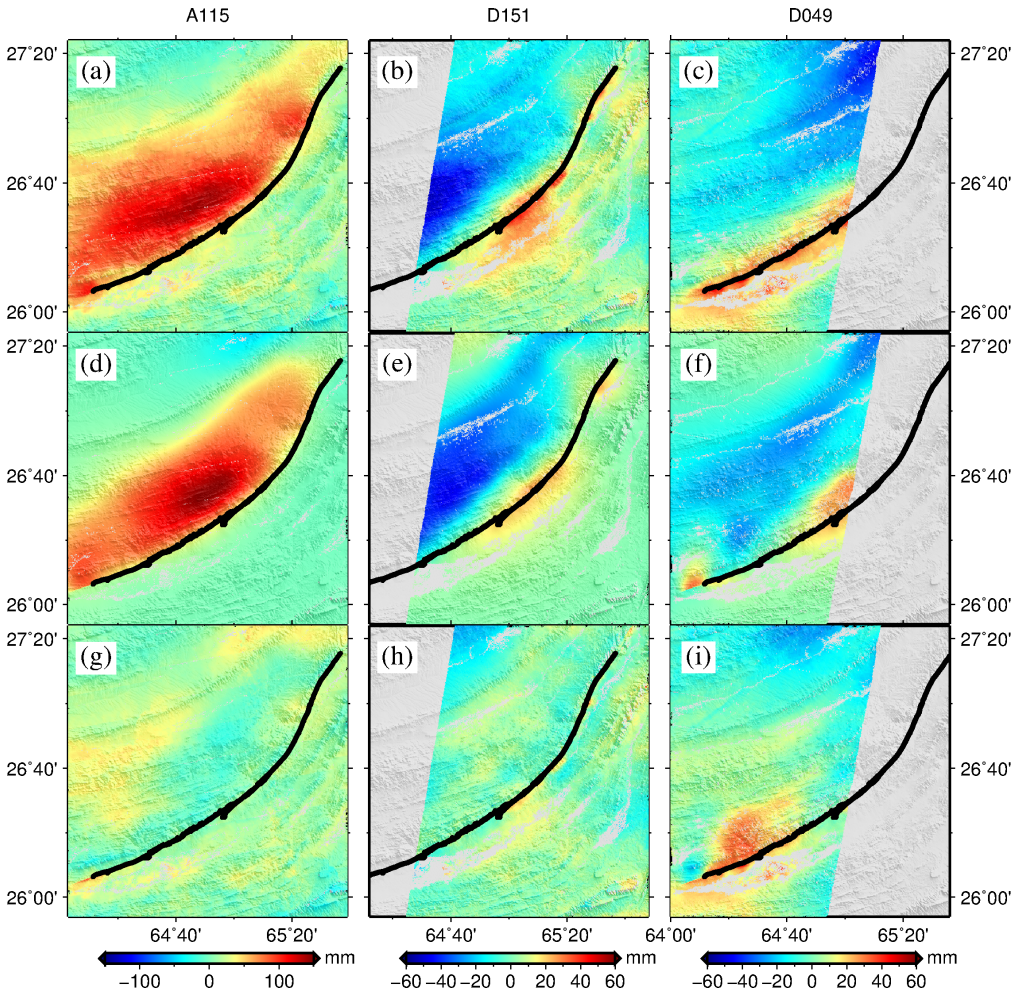

Figure 5.11: Comparison of the observed and modeled InSAR LOS displacements due to afterslip on fault planes connecting to a décollement at 15 km. The forward calculation is based on the afterslip model of Figure 5.9b (model B). (a-c) Observations, (d-f) model predictions, and (g-i) residuals. Note that data from the descending track D049 were not used in the inversion, because of the relative poor signal-to-noise (SNR) ratio.

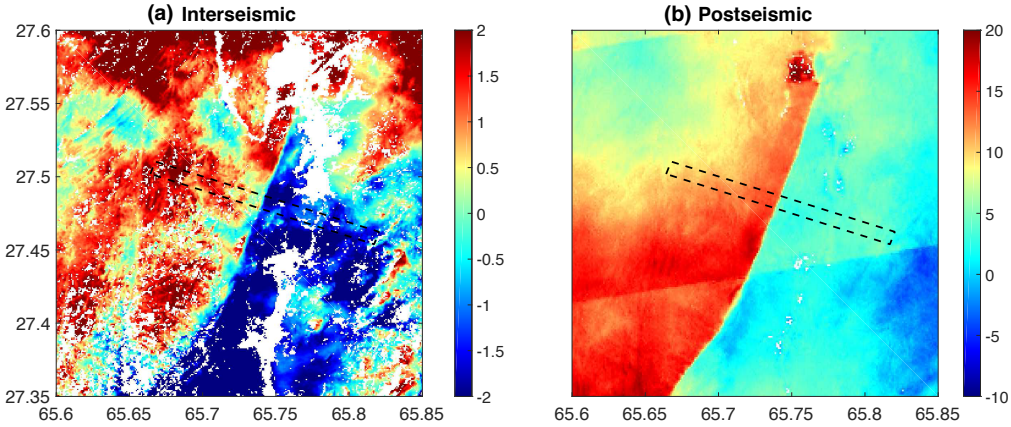

Figure 5.12: Surface creep along the North-East continuation of the 2013 Balochistan rupture revealed by InSAR observations. (a) Interseismic LOS velocity map derived from the Envisat ASAR data from 2004-2010. (b) Average LOS velocity map derived from the Sentinel-1A data from December 2014 to April, 2017. Dashed black box denotes a profile shown in Figure 5.13. The units of the LOS velocities are mm/yr.

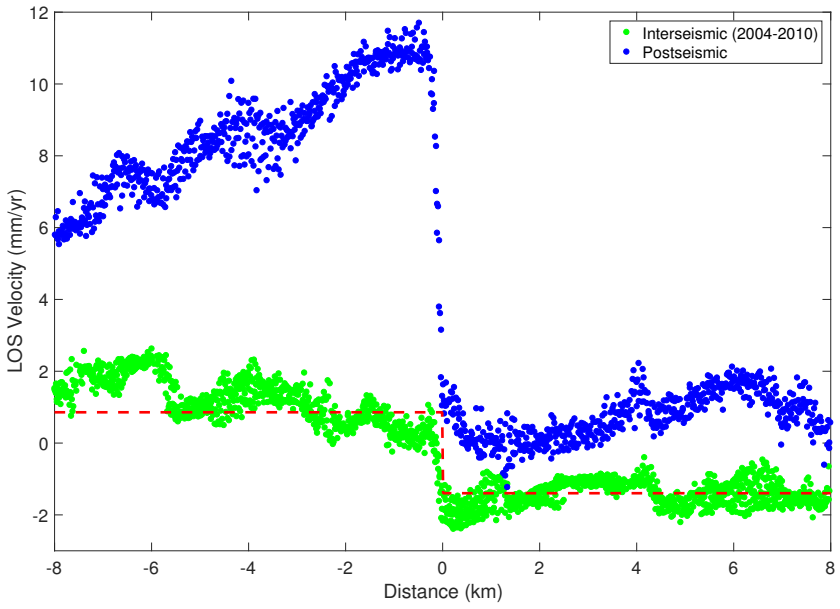

Figure 5.13: Interseismic and postseismic InSAR LOS velocities along a profile perpendicular to the surface creep north of the 2013 Balochistan rupture. Postseismic LOS velocities are for the ascending Sentinel-1A track A115 (Figure 5.5a). Red dash line denotes the best-fitting step function with an offset of 2.1 mm/yr across the fault.

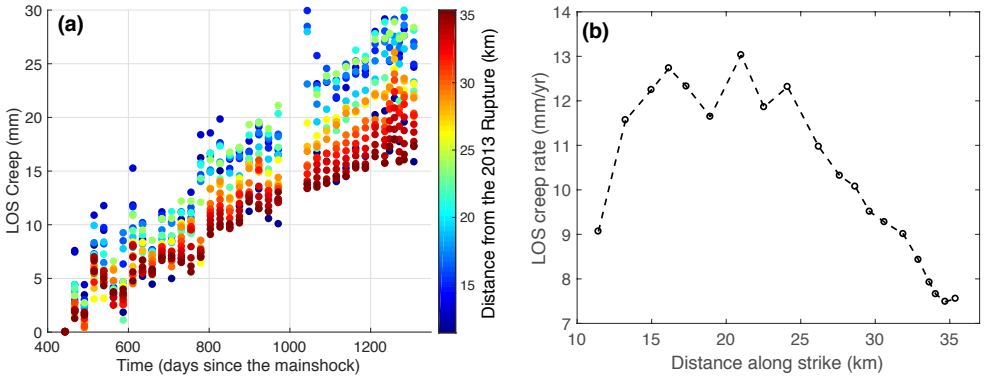

Figure 5.14: Spatiotemporal variations of the postseismic surface creep along the fault segment north of the 2013 Balochistan earthquake. (a) time series of the relative LOS displacements across the fault trace. Color represents the distance of the creep location from the northern tip of the 2013 Balochistan earthquake. (b) average LOS creep rate as a function of distance from the 2013 Balochistan rupture.

Bibliography

Ambraseys, N., and R. Bilham (2003), Earthquakes and associated deformation in northern baluchistan 1892-2001, *Bulletin of the Seismological Society of America*, *93*(4), 1573–1605.

Avouac, J.-P., F. Ayoub, S. Wei, J.-P. Ampuero, L. Meng, S. Leprince, R. Jolivet, Z. Duputel, and D. Helmberger (2014), The 2013, Mw 7.7 Balochistan earthquake, energetic strike-slip reactivation of a thrust fault, *Earth and Planetary Science Letters*, *391*, 128–134.

Barbot, S., Y. Hamiel, and Y. Fialko (2008), Space geodetic investigation of the coseismic and postseismic deformation due to the 2003 Mw 7. 2 Altai earthquake: Implications for the local lithospheric rheology, *Journal of Geophysical Research: Solid Earth*, *113*(B3).

Barnhart, W. D., G. P. Hayes, R. W. Briggs, R. D. Gold, and R. Bilham (2014), Ball-and-socket tectonic rotation during the 2013 M(w) 7.7 Balochistan earthquake, *Earth and Planetary Science Letters*, *403*, 210–216.

Barnhart, W. D., R. W. Briggs, N. G. Reitman, R. D. Gold, and G. P. Hayes (2015), Evidence for slip partitioning and bimodal slip behavior on a single fault: Surface slip characteristics of the 2013 Mw 7.7 Balochistan, Pakistan earthquake, *Earth and Planetary Science Letters*, *420*, 1–11.

Berardino, P., G. Fornaro, R. Lanari, and E. Sansosti (2002), A new algorithm for surface deformation monitoring based on small baseline differential SAR interferograms, *IEEE Transactions on Geoscience and Remote Sensing*, *40*(11), 2375–2383.

Chen, C. W., and H. A. Zebker (2002), Phase unwrapping for large sar interferograms: Statistical segmentation and generalized network models, *IEEE Transactions on Geoscience and Remote Sensing*, *40*(8), 1709–1719.

Ding, X., Z. Li, J. Zhu, G. Feng, and J. Long (2008), Atmospheric effects on InSAR measurements and their mitigation, *Sensors*, *8*(9), 5426–5448.

Fattahi, H., and F. Amelung (2016), InSAR observations of strain accumulation and fault creep along the Chaman Fault system, Pakistan and Afghanistan, *Geophysical Research Letters*, *43*(16), 8399–8406.

Frohling, E., and W. Szeliga (2016), GPS constraints on interplate locking within the Makran subduction zone, *Geophysical Journal International*, *205*(1), 67–76.

Hu, Y., K. Wang, J. He, J. Klotz, and G. Khazaradze (2004), Three-dimensional viscoelastic finite element model for postseismic deformation of the great 1960 Chile earthquake, *Journal of Geophysical Research: Solid Earth*, *109*(B12).

Jolivet, R., Z. Duputel, B. Riel, M. Simons, L. Rivera, S. E. Minson, H. Zhang, M. A. G. Aivazis, F. Ayoub, S. Leprince, S. Samsonov, M. Motagh, and E. J. Fielding (2014), The 2013 Mw 7.7 Balochistan Earthquake: Seismic Potential of an Accretionary Wedge, *Bulletin of the Seismological Society of America*, *104*(2), 1020–1030.

Kaneko, Y., J.-P. Avouac, and N. Lapusta (2010), Towards inferring earthquake patterns from geodetic observations of interseismic coupling, *Nature Geoscience*, *3*(5), 363.

Lapusta, N., and Y. Liu (2009), Three-dimensional boundary integral modeling of spontaneous earthquake sequences and aseismic slip, *Journal of Geophysical Research: Solid Earth*, *114*(B9).

Lawrence, R., R. Yeats, S. Khan, A. Farah, and K. DeJong (1981), Thrust and strike slip fault interaction along the chaman transform zone, Pakistan, *Geological Society, London, Special Publications*, *9*(1), 363–370.

Mohadjer, Solmaz, Ehlers, Todd Alan, Bendick, Rebecca, Stübner, Konstanze, and Strube, Timo (2016), A Quaternary fault database for central Asia, *Natural Hazards and Earth System Sciences*, *16*(2), 529–542.

Okada, Y. (1985), Surface deformation due to shear and tensile faults in a half-space, *Bulletin of the Seismological Society of America*, *75*(4), 1135–1154.

Penney, C., F. Tavakoli, A. Saadat, H. R. Nankali, M. Sedighi, F. Khorrami, F. Sobouti, Z. Rafi, A. Copley, J. Jackson, and K. Priestley (2017), Megathrust and accretionary wedge properties and behaviour in the Makran subduction zone, *Geophysical Journal International*, *209*(3), 1800–1830.

Schmidt, D. A., and R. Bürgmann (2003), Time-dependent land uplift and subsidence in the Santa Clara valley, California, from a large interferometric synthetic aperture radar data set, *Journal of Geophysical Research: Solid Earth (1978–2012)*, *108*(B9), 1985.

Smith, G., L. McNeill, T. J. Henstock, and J. Bull (2012), The structure and fault activity of the Makran accretionary prism, *Journal of Geophysical Research: Solid Earth*, *117*(B7).

Szeliga, W., R. Bilham, D. M. Kakar, and S. H. Lodi (2012), Interseismic strain accumulation along the western boundary of the Indian subcontinent, *Journal of Geophysical Research: Solid Earth*, *117*(B8).

Tong, X., and D. Schmidt (2016), Active movement of the Cascade landslide complex in Washington from a coherence-based InSAR time series method, *Remote Sensing of Environment*, *186*, 405–415.

Tymofyeyeva, E., and Y. Fialko (2015), Mitigation of atmospheric phase delays in insar data, with application to the eastern California shear zone, *Journal of Geophysical Research: Solid Earth*, *120*(8), 5952–5963.

Ul-Hadi, S., S. D. Khan, L. A. Owen, A. S. Khan, K. A. Hedrick, and M. W. Caffee (2013), Slip-rates along the Chaman fault: Implication for transient strain accumulation and strain partitioning along the western Indian plate margin, *Tectonophysics*, *608*, 389–400.

Vallage, A., Y. Klinger, R. Grandin, H. S. Bhat, and M. Pierrot-Deseilligny (2015), Inelastic surface deformation during the 2013 Mw 7.7 Balochistan, Pakistan, earthquake, *Geology*, *43*(12), 1079–1082.

Vallage, A., Y. Klinger, R. Lacassin, A. Delorme, and M. Pierrot-Deseilligny (2016), Geological structures control on earthquake ruptures: The Mw 7.7, 2013, Balochistan earthquake, Pakistan, *Geophysical Research Letters*, *43*(19), 10,155–10,163.

Wang, K., and Y. Fialko (2014), Space geodetic observations and models of post-seismic deformation due to the 2005 M7.6 Kashmir (Pakistan) earthquake, *Journal of Geophysical Research: Solid Earth*, *119*(9), 7306–7318.

Wang, K., and Y. Fialko (2015), Slip model of the 2015 Mw 7.8 Gorkha (Nepal) earthquake from inversions of ALOS-2 and GPS data, *Geophysical Research Letters*, *42*(18), 7452–7458.

Wang, K., and Y. Fialko (2017), Observations and modeling of co- and post-seismic deformation due to the 2015 mw 7.8 Gorkha (Nepal) earthquake, *Journal of Geophysical Research: Solid Earth*, in revision.

Wang, K., Y. Hu, and J. He (2012), Deformation cycles of subduction earthquakes in a viscoelastic earth, *Nature*, *484*(7394), 327.

Wang, R., F. L. Martın, and F. Roth (2003), Computation of deformation induced by earthquakes in a multi-layered elastic crust–FOTRAN programs EDGRN/EDCMP, *Computers & Geosciences*, *29*(2), 195–207.

Wang, R., F. Lorenzo-Martín, and F. Roth (2006), PSGRN/PSCMP–a new code for calculating co-and post-seismic deformation, geoid and gravity changes based on the viscoelastic-gravitational dislocation theory, *Computers & Geosciences*, *32*(4), 527–541.

Xu, X., D. T. Sandwell, E. Tymofyeyeva, A. González-Ortega, and X. Tong (2017), Tectonic and anthropogenic deformation at the Cerro Prieto geothermal step-over revealed by Sentinel-1A InSAR, *IEEE Transactions on Geoscience and Remote Sensing*.

Chapter 6

Improving Burst Alignment in TOPS Interferometry with Bivariate Enhanced Spectral Diversity (BESD)

Abstract

TOPS-mode SAR interferometry requires high accuracy of burst alignments. Geometrical burst alignment relying on precise orbits and digital topography is not always sufficient for Sentinel-1A TOPS mode Interferometry. Enhanced spectral diversity (ESD) method was proposed to estimate a constant azimuth shift between radar images that minimizes phase discontinuities across the bursts.

In some cases however the ESD refinement fails to align the bursts in Sentinel-1 interferograms, possibly because of ionospheric propagation effects. Here we show that in such cases a bivariate shift (that depends on both azimuth and range) can efficiently remove phase discontinuities across the bursts. The bivariate shift can be derived from the double-differenced radar phase in the burst overlap regions.

6.1 Introduction

Several recently launched Synthetic Aperture Radar (SAR) missions, including TerraSAR-X and Sentinel-1, employ Terrain Observation by Progressive Scans (TOPS) mode (*De Zan and Guarnieri*, 2006). In the TOPS mode SAR system, the antenna is rotated from backward to forward-looking direction during the burst acquisition (opposite to the antenna rotation in case of the SPOT-mode SAR system). While this approach improves the image quality both in terms of amplitude (decreased 'scallopin' effect) and phase (reduced azimuth ambiguity), the fast steering of antenna along azimuth direction causes large variations of the Doppler centroid within a burst (*De Zan and Guarnieri*, 2006). It is well known that in the presence of a squint, linear phase ramps are introduced in the focused response both in azimuth and range, although ramps in the range direction are mostly negligible. To form interferograms of coherent phase, the reference and repeat images have to be aligned accurately. However, because the orbital velocities or burst timing of the reference and repeat acquisitions may be different, a

small misalignment of bursts in the azimuth direction could be expected. As the difference in the Doppler centroids at the upper and lower edges of each burst is usually much larger than the pulse repetition frequency (PRF), a small azimuthal misalignment could result in a significant phase jump in the interferogram at the burst boundaries. The relationship between the burst misalignment Δa and the resulting phase jump ϕ at the burst boundaries is:

$$\Delta a = PRF \frac{\phi}{2\pi \Delta f} \tag{6.1}$$

where Δf denotes the Doppler centroid variation caused by steering of the antenna from backward-looking to forward-looking within one burst (*Grandin et al.*, 2016; *Prats-Iraola et al.*, 2012). For example, for the C-band Sentinel-1 mission, the Doppler centroid variation within one burst is ∼4500 Hz, and the effective PRF is 486 Hz. Therefore to keep phase jumps to be smaller than 1/10 of a phase cycle (corresponding to 2.8 mm along the radar line of sight) at the burst boundaries, the burst alignment between reference and repeat acquisitions has to be at the accuracy of 0.01 pixel size in the azimuth direction. The traditional cross-correlation method used in the stripmap mode SAR interferometry is not sufficient for this purpose. With the information on SAR system's internal geometry, satellite's orbits and external Digital Elevation Model (DEM), one can precisely map the footprint of each image acquisition on the ground. Differencing the ground footprints provides an offset map needed for the image alignment. This method is often referred to as 'geometrical alignment'. The accuracy of the geometrical

alignment largely depends on the accuracy of satellite orbits. For the Sentinel-1 mission, the accuracy of the post-processed orbit is ∼5cm along-track and ∼2-3 cm radially and cross-track (*Fernández et al.*, 2015), i.e., on the order of 1% of the pixel size. While the geometrical alignment should in theory be sufficient for Sentinel-1 interferometry, in practice phase discontinuities between the bursts often persist.

The burst alignment can be improved by taking advantage of the fact that small overlapping regions between consecutive bursts are imaged twice from two slightly different view directions (forward-looking and backward-looking). Similar to the along-track interferogram or MAI (multi-aperture interferogram) in stripmap interferometry (e.g. *Barbot et al.*, 2008; *Bechor and Zebker*, 2006; *Jung et al.*, 2013), a double-difference interferogram can be generated for pixels within the burst overlap regions. The double differenced phase is proportional to the azimuth shift of pixels between image acquisitions. Provided the ground motion along the satellite track is negligible between image acquisitions, the double-differenced phase of pixels in the burst overlap areas can be used to correct burst misalignment that might result from a clock drift, imprecise knowledge of satellite orbits or other unmodeled sources causing the along-track pixel shift. This method is known as Enhanced Spectral Diversity (ESD) (e.g. *Prats-Iraola et al.*, 2012) and is used in a number of data processing packages. SAR processors that use the ESD method to correct for the geometrical alignment use either median or mean values of the double-differenced phase within the burst overlap regions to estimate a constant

shift in the azimuth direction. A few recent studies have attempted to use azimuth-dependent shift to correct for the geometrical misalignment (*Scheiber et al.*, 2015; *Xu et al.*, 2016). Here we present examples of Sentinel-1A data that exhibit strong variations in the double-differenced phase in both range and azimuth directions. In such cases, corrections of burst alignments assuming a constant azimuth shift cannot completely remove artificial phase jumps at burst boundaries. We show that bivariate (azimuth- and range-dependent) azimuth shifts are necessary to produce accurate burst alignment in TOPS mode SAR interferometry.

6.2 Data processing

The data used in this study are interferometric wide-swath (IW) TOPS mode single look complexes (SLCs) of Sentinel-1A mission, downloaded from Alaska Satellite Facility (ASF). We processed the data with the latest (v5.2) version of GMT5SAR (*Xu et al.*, 2017). We first geometrically aligned the reference (master) and repeat (slave) images using the post-processed precise orbit ephemerides and SRTM V3 3arcsec DEM data. The double-differenced interferogram within the burst overlap regions was then calculated as follows:

$$\phi = \arg[(c_{11} \times c_{12}^*) \times (c_{21} \times c_{22}^*)^*] \tag{6.2}$$

where the first and second subscript of each variable represents the view geometry and acquisition, respectively, and * symbol represents the conjugate of a complex number. For instance, c_{22}^* denotes the conjugate of the complex numbers corre-

sponding to forward-looking view in the second acquisition. We then calculated the azimuth shift of the burst overlap pixels using equation 6.1. Since the width of a burst overlap between two consecutive bursts is only about 1/10 of the width of a burst itself, interpolation is needed to fill gaps between the bursts. To increase the signal-to-noise ratio, we applied a 40 by 10 block median filter to the original double-differenced phase in the burst overlap regions before interpolation. We used a Laplacian operator to smooth the interpolation results. The degree of smoothing affects the final refinement of burst alignments. A weaker smoothing results in a better alignment. A stronger smoothing is more efficient at suppressing noise in the double-differenced phase that may give rise to spurious azimuth offsets. We tested a range of the smoothing parameters and chose an optimal value such that the interpolated azimuth shift map is sufficiently smooth on scales of 20 km or below, while the phase jumps across burst boundaries did not exceed 0.05 rad on average. The azimuth shift table after interpolation was then added to the shift table from geometrical alignment to refine the burst alignment.

6.3 Examples

Here we present an example to illustrate how the burst alignment can be improved with Bivariate (range-and-azimuth dependent) Enhanced Spectral Diversity (BESD) method. For Sentinel 1 mission, each scene contains 3 sub-swaths and each sub-swath typically has 9 bursts. For the sake of brevity and simplicity,

in the example below we only show a sub-swath with largest phase discontinuities across burst boundaries after geometrical alignment. The Sentinel-1A scene IDs for the two SAR images are:

`S1A_IW_SLC__1SSV_20151222T100036_20151222T100104_009153_00D2C0_506F`

`S1A_IW_SLC__1SSV_20160115T100035_20160115T100103_009503_00DCC1_C03E`

The images cover an area in South America near the boarder of Chile, Bolivia and Argentina. The area is characterized by high correlation of the radar phase due to an arid sparsely vegetated environment (*Fialko and Pearse*, 2012). Figure 6.1 shows the double-differenced phase for the burst overlaps pixels and its statistics (mean and median values). An obvious feature of the double-differenced interferogram in this example is a strong variation of the azimuth shift in both range and azimuth directions. The azimuth shift varies continuously from -0.015 to 0.015 across the swath, with median and mean values of -0.0026 and 0.0019, respectively (Figure 6.1). Correspondingly, an interferogram with the geometrical burst alignment shows phase discontinuities across most of the burst boundaries (Figure 6.2a). To quantify phase jumps at burst boundaries, we computed an average phase gradient in the azimuth direction $d\phi$ as:

$$d\phi_j = \frac{1}{N}\sum_{i=1}^{N}[\phi(i, j+1) - \phi(i, j)] \tag{6.3}$$

where ϕ denotes the unwrapped radar phase, indexes i and j denote pixel coordinates in range and azimuth, respectively, and N is the number of pixels in the range direction. The interferogram with no correction (Figure 6.2a) has an aver-

age phase jump of >0.1 rad across most of the bursts (note that this value is the average phase jump along the range direction, and the local phase discontinuities across certain burst boundaries could be much higher than this value). The ESD corrections with the median and mean values of the azimuth shift from the double-difference interferogram do not appreciably reduce phase jumps between the bursts. The correction using a bivariate shift (BESD) shown in Figure 6.1c, on the other hand, efficiently removes the phase discontinuities for the entire interferogram.

6.4 Discussion

Strong variations of the azimuth shift along both range and azimuth directions suggest that such variations are unlikely due to clock errors or imprecise knowledge of satellite orbits. This is because clock and orbital errors might introduce variations in the azimuth shift that are chiefly azimuth-dependent. In addition, if the burst misalignment were due to the clock drift or orbital errors, the double differenced interferograms or equivalent azimuth shift maps of all three sub-swaths would be expected to have nearly identical patterns of the azimuth dependence, as all sub-swaths are acquired from the same trajectory and at nearly the same time. To examine the pattern of the azimuth shift across different sub-swaths, we formed double difference interferograms separately for each sub-swatch of the SAR scenes used in example above. The combined double differenced phase and inferred azimuth shift for all 3 sub-swaths are shown in Figure 6.3. Both the

original double differenced phase in the burst overlap regions (Figure 6.3) and the interpolated azimuth shift (Figure 6.3b) show remarkable consistency and continuity across the sub-swath boundaries. The azimuth shift variations in the third sub-swath are on average much stronger than those in the first sub-swath, and are dominated by 'ridges' and 'troughs' that are oblique to the azimuth direction. Using the combined azimuth shift map (Figure 6.3b) to correct for the burst alignment, one obtains an interferogram with a continuous radar phase across both the burst and sub-swath boundaries (Figure 6.4).

Features seen in the azimuth shift map in Figure 6.3b are very similar to the 'azimuth streaks' caused by ionospheric perturbations in SAR interferograms, particularly for L-band (e.g. *Raucoules and De Michele*, 2010). The effect of ionosphere on the interferometric phase depends on the radar wavelength and the total electron content (TEC) gradient along the satellite's flight direction. For SAR interferometry, apparent azimuth shift may occur if the azimuth gradients of TEC are different at the times of image acquisition. The azimuth shift caused by ionosphere perturbations is proportional to the difference of TEC gradients along the azimuth direction. Several studies have used this relationship to correct for the ionospheric effects in L-band SAR interferometry (e.g. *Jung et al.*, 2013; *Liu et al.*, 2014) The effect of ionospheric perturbations on C-band interferometry is expected to be much weaker than that of L-band, as the ionospheric phase delay is inversely proportional to the square of the radar carrier wave's frequency. Azimuth streaks, however, do occasionally occur in ERS, ENVISAT and RADARSAT interferograms

(*Gray et al.*, 2000). Recent studies show that the ionospheric effect on Sentinel-1 interferometry can be significant indeed (*Gomba et al.*, 2017). Various ways have been proposed to reduce ionospheric errors in InSAR measurements, including the range spectrum-split method (*Gomba et al.*, 2017) and common-point-stacking (*Tymofyeyeva and Fialko*, 2015). If variations in the azimuth shift documented in this study (Figure 6.3) are indeed due to ionospheric effects, the method proposed in this paper could be used to study the TEC variations at high spatial resolution.

It is possible that interpolation may introduce some artifacts to the phase of pixels outside of the burst overlaps. However, given that the Doppler frequency variation within a burst is small between two adjacent radar pulses, the phase error due to the interpolation of azimuth shift should be small in the non-overlapping areas. Particularly, if the bivariate azimuth shift seen in the double-difference interferogram is indeed due to TEC (Total Electron Content) gradients along the satellite flying path, the interpolation from burst overlaps to the rest of the image should be robust, as the dominant power of ionospheric phase delay usually lies at relatively large wavelengths (e.g. > 50 km). At the top and bottom edges of the azimuth shift map, where the double-differenced phase is essentially extrapolated beyond the available burst overlaps (e.g., Figure 6.1c), the artifacts due to interpolation could be more pronounced. Such artifacts can be reduced by using longer radar swaths and/or trimming interferograms to exclude areas beyond the burst overlaps. Similar to conventional interferograms, an increase in temporal and geometrical baseline could deteriorate the phase correlation of a double-differenced

interferogram, making the estimation of the azimuth shift less accurate. One way to mitigate this problem is to first estimate the azimuth shift maps only for interferograms with short temporal and geometric baselines and then solve for the time series of the azimuth shifts relative to a reference acquisition (NESD) (*Fattahi et al.*, 2017).

In case of non-negligible surface displacements along the satellite track, the proposed method is not well suited for minimizing phase discontinuities between the bursts, as contributions of surface displacements to the azimuth shift can trade off with ionospheric effects and instrument/platform-related artifacts (clock drift, orbit errors, etc.). For the same reason, the along-track interferograms obtained from interpolation of the double-differenced phase in the burst overlap areas are unlikely to be useful for measuring a low-amplitude large-wavelength along-track component of ground motion (e.g., due to interseismic deformation), despite a high theoretical accuracy of the ESD method. The along-track interferograms can provide important constraints on surface displacements that greatly exceed possible contributions from the ionosphere and/or instrument/platform artifacts (e.g., in case of large earthquakes, landslides, flow of ice etc.), complementing measurements of range changes based on conventional interferometry.

6.5 Conclusions

TOPS mode SAR interferometry requires high accuracy of burst alignments. Misalignment of bursts causes phase jumps at the burst boundaries. Geometrical burst alignment relying on precise orbits and external DEM appears sufficient for Sentinel-1A TOPS mode interferometry in many cases. However, in many other cases geometrical alignment is insufficient to remove phase discontinuities across burst boundaries. The Enhanced Spectral Diversity (ESD) method was proposed to mitigate this problem. Here we present examples of Sentinel-1 TOPS interferograms in which neither geometrical alignment nor the ESD refinement are sufficient to remove phase discontinuities between the bursts. We propose a modification of the ESD method, named Bivariate Enhanced Spectral Diversity (BESD) that relaxes the assumption of a constant azimuth shift and estimates a point-by-point azimuth shift map that varies in both range and azimuth. We demonstrate that the BESD method is able to produce TOPS interferograms without artificial phase discontinuities. Variations in the azimuth shift in range and azimuth directions cannot be explained by clock drift or orbital errors, but may result from ionospheric perturbations during SAR acquisitions.

Acknowledgement

We thank two anonymous reviewers for their comments. This work was supported by NASA (grant NNX14AQ15G). Sentinel-1 data are provided by the

European Space Agency (ESA) through Alaska Satellite Facility (ASF) and UNAVCO. SAR data processing was performed on the Comet cluster at the San Diego Supercomputing Center (SDSC). Processed data and software used in this study are available from the authors.

This chapter, in full, is a preprint of the material submitted to the *IEEE Geoscience and Remote Sensing Letters* as: Wang, K., X. Xu and Y. Fialko, "Improving Burst Alignment in TOPS Interferometry with Bivariate Enhanced Spectral Diversity (BESD)". The author of this dissertation is the primary investigator of work presented in this chapter.

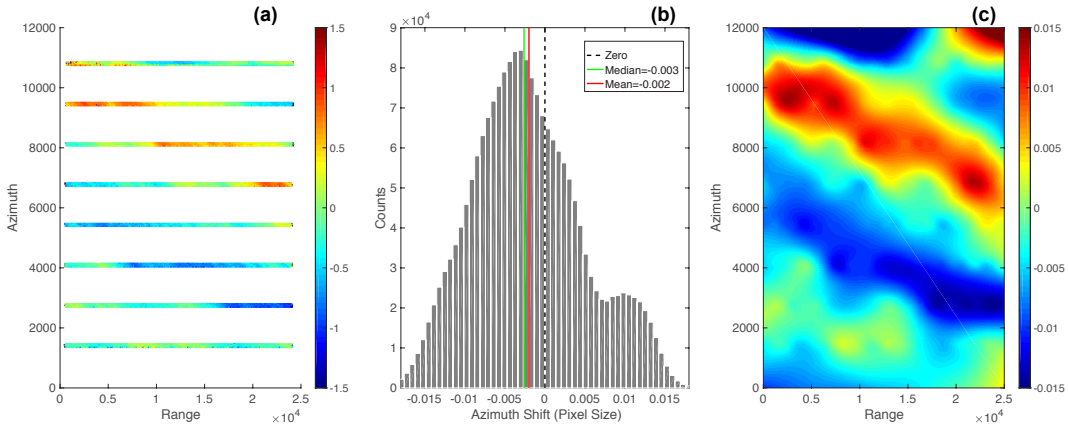

Figure 6.1: (a) double differenced phase in the burst overlaps. (b) histogram of azimuth shift for burst overlaps. (c) interpolated azimuth shift map derived from the double-differenced phase from the burst overlap regions.

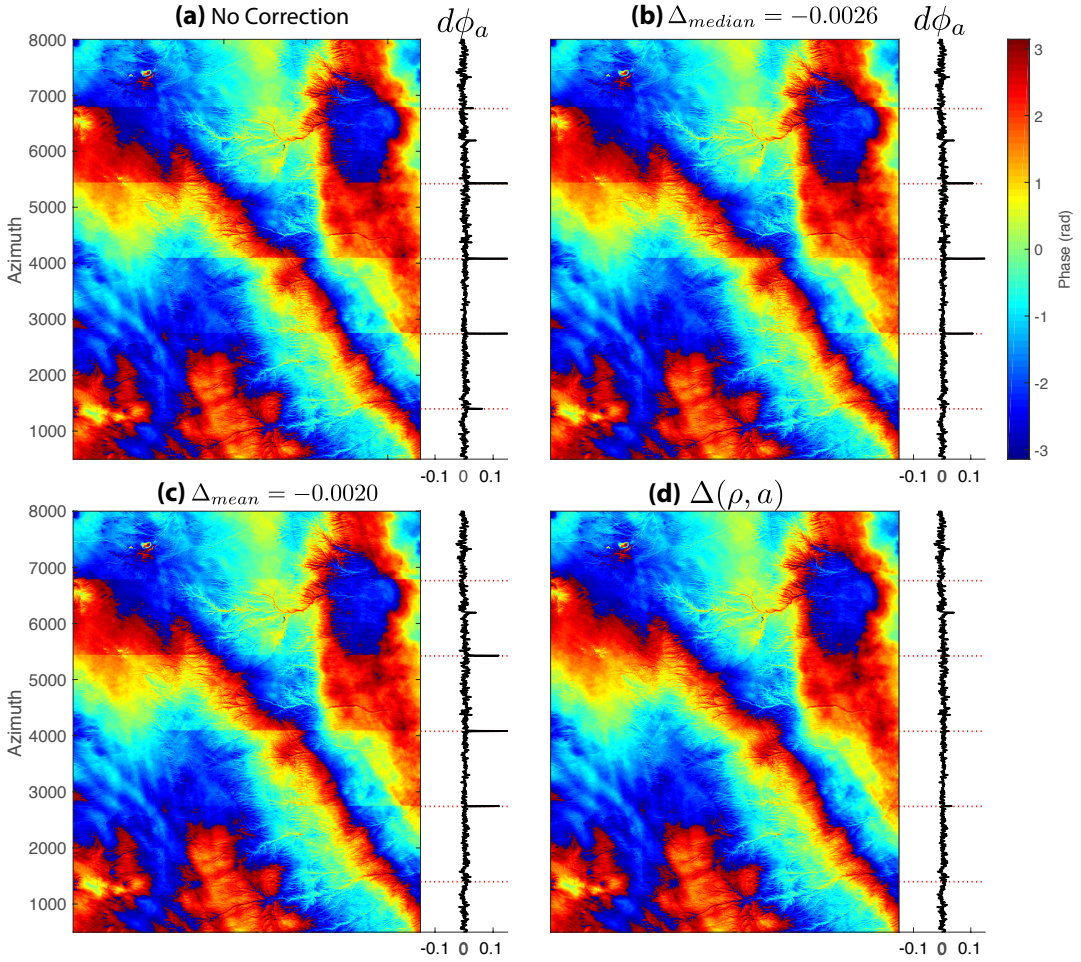

Figure 6.2: (a) geometrical alignment only. (b) correction with median value of the azimuth shift derived using the ESD method. (c) correction with mean value of the azimuth shift derived using the ESD method. (d) correction with range-and-azimuth variable azimuth shift derived using the BESD method. The black profile to the right of each interferogram represents the average phase gradient along azimuth direction. Phase discontinuities are manifested by spikes in the phase gradient. The red dotted lines denote the locations of burst boundaries.

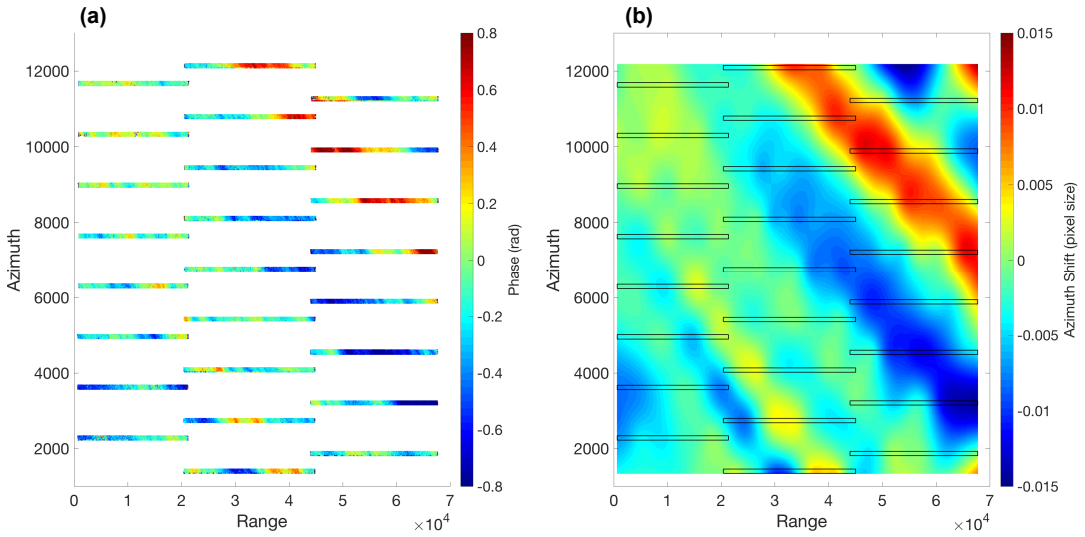

Figure 6.3: (a) double differenced phase in the burst overlap areas of all 3 sub-swaths. (b) interpolated azimuth shift map derived from data shown in Figure 6.3a. The back rectangles denote the bursts overlaps.

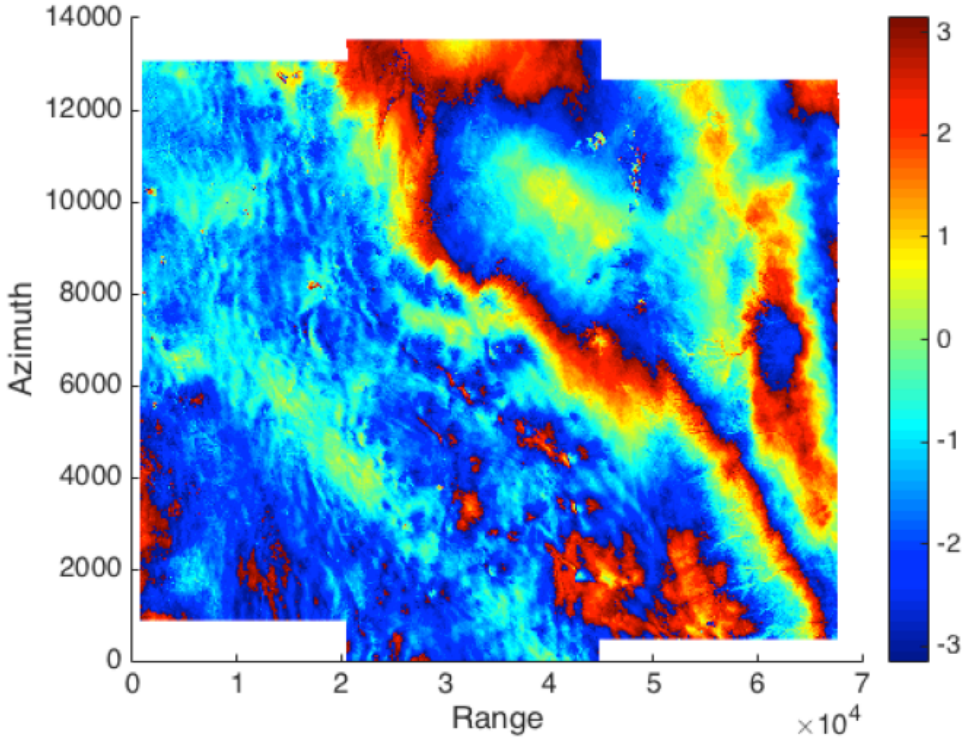

Figure 6.4: Interferometric phase for all 3 sub-swaths obtained using the refined burst alignment by the BESD method.

Bibliography

Barbot, S., Y. Hamiel, and Y. Fialko (2008), Space geodetic investigation of the coseismic and postseismic deformation due to the 2003 Mw 7. 2 Altai earthquake: Implications for the local lithospheric rheology, *Journal of Geophysical Research: Solid Earth*, *113*(B3).

Bechor, N. B., and H. A. Zebker (2006), Measuring two-dimensional movements using a single InSAR pair, *Geophysical Research Letters*, *33*(16).

De Zan, F., and A. M. Guarnieri (2006), TOPSAR: Terrain observation by progressive scans, *IEEE Transactions on Geoscience and Remote Sensing*, *44*(9), 2352–2360.

Fattahi, H., P. Agram, and M. Simons (2017), A network-based enhanced spectral diversity approach for tops time-series analysis, *IEEE Transactions on Geoscience and Remote Sensing*, *55*(2), 777–786.

Fernández, J., D. Escobar, H. Peter, and P. Féménias (2015), Copernicus pod service operations -orbital accuracy of Sentinel-1A and Sentinel-2B, in *International Symposium on Space Flight Dynamics*.

Fialko, Y., and J. Pearse (2012), Sombrero uplift above the Altiplano-Puna magma body: Evidence of a ballooning mid-crustal diapir, *Science*, *338*(6104), 250–252.

Gomba, G., F. R. González, and F. De Zan (2017), Ionospheric phase screen compensation for the Sentinel-1 TOPS and ALOS-2 ScanSAR modes, *IEEE Transactions on Geoscience and Remote Sensing*, *55*(1), 223–235.

Grandin, R., E. Klein, M. Métois, and C. Vigny (2016), Three-dimensional displacement field of the 2015 Mw 8.3 Illapel earthquake (Chile) from across- and along-track Sentinel-1 TOPS interferometry, *Geophysical Research Letters*, *43*(6), 2552–2561.

Gray, A. L., K. E. Mattar, and G. Sofko (2000), Influence of ionospheric electron density fluctuations on satellite radar interferometry, *Geophysical Research Letters*, *27*(10), 1451–1454.

Jung, H.-S., D.-T. Lee, Z. Lu, and J.-S. Won (2013), Ionospheric correction of SAR interferograms by multiple-aperture interferometry, *IEEE Transactions on Geoscience and Remote Sensing*, *51*(5), 3191–3199.

Liu, Z., H.-S. Jung, and Z. Lu (2014), Joint correction of ionosphere noise and orbital error in L-band SAR interferometry of interseismic deformation in southern california, *IEEE Transactions on Geoscience and Remote Sensing*, *52*(6), 3421–3427.

Prats-Iraola, P., R. Scheiber, L. Marotti, S. Wollstadt, and A. Reigber (2012), TOPS interferometry with TerraSAR-X, *IEEE Transactions on geoscience and remote sensing*, *50*(8), 3179–3188.

Raucoules, D., and M. De Michele (2010), Assessing ionospheric influence on l-band sar data: Implications on coseismic displacement measurements of the 2008 Sichuan earthquake, *IEEE Geoscience and Remote Sensing Letters*, *7*(2), 286–290.

Scheiber, R., M. Jäger, P. Prats-Iraola, F. De Zan, and D. Geudtner (2015), Speckle tracking and interferometric processing of TerraSA-X TOPS data for mapping nonstationary scenarios, *IEEE Journal of Selected Topics in Applied Earth Observations and Remote Sensing*, *8*(4), 1709–1720.

Tymofyeyeva, E., and Y. Fialko (2015), Mitigation of atmospheric phase delays in insar data, with application to the eastern California shear zone, *Journal of Geophysical Research: Solid Earth*, *120*(8), 5952–5963.

Xu, B., Z. Li, G. Feng, Z. Zhang, Q. Wang, J. Hu, and X. Chen (2016), Continent-wide 2-d co-seismic deformation of the 2015 Mw 8.3 Illapel, Chile earthquake derived from Sentinel-1A data: Correction of azimuth co-registration error, *Remote Sensing*, *8*(5), 376.

Xu, X., D. T. Sandwell, E. Tymofyeyeva, A. González-Ortega, and X. Tong (2017), Tectonic and anthropogenic deformation at the Cerro Prieto geothermal step-over revealed by Sentinel-1A InSAR, *IEEE Transactions on Geoscience and Remote Sensing*.